Industrial Rotating Kiln Simulation

This thesis is presented for the degree of Doctor of Philosophy

Faculty of Science

University of Technology, Sydney

1999

Submitted by Dennis Van Puyvelde, B. Chem. Eng. (Hons)

Certificate of Authorship/Originality

I certify that the work in this thesis has not been previously submitted for a degree nor has it been submitted as part of requirements for a degree except as fully acknowledged within the text.

I also certify that the thesis has been written by me. Any help that I have received in my research work and the preparation of the thesis itself has been acknowledged. In addition, I certify that all information sources and literature used are indicated in the thesis.

Signature of Candidate

_____

ABSTRACT

A new industrial process is being developed to allow the commercial recovery of oil from oil shales. As part of this process, a rotating kiln is used to pyrolyse the organic component of the oil shales. The configuration and application of this rotating kiln is unique and hence previous rotating kiln models cannot be used to predict the solid behaviour in the current processor. It is the aim of this work to develop mathematical models which allow the prediction of mixing, segregation and heat transfer in industrial rotating kilns, especially with respect to the new rotating kiln technology trialed in the oil shale industry.

Experiments were developed to observe and measure the mixing and segregation behaviour of solids in rotating drums. These experiments used image analysis and provided quantitative results. Further experiments were carried out to allow suitable scaling parameters to be developed.

All the mixing experiments followed a constant mixing rate until the bed became fully mixed. The mixing rate and the final amount of mixing depended on the rotational velocity, the drum loading, the particle size and the material ratio. The segregation dynamics occurred too fast to be measured. However the final segregated state was measured and depended on the rotational velocity and the differences in particle sizes. Scaling parameters were developed that related the mixing and segregation results to the operational variables of the rotating kiln.

Mathematical models were derived for the mixing and segregation of solids in a rotating kiln and these models included the developed scaling parameters so that these models would be useful for the prediction of the solid behaviour in industrial rotating kilns. The mathematical models were applied to independent experiments and it was found that they predicted the mixing and segregation to within the

experimental error, even for different sized drums indicating that the developed scaling parameters were suitable.

A computational simulation of the industrial rotating kiln processor was developed by combining the mathematical models of the mixing and segregation with heat transfer modelling applicable to this industrial rotating kiln. A case study was completed to study the behaviour of the industrial rotating kiln by changing operational variables, such as the rotational speed and the particle size.

The developed simulation can be used to predict the dynamic behaviour of the rotating kiln used in the emerging oil from oil shale industry. This simulation can assist in further commercialisation of this new industrial process.

ACKNOWLEDGEMENTS

I would like to thank the following for their assistance during the course of my PhD research.

Firstly my academic and industrial supervisors: Dr. Brent Young from the University of Calgary, Canada, Professor Michael Wilson from the University of Technology, Sydney, Dr. Stephen Grocott and Mr. Jim Schmidt from Southern Pacific Petroleum (Development). Dr. Young deserves a special mention by going beyond his initial commitment as a local supervisor and maintaining excellent supervision after his relocation to Canada.

Financial commitment for the project was provided by Southern Pacific Petroleum N.L. and the University of Technology, Sydney. This financial assistance made the work possible and allowed me to present my work at various conferences.

All the present and past members of the Chemical Technology and Engineering Research Group – especially Dr. Adam Berkovich, for helpful discussions. Especially the ones held at The Duke of Cornwell.

The Faculty of Science workshop and Mr. Alan Barnes were very helpful in the design of the experimental equipment.

The Faculty of Science Research Degrees Committee and the University's Chemical Society for showing me there is more to a research degree than research.

My parents and family.

Lastly and most importantly, I would like to take the opportunity to thank my wife and best friend Shannon Elizabeth for her wonderful support throughout the last three years of my life.

Table of content

Table of Figures

CHAPTER 1

Introduction.

The focus of this chapter is to introduce rotary kilns. A new development in the oil shale industry, the Stuart project, will also be described and this will be followed by a description of the AOSTRA-Taciuk Processor and its significance in the Stuart project. The chapter will be concluded with the research objectives for the current research project.

1.1 APPLICATIONS AND DESCRIPTIONS OF ROTARY KILNS

Rotary kilns are widely used in industry. Some of their applications include the calcining of mineral ores (Barr et al, 1989a, b; Boateng, 1993), the drying of a granular product such as fruit and grain (Sotocinal et al, 1997a) and a new process to pyrolyse oil shale (Southern Pacific Petroleum, 1991).

In their simplest form, rotary kilns consist of long horizontal or slightly inclined smooth cylindrical shells with partially enclosed ends. Variations of this basic design may include the use of tapered ends or flights to control the solid throughput or the solid behaviour in the rotating kiln (Kramers & Croockewit, 1952). Granular materials are fed to the inclined drums at the higher end and proceed through the drum to exit at the lower end. Flow through a horizontal rotary kiln can be achieved by having the bed of solids sloping down towards the exit so that the solids roll down the inclined surface of the bed. In this latter case the bed height is not uniform along the kiln length. If a uniform bed height is required in a horizontal drum, specially designed pushers could be used to move the material through the horizontal drum. More complex rotary kilns may have flights along the cylindrical shell to lift the granular material above the bed of solids to enhance the interaction between the gaseous medium and the solid material (Baker, 1992; Sherritt et al 1993, 1994).

Rotary kilns are normally used to transfer heat to or from the granular material inside the rotating kiln. For drying or calcining this heat is usually supplied in the form of an emissive flame above the bed of solids. Alternatively, the heat may be supplied to the outside of the rotary kiln. In the latter case, the main mode of heat transfer would be via conduction through the cylinder wall and conduction into the bed of solids. A third way of heat transfer in rotating kilns is through the use of a granular heating medium. This granular medium heating technique is normally used if a uniform temperature is required across the bed of solids.

To ensure a uniform temperature of particles in the rotary kiln sufficient mixing between the solids closer to the heat source and furthest from the heat source must occur. Rotation of the kiln will result in the mixing of the solid charge, thus enhancing heat transfer between the particles and ensuring the movement of solids through the kiln. Rotary kilns require a smaller capital investment when compared with other drying equipment and their operating costs, their flexibility with respect to feed particle size and their fuel capacity make them very suitable for the processing industries (Sai et al, 1990; Sotocinal et al, 1997a). Usually a rotary kiln is loaded below 40% of its volume but loadings from 3% (Woodle & Munro, 1991) up to 70% (Hogg & Fuerstenau, 1972) of the kiln volume have been reported. Commercial rotary kilns range from 0.30 m to 7.00 m diameter and from 2 to 90 m in length and large volumetric throughputs are normally achieved in industrial rotary kilns.

1.2 "OIL FROM OIL SHALE" PROCESS

The extraction of oil from oil shale has been, and still is, important in various parts of the world including Estonia, Canada, China and Australia (Southern Pacific Petroleum, 1991).

1.2.1 Oil shale in Australia

In Australia, oil was recovered from oil shale as early as 1865. The first Australian commercial "oil from oil shale" recovery was achieved at Port Kembla, New South Wales. The demise of the Australian oil shale industry occurred in 1906 at Joadja

Creek, New South Wales due to the availability of more competitive oil products from the petroleum fields. During the World War 2 era, "oil from oil shale" processes once again became an important source of oil at the Glen Davis site in New South Wales. However, this operation was never profitable and was closed in 1952 (Australian Institute of Petroleum, 1993).

1.2.2 The Stuart project

Since the early 1970's Southern Pacific Petroleum in partnership with Central Pacific Minerals have invested $A150 million investigating possible oil shale sites in South Eastern Queensland and researching "oil from oil shale" extraction processes (Southern Pacific Petroleum, 1991). Together they hold titles to 10 oil shale deposits containing $28.6 * 10^9$ barrels of in-situ oil. The most favourable site is the Kerosene Creek member of the Stuart deposit near Gladstone (Bram, 1995). The location of Gladstone is shown in Figure 1.1 and is approximately 600 km North of Brisbane. The Kerosene Creek oil shale member is rich in oil compared to oil shales from other sites (Berkovich et al, 1997). Furthermore, Kerosene Creek is closely situated to an industrial port and has the necessary infrastructure making it an ideal site to test the viability of the new technology used in the re-emerging "oil from oil shale" industry.

The Stuart Project consists of three stages. The first stage is a demonstration plant, the construction of which was completed in April 1999. The planned production of this stage is 4500 barrels of oil per day and the commercial viability of the technology used in the Stuart project will be evaluated in stage 1. The second stage involves the construction of a commercial module and the construction of this stage is planned for the year 2000. A full-scale commercial plant with a capacity of 85000 barrels of oil per day is expected to be in operation by the year 2005. The reserve of the Stuart mining lease is estimated to be to $3 ½ * 10^9$ barrels of oil which could result in a 20 year operating life of the final stage retort plant at full production. Development of the demonstration plant is a joint venture between Southern Pacific Petroleum N.L., Central Pacific Minerals N.L. and Suncor Energy.

Figure 1.1: Map of Australia showing the location of Gladstone.

1.2.3 The AOSTRA-Taciuk Processor

The AOSTRA-Taciuk Processor was invented by William Taciuk and developed by the Alberta Oil Sands Technology and Research Authority (AOSTRA) and Umatac Industrial Processes (Taciuk & Turner, 1988). This is the preferred technology for the "oil from oil shale" process in the Stuart project.

The AOSTRA-Taciuk Processor is shown schematically in Figure 1.2. This process is unique as it employs two solid materials inside the rotary kiln to optimise the use of process heat. One of the materials, the preheated shale, is the initial reaction charge and the other material, the combusted shale, supplies additional heat. It is necessary to model the interaction of these two solid materials so that the heat transfer between the two materials can be calculated and the rate of volatile evolution can be predicted.

The AOSTRA-Taciuk Processor consists of three zones, namely the preheat/cooling zone, the retort zone and the combustion zone. These zones are shown in Figure 1.2. In the preheat/cooling zone the fresh shale is heated from ambient conditions to approximately 250°C. This preliminary heating removes the surface-and-inherent moisture from the fresh shale. This heating is achieved by recovering the heat from the hot combusted spent shale which is at approximately 800°C. The preheated shale is then passed into the retort zone where it is directly mixed with hot combusted spent shale. Heating of the oil shale in the retort zone allows the kerogen, the organic component of oil shale, to be pyrolysed and to be removed as gaseous products. These volatiles are processed in the separations and upgrading sections of the plant. During the kerogen decomposition in the retort zone a layer of organic material is formed on the surface of the solid material. This spent shale is then passed into the combustion zone where the surface organic matter is combusted to raise the temperature to approximately 800°C. This hot combusted spent shale is split into two streams and returned to the processor. One of the streams is returned to the retort zone to mix with preheated shale. The remaining stream is removed from the processor after heat recovery in the preheat/cooling zone.

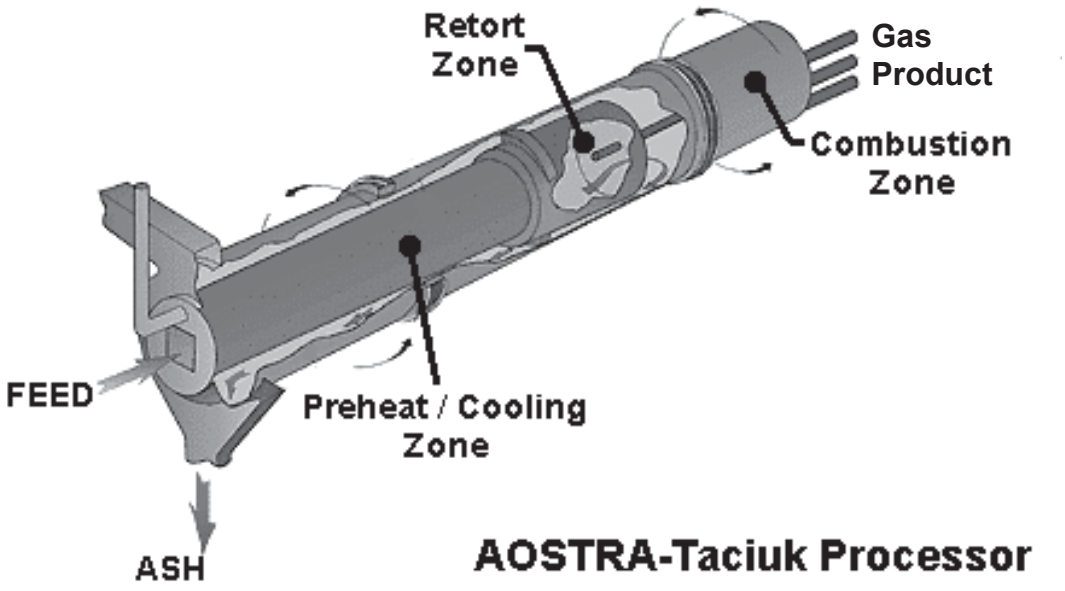

Figure 1.2: Schematic of the AOSTRA-Taciuk Processor (Southern Pacific Petroleum, 1991).

1.3 RESEARCH OBJECTIVES

The mechanisms of mixing, segregation, heat transfer and volatile evolution in the AOSTRA-Taciuk Processor are not well understood. These mechanisms affect the rate of kerogen decomposition and thus the efficient operation of the AOSTRA-Taciuk Processor. The current research project focuses on modelling the behaviour of solids in the retort zone. This mixing and segregation work is unique due to the nature of combining two separate materials, each of which has a wide particle size range. The heat transfer between the granular materials is also unique since most heat transfer applications of rotary kilns are from the gaseous phase to the solid phase, and due to the complex chemistry of the kerogen decomposition. In the case of the current research heat transfer occurs between the preheated oil shale and the hot combusted spent shale.

The current research objectives are:

1. Review the literature pertaining to the mixing, segregation and thermal behaviour of solid materials in rotating drums.
2. To develop experimental methods to study the solid behaviour in a rotating drum.
3. To study and model the effect of rotating drum parameters on solid mixing.
4. To study and model the effect of rotating drum parameters on solid segregation.
5. To simulate the mixing and segregation of solids in a rotating drum.
6. To develop a granular heat transfer model applicable to the AOSTRA-Taciuk Processor.
7. To simulate the AOSTRA-Taciuk Processor using the derived models. The prediction of volatile evolution from the retort zone is a requirement of this simulation.

The prediction of the behaviour of the solid particles and the implementation of the granular heat transfer will allow the rate of kerogen decomposition and volatile

evolution to be predicted in the AOSTRA-Taciuk Processor. This would be a very useful industrial tool that could be adapted for operator training and plant control.

1.4 THESIS STRUCTURE

Chapter 2 will characterise and describe granular media and their behaviour with respect to mixing, segregation and heat transfer. Previous research carried out in rotating drums, covering all aspects such as characterisation, mixing, segregation and heat transfer will be described in Chapter 3. The current experimental design is covered in Chapter 4. The active layer is an important parameter in the behaviour of solids in a rotating drum and is studied in Chapter 5 to develop scaling parameters for rotating drums. Chapter 6 describes the experimental and modelling work to study the solids mixing in a rotating drum. Chapter 7 describes the experimental and modelling work carried out to study the solids segregation in a rotating drum. A simulation of the mixing and segregation in a rotating drum will be described in Chapter 8. The heat transfer mechanism of the solids will be derived in Chapter 9, followed by the simulation of the AOSTRA-Taciuk Processor. Conclusions of the current research project are made in Chapter 10.

1.5 CHAPTER SUMMARY

In this chapter rotary kilns were briefly described. The Stuart project and the use of the AOSTRA-Taciuk Processor were described. The chapter concluded with the research objectives of this thesis.

CHAPTER 2

Mixing, segregation and heat transfer mechanisms of granular materials.

To familiarise the reader with the mixing, segregation and heat transfer mechanisms of granular materials this chapter will summarise those mechanisms that are applicable to any granular flow.

Granular flows are important in many chemical engineering applications ranging from combustion of solid fuels to cement calcining to environmental protection. The particles used in these processes range in size from microscopic to macroscopic and have different physical properties such as chemical composition, surface area and voidage, static and dynamic friction coefficients, particle and bulk densities and thermal conductivities.

The interaction between particles is important as this effects the movement of the granular materials. For example, Bridgewater (1976) noted that a cohesive material formed aggregates, which resulted in flow blockages or the clogging of orifices. On the other hand free flowing materials acted as individual particles. In general, Bridgewater (1976) found that material less than 100 micrometers were of a cohesive nature.

The flow of a granular material is strongly dependent on the physical properties of the material such as the angle of repose and the bulk density. This granular flow resulted in the mixing and/or segregation of the granular material. This also affected the heat transfer and/or reactions between different granular materials.

2.1 MIXING OF GRANULAR MATERIALS

Mixing of granular materials results in an increase of disorder between the solids, which results in more interaction between the different solids. The amount of mixing

can be related to the amount of surface contact between the particles of the two materials. A larger amount of contact would indicate that the granular material is mixed better.

Rose (1959) proposed a correlation to predict the complete mixing process, where the mixing rate, $\frac{dM}{dt}$ was given as:

$$\frac{dM}{dt} = a(1 - M) - b\varsigma \qquad (2.1)$$

where M was the degree of mixing which was zero for a non mixed bed and 1 for a fully mixed bed, ς was the segregation rate, a and b were constants for a particular mixture, mixer and operating conditions. This proposal is very limited in its application and indicated that many more laboratory studies needed to be conducted before a generic model of granular behaviour could be evolved.

Donald & Roseman (1962) defined "useless" and "useful" mixing. "Useful" mixing occurs when a particle of one type was replaced by a particle of another type whereas "useless" mixing indicates that a particle was replaced by a particle of the same type. "Useless" mixing occurs at all times whilst the bed is in motion whereas "useful" mixing occurs only until the bed is fully mixed. Nevertheless "useless" mixing still occurs resulting in the rearrangement of particles of the already mixed bed. This did not affect the mixing extent of the granular material but may have important implications in secondary processes related to mixing such as heat transfer or reactions between particles.

Donald & Roseman (1962) described the mixing of a granular material as the result of the combination of three mixing processes. These processes are shear, convective and diffusive mixing. Hogg et al (1966) indicated that for mixing to occur, the separate components must be brought together and then the individual particles must diffuse across the boundaries. This involves a combination of the three mixing mechanisms mentioned above. Each of these mechanisms is described briefly in the following paragraphs.

2.1.1 Shear mixing of granular materials

Shear mixing, as the name suggests, occurs due to the shear stresses being applied to the solid bulk of a granular material. These stresses concentrate at slipping planes and when these stresses exceed the inter particle frictional forces, the granular materials move relative to each other (Bridgewater, 1976). This results in a bulk relocation of some of the granular material and provides bulk mixing as shown by an increase of the contact between the two different coloured regions at the slipping plane, each representative of a different material, in Figure 2.1. The thick inclined line in Figure 2.1 shows the location of the slipping plane.

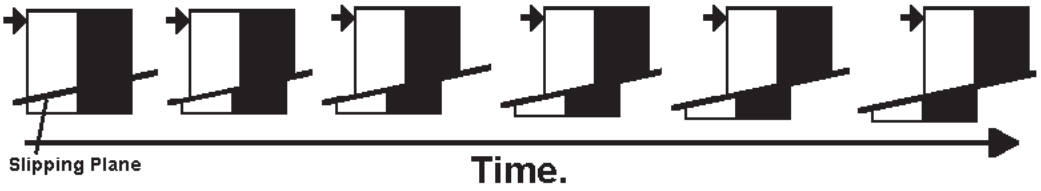

Figure 2.1:Shear mixing of a granular material.

2.1.2 Convective mixing of granular materials

Convective mixing is also a bulk mixing mechanism and occurs as a result of the velocity gradients within granular materials (Cahn & Fuerstenau, 1967; Hogg & Fuerstenau, 1972).

The shear rates between different layers of particles result in the layers sliding over each other as shown in Figure 2.2. By definition, convective mixing is fully reversible since there is no random distribution of the materials during the convective mixing process. Hogg & Fuerstenau (1972) described the convective mixing in a rotating drum at low speeds.

Figure 2.2:Convective mixing of a granular material.

2.1.3 Diffusive mixing of granular materials

Diffusion was described by Hogg et al (1966) and Cahn & Fuerstenau (1967) to conform to the one dimensional form of Fick's second law of diffusion which states that the diffusion mixing process is completely random, similar to the diffusion process in liquids or gases and is given by:

$$\frac{\partial C(x,t)}{\partial t} = \frac{\partial}{\partial x}\left(Đ_{Diff} \frac{\partial C(x,t)}{\partial x} \right) \tag{2.2}$$

where $C(x,t)$ is the concentration at any time, t, and distance, x, from the original surface and $Đ_{Diff}$ is the diffusion coefficient. The solution to Fick's second law was presented by Hogg et al (1966) and can be used to predict the relative concentrations of a mixture at any point and any time.

Cahn & Fuerstenau (1967) defined diffusion mixing as "micromixing" where the individual particles diffused across boundaries between regions rich in one component into regions rich in another component. Zik & Stavans (1991) found that an oscillating velocity in a bed of particles resulted in self diffusion of the materials in the bed. Kohring (1995) showed that the self diffusion coefficient of the materials increased as the magnitude of the oscillating velocity increased. Figure 2.3 illustrates the diffusive mixing mechanism of an initially separated material subjected to an oscillating horizontal velocity.

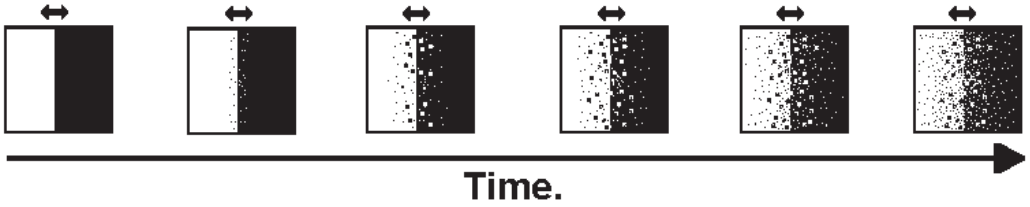

Figure 2.3: Diffusive mixing of a granular material subject of an oscillating horizontal velocity.

2.2 SEGREGATION OF GRANULAR MATERIALS

When using a mixture of various particle sizes Rutgers (1965b) found that accumulation of the finer particles in the voids created by the larger particles was quite common and termed this phenomenon segregation. Segregation is caused by the differences in physical properties of particles such as density, size, shape, roughness and resilience (Bridgewater, 1976). Williams & Khan (1973) found that in most applications segregation is caused by particle size differences. However Alonso et al (1991) reported that if the density ratio was large enough, segregation due to these density differences could also occur.

Roseman & Donald (1962) predicted the occurrence of segregation from the ratio of the two particle diameters. If this ratio was smaller than 1.2 no segregation occurred since the smaller particles could not slip through the voids created by the moving larger solids. Segregation occurred if this ratio was greater than 1.2. Donald & Roseman (1962) observed that mixing and segregation times were dependent on the particle size and particle density but not on the particle type. Williams & Khan (1973) showed that different packing arrangements gave different ratios of the particle size to gap size. For three particles touching this ratio is 6.3, for four particles touching in a square arrangement the ratio is 2.4. These configurations are shown in Figure 2.4. In Williams & Khan's (1973) experimental work, the observed value of diameter ratio was 4.3, which indicated that the average packing of their packed bed was between the two theoretically calculated packing arrangements. The coefficient of segregation, indicating how fast and how much the materials segregate, increased rapidly as the diameter ratio increased from 1 to 2. At higher diameter ratios no further increase in the coefficient of segregation was observed.

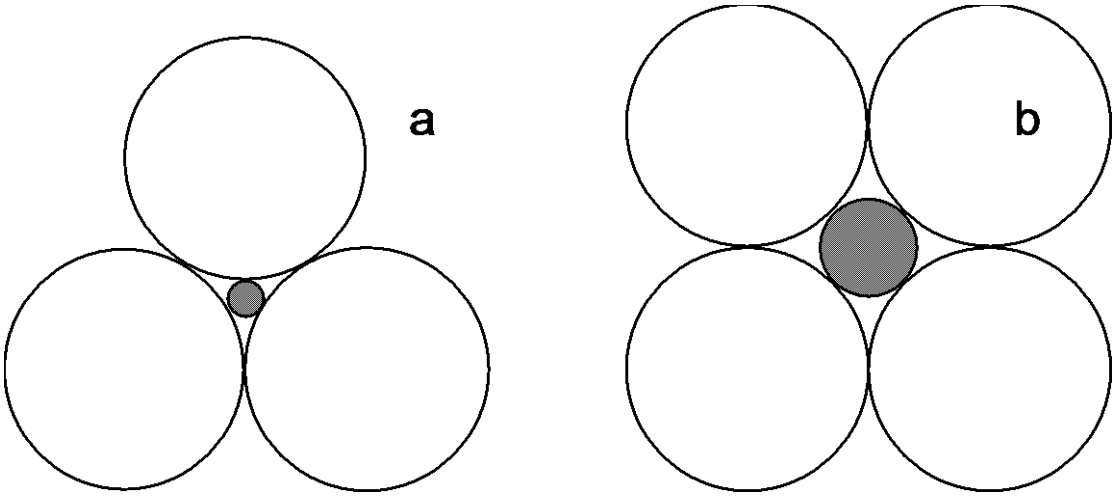

Figure 2.4:Different packing arrangements showing the difference in particle size to gap size: a) diameter ratio = 6.3, b) diameter ratio = 2.4 (Williams & Khan, 1973).

Segregation within a granular flow occurred via a combination of the percolation, flow and vibration mechanisms (Nityanand et al, 1986). These mechanisms are described below.

The darker particles in Figures 2.5 to 2.7 represent segregating particles as they segregated. The larger white particles represent the larger particles in the bed of solids.

2.2.1 Percolation segregation mechanism of granular materials

Percolation segregation occurs when smaller particles pass through the voids between the larger particles to accumulate beneath the larger particles. Williams & Khan (1973) stated that percolation segregation depended on "the probability that a particle will find a void into which to fall". This probability depends on the size of the particles and the particle size ratio. The most common occurrence of percolation segregation occurs in the pouring of heaps of multi sized particles and this is referred to as free surface segregation. The process of free surface segregation involves the percolation of the finer particles in the voids of the bed and the sinking of the heavier particles due to their larger relative weight as shown in Figure 2.5 (Alonso et al, 1991). The dark filled circles of Figure 2.5 to 2.7 represents the segregating

particle. The smaller heavier particles end up at the bottom of the bed and the larger lighter particles end up at the top of the bed. Alonso et al (1991) derived a correlation, which can be used to calculate an appropriate density ratio to compensate for the percolation segregation mechanism so that the mixture will not segregate.

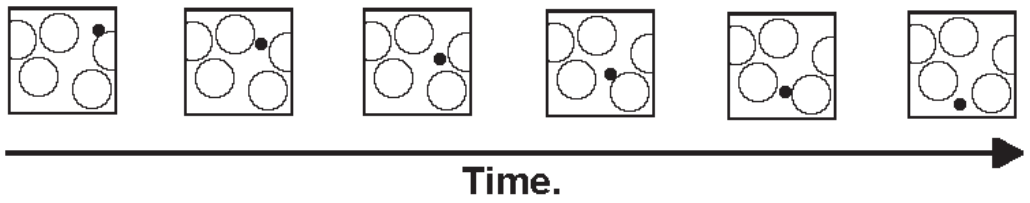

Figure 2.5:Percolation segregation of a granular material.

Spontaneous segregation occurs when the finer material segregates through a stationary bulk of larger particles (Bridgewater, 1976). The gravitational force acting on the fine particles is sufficient to allow the fine particles to fall through the voids created between the larger particles.

2.2.2 Flow or trajectory segregation mechanism of a granular material

When particles are projected across a surface the distance they travel along this surface is proportional to the square of the particle diameter (Williams & Khan, 1973). This indicates that a larger particle travels further compared to a smaller particle as shown in Figure 2.6. This occurs because the smaller particles are captured more readily by the inclined plane due to the increased relative contact area of the smaller particles and this increases the dynamic friction for these particles thereby reducing their velocity.

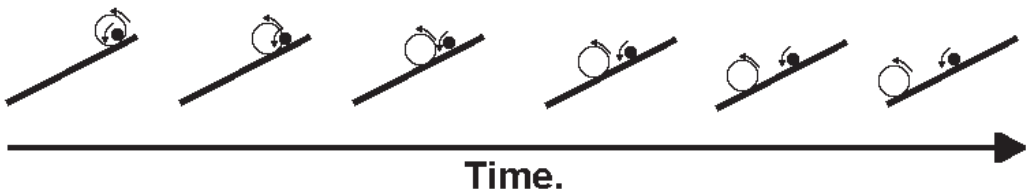

Figure 2.6:Flow segregation of a granular material.

2.2.3 Vibration segregation mechanism of a granular material

The final possible segregation mechanism is vibration segregation. Vibration segregation occurs when a bed of particles is vibrated. The larger particles rise to the surface even if they are denser than the finer particles (Williams & Khan, 1973). This is illustrated in Figure 2.7.

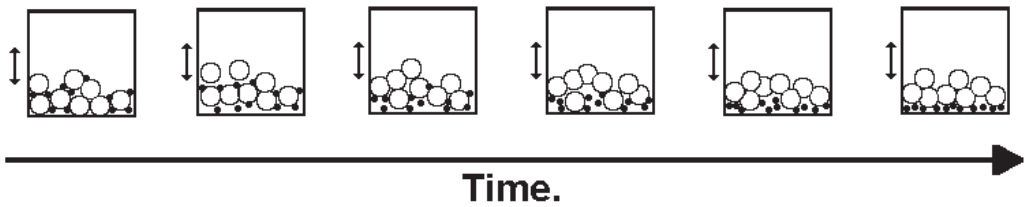

Figure 2.7:Vibration segregation of a granular material.

2.3 HEAT TRANSFER IN GRANULAR MATERIALS

Heat transfer in a granular medium occurs through a combination of conduction, convection, radiation and advection (Arpaci, 1966). The relevance of each of these heat transfer mechanisms depends on the nature of the granular material. Radiation heat transfer is important for particles greater than 1 mm diameter or at a temperature of more than 400°C (Saatdjian & Large, 1988). Under these conditions, Yagi & Kunii (1957) and Schotte (1960) reported that radiation could account for up to 80% of the total heat transfer. Molerus (1997) showed that there is negligible contact between large hard particles indicating that conduction heat transfer between such particles is negligible.

2.3.1 Heat transfer paths between particles

Heat transfer between solid particles has been described by Yagi & Kunii (1957) and Kunii & Smith (1960). Figure 2.8 illustrates the different paths of heat transfer between particles. Heat transfer path 1 is the conduction heat transfer between the particles through the points of contact between the particles. Path 2 is the heat transfer by conduction and convection through the fluid film near the place of

contact. Heat transfer path 3 is the net radiation heat transfer from the surface of a hot particle to the surface of cold particle. Radiation from the hot particle to the void space between particles and radiation from the void space to the cold particle are described as paths 4 and 5, respectively. Lastly path 6 describes the heat transfer from the surface of the cold particle into the bulk of the colder particle due to conduction. The total heat transfer through all six paths, Q, to the cold particle can be described as:

$$Q = UA\Delta T \tag{2.3}$$

where U is the overall heat transfer coefficient, A is the heat transfer area of the particle and ΔT is the temperature difference between the particles.

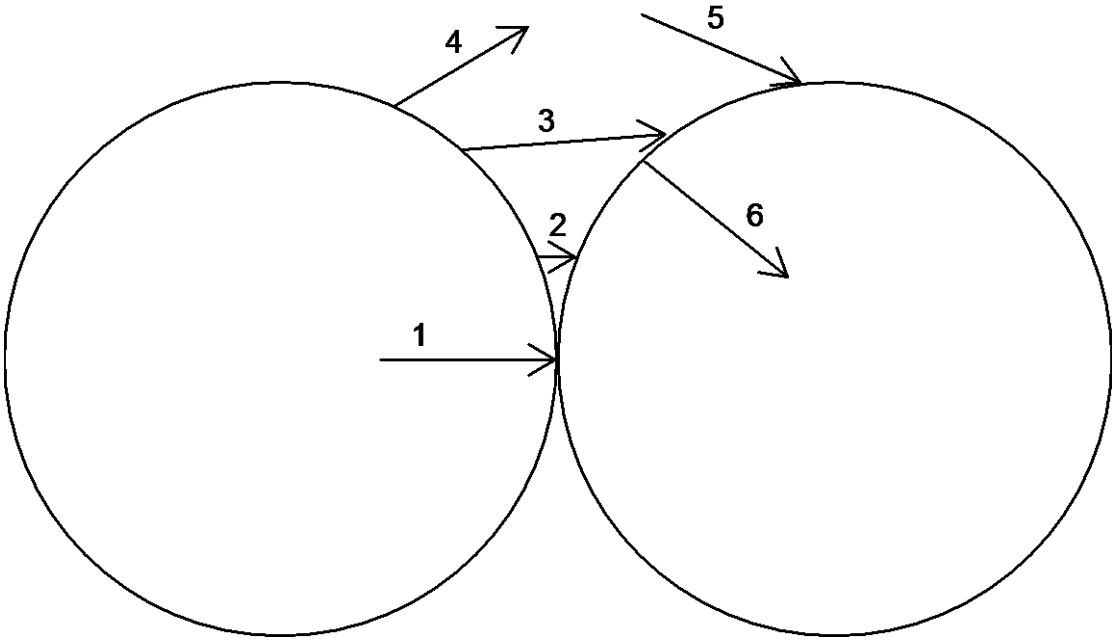

Figure 2.8; Heat transfer paths between particles (Yagi & Kunii, 1957).

Rao & Toor (1984, 1987) studied the effects of size and thermal conductivity ratios on the heat transfer from a particle to a surrounding bed of particles. They found that the discrete nature of the particle diminished as the conductivity ratio was decreased or the particle size ratio was increased. Under these conditions, the heat transfer from the particle could be considered as heat transfer from the particle to a continuum. However, the discrete nature of the particles must be considered if the

test particle was of similar size to the bed particles. Their discrete model to determine the heat transfer coefficient from their test particle to the bed of particles included a measurement for the number of contacts between the test particle and the particles in the surrounding bed.

Saadjian & Large (1988) indicated that the heat transfer between larger particles at elevated temperatures occurred predominantly through radiation. When a gaseous medium was used, convection between the stagnant fluid and the particles was small due to the lower thermal conductivity of the gases compared to that of solids.

2.3.2 Heat transfer in a granular medium

A granular medium can be described as numerous particle-particle interactions and the heat transfer in a granular medium occurred through these interactions. The effective thermal conductivity of the granular medium has been used to determine the heat transfer to the granular medium (Schotte, 1960; Dixon & Cresswell, 1979). Yagi & Kunii (1957) calculated the effective thermal conductivity, k_e^0, of a stationary medium. In a moving medium the effective thermal conductivity of the granular medium, k_e, includes a transport term so that:

$$k_e = k_e^{\,0} + k_e^{\,t} \qquad (2.4)$$

where k_e^t was the effective thermal conductivity dependent of the fluid flow. Yagi & Kunii (1957) included the mean particle diameter and the radiative heat transfer in their thermal conductivity determination. Kunii & Smith (1960) found that there was a decrease in thermal conductivity with an increase in void fraction. Barker (1965) found that bed packing directly affected the bed voidage and the contact between the particles. Since fine dusts can have a voidage of up to 98% the presence of fine dusts in poorly packed beds could results in a decrease of the thermal conductivity of the granular medium.

Gurgel & Kluppel (1996) studied the heat transfer in a granular medium by changing the moisture content of the voidage between particles. They found that the bed

thermal conductivity was strongly dependent on the voidage composition. This indicated that the heat transfer in a granular medium was limited by the thermal conductivity of the fluid in the voids of the granular medium. This is especially important at lower temperatures where the radiation heat transfer is not dominant. Furthermore, Hunt (1997) also found that the fluid phase properties of a granular medium are critical in the heat transfer since the particles exchanged most of their heat with the fluid. This is especially important if the fluid is a gas since thermal conductivities of gases are much lower compared with thermal conductivities of solids thereby limiting the heat transfer rate.

Granular materials have been used to dry fruits and grains due to the enhanced conduction between solids because of the larger thermal mass of solid materials compared to air. This heat transfer mechanism was referred to as granular medium heat transfer. Raghavan et al (1974) found that using granular materials had the advantage of being economical and provided a uniform heat transfer from one material to the other depending on the mixing conditions of the granular medium. Sullivan et al (1975) found that the increase in thermal mass, compared with gaseous heating, resulted in shorter drying times and reduced overheating of the material to be dried.

Particulate medium heating is the method of heat exchange between the solids in the AOSTRA-Taciuk Processor. However in the AOSTRA-Taciuk Processor, the operating temperatures are significantly higher than those experienced in previous particulate medium heating systems and thus the heat transfer mechanism between the materials will be different.

2.4 CHAPTER SUMMARY

The movement of granular materials, namely the mixing and segregation mechanisms were introduced as well as the heat transfer characteristics of granular materials. Practical applications of mixing and/or segregation in rotating kilns are described in Chapter 3. Discussion of the heat transfer between particles will be expanded in Chapter 9 where the simulation of the AOSTRA-

Taciuk Processor, including heat transfer between the different particles and the volatile evolution will be carried out.

CHAPTER 3

Rotating drums and kilns – literature review.

In this chapter, the literature characterising the operations of a rotating drum is reviewed. This is then extended to include studies of the mixing, segregation and heat transfer of solids in rotary kilns.

The movement of solids in a rotary kiln consists of both a transverse and an axial component. The axial movement is defined as the movement parallel to the axis of the rotating drum whereas the transverse component occurs perpendicular to the axis. Barr et al (1989a, b) found that the transverse movement was important to obtain a homogenous bed. On the other hand, Perron & Bui (1990) noted that the axial movement was important for predicting the overall residence times of the solids in the kiln. Pershin & Minaev (1989a) believed that the intensity of heat and mass transfer depended to a great extent on the type of motion experienced in the transverse section of a rotating drum.

The literature shows that modelling of rotary kilns has been limited to either modelling in the transverse direction or the axial direction. Modelling to date includes flow, mixing, segregation and heat transfer in either the transverse or axial direction. The mixing and segregation models in the past have been mostly qualitative and focused on calcining kilns where the heat transfer occurs from the gaseous phase above the bed to the bed of solids. There is a lack of quantitative knowledge of the industrial rotary kiln especially with respect to the proposed AOSTRA-Taciuk Processor, which was described in Chapter 1.

Eventhough the focus of this thesis is the transverse motion of a rotating drum, it is relevant to discuss the axial motion since most industrial rotating kilns have high length to diameter ratios. The time spent travelling through the kiln is important from both an operational and economic point of view and is dependent upon the axial flow in the kiln.

3.1.1 Transverse bed regimes

Henein et al (1983a, b) described six different motion regimes in the transverse direction of a rotating bed as shown in Figure 3.1. The motion of the bed was shown to depend on the rotational velocity of the rotating drum and is commonly expressed as a function of the Froude number. The Froude number, *Fr*, is the ratio of centrifugal to gravitational forces and can be calculated using equation 3.1;

$$Fr = \frac{\varpi^2 R}{g} \tag{3.1}$$

where ω is the rotational velocity in rad s^{-1}, *R* is the radius of the drum in m and *g* is the acceleration due to gravity in ms^{-2}.

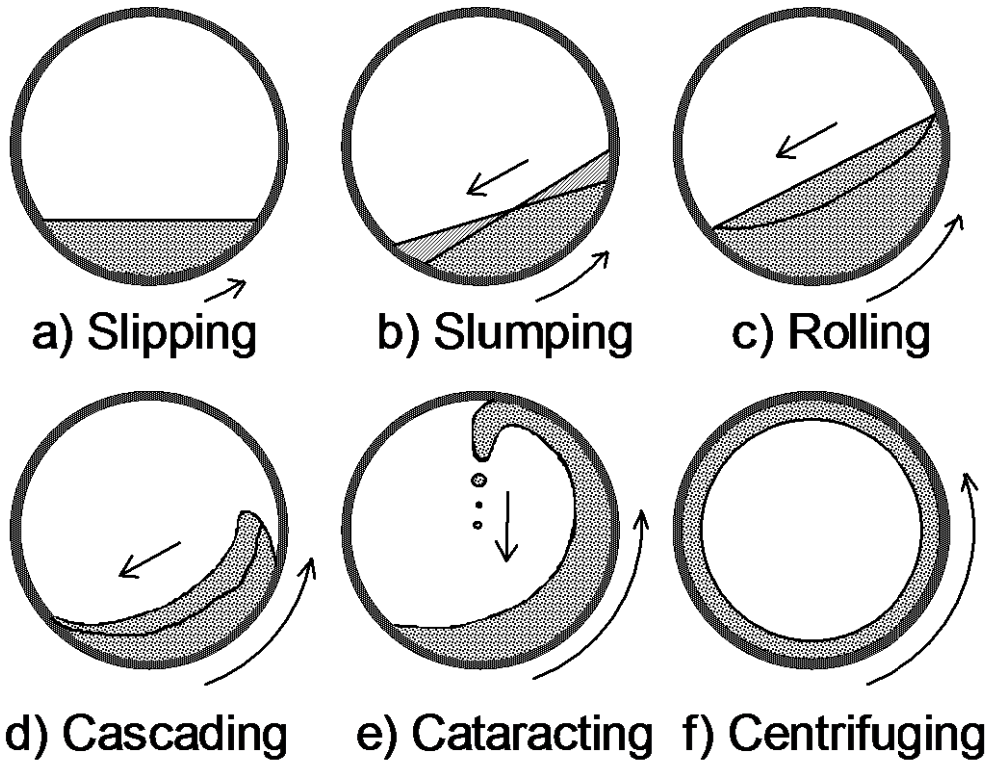

Figure 3.1 Different motion regimes in a rolling drum (Henein et al, 1983a, b).

At low speeds and low loading, Henein et al (1983a, b) showed that the bed "slipped" continuously. This was due to the low friction between the solids and the

drum walls, and resulted in minimal movement of the solids with respect to each other. At slightly higher speeds the bed passed through a "slumping" stage. When the potential energy of the material in the upper triangle, as shown in Figure 3.1b, exceeds the static inter-particle forces this material flows into the area indicated by the lower triangle. This slumping occurred periodically. Increasing the velocity further resulted in a "rolling" bed where the solid material continuously moved upward with the drum walls and rolled down the inclined surface, as shown in Figure 3.1c. "Cascading" is a more severe form of rolling and this occurs at slightly higher velocities where the upper surface of the bed became more wavelike. "Cataracting" occurs when solids at the high point of the bed became airborne due to the extra kinetic energy of the particles as they left the free surface of the bed. This was beneficial for extra gas-solid contact and was simulated at lower velocities using flights on the inside surface of the rolling drum. Papadakis et al (1994), Baker (1992) and Sherritt et al (1993, 1994) termed their cataracting regime as cascading even though this did not follow the cascading regime as described here. "Centrifuging", shown in Figure 3.1f, occurs when the kiln is rotating at a velocity greater than the critical speed. In this regime all the solids adhered to the wall and formed an annulus.

The critical rotational speed of a rotational drum, ω_c, can be calculated using:

$$\omega_c = \sqrt{\frac{g}{R}} \tag{3.2}$$

The Froude number equals 1 at the critical rotational speed (Henein et al, 1983a) since the centrifugal forces balance the gravitational ones. Rolling of the bed occurred when the rotational speed was greater than 0.10 ω_c and less than 0.55 ω_c. Rutgers (1965a) found that cataracting occurred in the region of 0.55 to 0.60 ω_c. Rolling, cascading and cataracting are the most common motion regimes since they provide good relative material movement. The focus of this research is on the transverse rolling regime, which will be described in the next section.

Henein et al (1983a, b) constructed "Bed Behaviour Diagrams" for different solids under different conditions in order to describe the motion regime of the solids bed. The "Bed Behaviour Diagrams" for the different materials are qualitatively similar. They found that nodular material rolled at lower rotational velocities compared to

irregular particles and that smaller particles rolled at higher rotational rates due to the extra interfacial area resulting in higher friction coefficients. These "Bed Behaviour Diagrams" could be used to predict the regime of the bed from the operational variables such as the rotational speed, the drum loading and the particle characterisation.

Pershin & Minaev (1989a) studied these transverse bed regimes and found that the mixing regime of the bed was dependent on the potential energy of the material in the bed.

3.1.2 The transverse rolling regime in a rotating drum

The rolling regime was described and observed by Lehmberg et al (1977) to consist of two layers, namely the active and stagnant layers. The stagnant layer was considered as a dense plug, which moved at the same rotational velocity as the wall due to the no slip boundary condition between the bed of solids and the wall. The active layer occurred when particles moved relative - down the incline - to each other resulting in both mixing and segregation. This regime has been studied in detail due to its importance in rotating kiln operation.

3.1.2.1 Description of the active layer in the rolling regime

Different active layer geometries, as shown in Figure 3.2, have been used in the past. Lehmberg et al (1977) observed that the active layer in a rolling bed was curved and occupied a certain percentage of the bed height. Mu & Perlmutter (1980) and Woodle & Munro (1993) considered the active layer as a layer of uniform thickness at the free surface of the rolling bed where the mixing occurred. Ferron & Singh (1991) considered the active layer as a very fast moving layer being a single particle thick at the top of the stagnant layer.

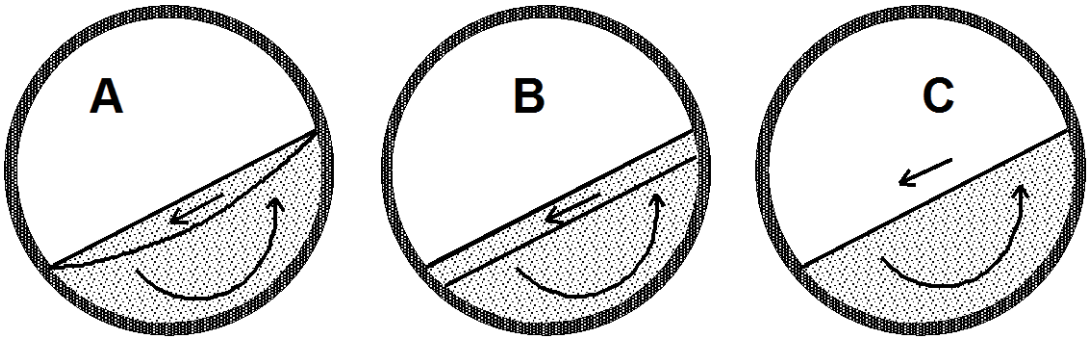

Figure 3.2: Active layer configurations; A) Lehmberg et al (1977), B) Mu & Perlmutter (1980), Woodle & Munro (1993), C) Ferron & Singh (1991).

Nakagawa et al (1992) measured the transverse velocity profile using magnetic resonance imaging. They observed that the velocity profile in both the active layer and stagnant layers were linear. The transverse velocity profile was confirmed by Boateng & Barr (1997) who measured the velocities of particles moving away from an optical probe. These experiments showed that the active layer thickness of a rolling bed could be approximated by a fraction of the bed height similar to the geometry used by Lehmberg et al (1977). This fraction depends on the granular material properties and the experimental conditions. Furthermore, Boateng (1993) observed that the velocity profile in the active layer of larger beds was skewed indicating that the material was still accelerating past the mid chord position and would not result in a symmetric velocity profile about the mid chord position. This has important implications in determining the solid behaviour in larger drums since more movement occurs between the particles in the lower section of the active layer compared to the movement in the upper section of the active layer. Figure 3.3 illustrates the velocity profile at mid chord in a rolling bed as observed by Nakagawa et al (1992) and Boateng & Barr (1997). The linear velocity gradients of both the active and stagnant layer are indicated on the figure. A mean velocity of each layer is also shown in the figure. As can be seen from the figure, the mean velocity in the active layer is significantly larger than the mean velocity in the stagnant layer and this, combined with the less dense packing of the active layer, results in the mixing and/or segregation of solids in the bed.

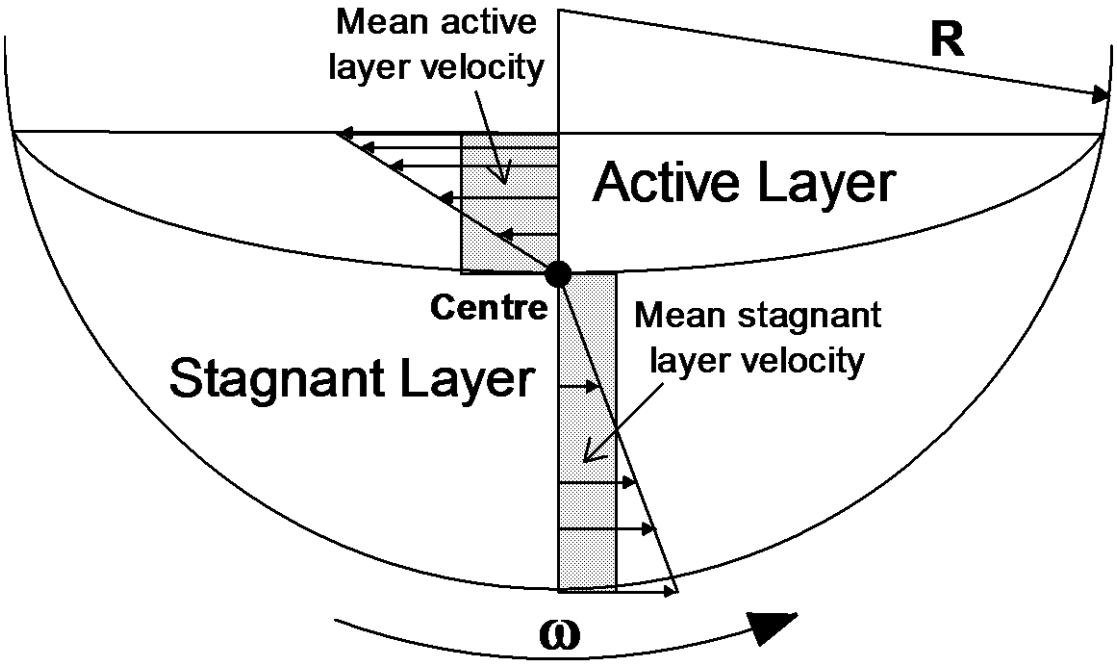

Figure 3.3: Rolling bed velocity profile (Nakagawa et al, 1992; Boateng, 1993).

The active layer depth was often considered as the proportion of the mid chord bed height occupied by the active layer. Cahn et al (1967) observed a "dead" zone in the transverse section when the bed was filled so that it exceeded 50% of the cylinder volume. Hogg & Fuerstenau (1972) removed this "dead" zone by increasing the velocity of the kiln so that the active layer proportion increased and the centre of rotation of the bed was forced below the centre of the "dead" zone. This early work showed that the active layer depth was dependent upon the rotational velocity. In their experimental study of transverse bed motion, Henein et al (1983a, b) noted that the active layer depth decreased for smaller particles, decreased with bed depth and increased with rotational speed. In further work Henein et al (1985) indicated that the fine proportion of the bed did not affect the size of the active layer. Boateng (1993) found that the active layer proportion with respect to bed depth increased with increasing rotational speed and decreased with bed loading. Yang & Farouk (1997) modelled the flow field of a rolling bed in a rotary kiln. At mid chord, their active layer depths were approximately 40-50 % of the bed height for all their experiments. They also measured the velocity profile for different sized particles and found that the active layer thickness increased for smaller particles, but the velocity gradient was not as steep. This was contradictory to the work of Henein et al (1983a,

b) and was probably due to the use of different granular materials and different experimental conditions. This emphasised that granular materials were not easily classified and that the behaviour of solid materials should be characterised prior using them in experimental studies.

Rutgers (1965b) measured voidages of the active layer between 0.50 and 0.55. Mu & Perlmutter (1980) showed that the initial velocities of particles entering the active layer are dependent upon the position at which the particles entered the active layer. The large voidages and the different velocities of particles resulted in the mixing and/or segregation of the solids as they passed through the active layer according to the mechanisms described in Chapter 2.

Donald & Roseman (1962) and Nityanand et al (1986) showed that measurements at the end surface of a rotating drum were not representative of the bulk of the drum. They found that the end effects were limited to a few particle diameters from the end of the drum. Boateng & Barr (1997) found that the end surface effect increased the angle subtended by the material by approximately 10% over that of the undisturbed region. This resulted in velocity enhancement of the particles in the active layer near the end surface. Due to this increased velocity of 20-25%, the active layer depth was observed to be smaller, by approximately 15%, at the end surfaces compared to the bulk. This end effect needs to be accounted for to fully model the behaviour of solids in a rotating bed. Thus, experimental results obtained through a transparent end surface included the end effects and needed to be corrected in order to predict the motion and mixing parameters within the bulk of the bed.

3.1.2.2 Description of the stagnant layer in the rolling regime

The stagnant layer has not been characterised to the same extent as the active layer. Rutgers (1965) measured the density of a bed of cereal grains to be approximately 70% of the loosely packed bulk density of the material. This bulk density decreased as the rotational velocity increased. The bulk phase of the rolling bed provided intimate particle-particle contact which was of great importance when heat or mass transfer was required within the bulk phase (Ferron & Singh, 1991). This showed the

importance of the bulk phase, which in most cases was considered as a moving packed bed.

3.1.2.3 Description of the mixing and segregation in the rolling regime

Mixing and segregation are two facets of the same physical process, namely granular flow. Since these processes are strongly linked and occur simultaneously, they will both be described together in this part of the thesis. This review is given in a chronological order and is concluded with a final paragraph to summarise the important findings.

Roseman & Donald (1962) showed that transverse mixing decreased as the bed height increased and that transverse mixing was slow. However, Rutgers (1965a, b) clearly stated that the mixing in the transverse direction was 2 to 4 orders of magnitude faster than mixing in the axial direction. Rutgers (1965a, b) found that most of the mixing in a rolling bed takes place in the bottom part of the active layer and that the extent of this mixing was determined more by the total number of revolutions rather than the velocity of the drum.

Hogg & Fuerstenau (1972) described the convective mixing mechanism, as described in Chapter 2, for a rotating drum. The convective mixing component can only be studied at low rotational velocities. Convective mixing occurs in a rolling bed due to the differences in particle circulation times. These differences occur when the particles re-enter the stagnant layer in the same circulation zone as the one they emerged from. In the stagnant layer, the residence times of the particles in all the circulation zones were equal. However the time spent in the active layer depended on the distance the particles traveled across this active layer. For the particles rotating closer to the wall, they need to travel a greater distance and as they travel further down the inclined plane their circulation period would be prolonged. In the meantime other particles closer to the centre had already re-entered the stagnant layer. This resulted in the formation of thinner and thinner bands as more rotations were experienced and eventually led to a system of numerous parallel thin bands. This is shown in Figure 3.4. Convective mixing as described here only occurred in

ideal situations. In reality, the mixing in the active layer also included diffusive components. Hogg & Fuerstenau (1972) treated the complete mixing in the transverse direction as a combination of convection and diffusion with convection described in terms of a distribution of circulation times and diffusion represented by random interchanges between the radial elements. However Cahn et al (1967) found a linear relationship between observed and simulated diffusion coefficients indicating that the mixing mechanism in a simple barrel mixer could be simulated by the diffusion equation. This does not indicate that mixing only occurred by diffusion but rather that the complete mixing, including convection and diffusion, could be expressed in terms of the diffusion equation. Bridgewater (1976) showed that the radial dispersion in a rotary kiln conformed to a solution of the diffusion equation, which agrees with the previous work by Cahn et al (1967).

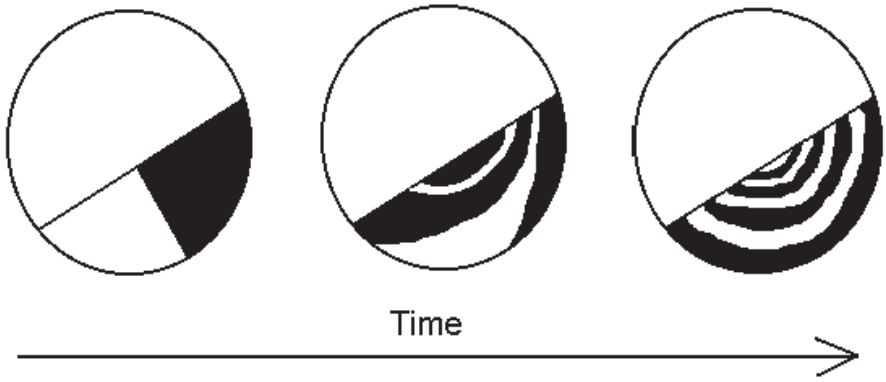

Figure 3.4: Convective mixing in a rotary kiln (Hogg & Fuerstenau, 1972).

In their study of inclined drums, Williams & Khan (1973) showed that the equilibrium of the solid mixture can be shifted towards segregation or mixing by altering the operating conditions of the cylinder, mainly the rotational speed. They showed that the segregation of materials in rolling drums was primarily due to the percolation mechanism, especially at low speeds.

Lehmberg et al (1977) measured the mixing of solids in the transverse direction of a rotating drum. A qualitative description of the mixing was given by mixing similar solids of different colours. The data obtained showed that a well mixed state was achieved after 42 seconds for 0.80 mm sand being mixed at rotational speed 2 rpm in

a 300 mm diameter drum. This was quantified using hot tracer particles and then the temperature was measured at the top of the bed. The temperature of the bed at this position followed an exponential oscillating decay with respect to the maximum temperature. The rate of mixing was not calculated by the authors but could be determined from the successive peaks by considering the heat transfer from the hot particles to the colder particles. This work did not determine the effects of changing experimental variables.

Henein et al (1985) observed that vibration segregation was not applicable to rotary kilns, instead segregation in rotary kilns is governed by the percolation mechanism, which is in agreement with the observations of Williams & Khan (1973).

Nityanand et al (1986) measured transverse segregation to occur within 1 to 10 bed revolutions whereas axial segregation took from 500 to 10000 bed revolutions for complete segregation. This order of magnitude difference between transverse and axial solid movement mechanism is quite often observed, not only for segregation but also for mixing. Furthermore, in the vicinity of the walls, such as in any visual experiment, the end wall effects decreased the size of the segregated core. As previously mentioned Boateng (1993) found that the velocity in the active layer increased near the walls. Combining these two results indicates that segregation decreases with increased velocity. Nityanand et al (1986) also showed that particles in the segregated core are restricted to the segregated core as shown in Figure 3.5.

Pollard & Henein (1989) showed that transverse segregation followed zero order kinetics and expressed the segregation behaviour as a normalised segregation rate. The initial content of fines in the bed did not effect the normalised segregation rate however a linear dependence on rotational speed was observed. The size ratio did effect the segregation rate, whereas bed depth did not effect the segregation rate. Pollard & Henein (1989) compared segregation rates of irregular limestone particles to smooth acrylic spheres and found these segregation rates to be similar. This indicates that the segregation rate is independent on the particle size and particle friction. This point was not adequately explained in the literature and illustrates the need for further research to study the behaviour of solids in rotating drums. Pollard

& Henein (1989) showed that the segregated core was of similar shape as the rotating bed and that the segregated core formed near the middle bottom of the active layer as shown in Figure 3.5.

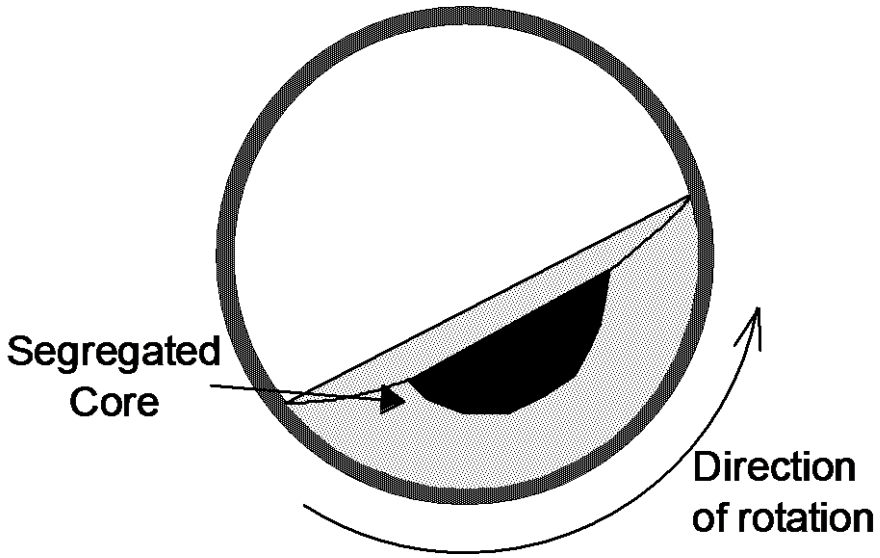

Figure 3.5: Schematic of the segregated core.

Pershin & Minaev (1989a, b) studied the mixing and segregation of a granular material in the transverse section of a rotary drum using the concentric sublayer model that was developed by Pershin (1987). Mixing or segregation was assumed to occur if the material moved from one sublayer to an adjoining one, only one transgression was permitted per bed revolution. This was not consistent with observations that segregation sometimes occurred within a single bed revolution, which required the movement of fines through numerous layers per bed revolution. Mixing occurred when a particle left its zone of circulation. Segregation occurred in a similar manner but with the added constraints of movement closer to the center of rotation and that the particle remained trapped in this new circulation zone. Mixing also occurred through the re-arrangement of particles within any sublayer but this was not considered by Pershin & Minaev (1989a, b).

Woodle & Munro (1993) measured mixing dynamics for ovoid, shell and tube solids from 3 to 15% loading in a rotating drum using a statistical method where the concentrations of the top and bottom surfaces of the bed were measured. These

experiments indicated that mixing occurred 10 times faster when strips were attached to the inside walls of the drum compared to a rolling drum without strips. Previous work by Wes et al (1976a, b) also showed that the transverse mixing coefficient increased with rotational velocity and normal strip height. Mixing times of 46 minutes were measured by Woodle & Munro (1993) for shell shaped particles with a rotational speed of 8.5 rpm. These times were much larger than those observed by Lehmberg et al (1977) even though a higher rotational velocity was used. This lack of agreement clearly indicates the need of further research into this area. Woodle & Munro (1993) derived a correlation to determine the time required to obtain a fully mixed condition using the complete mixing time of a certain material and the ratio of friction factors of the two materials:

$$\frac{t_1}{t_2} = \left(\frac{\mu_1}{\mu_2} \right)^{1.3} \tag{3.3}$$

where t_1 and t_2 were the respective mixing times and μ_1 and μ_2 were the friction coefficients of the material. This equation is only applicable for the same experimental conditions with different materials. The mixing dynamics in these experiments were at a constant rate until the steady state was reached. A random distribution was observed at the end of mixing due to the stochastic nature of mixing.

A combined model of mixing and segregation was developed by Boateng & Barr (1996a) for a binary mixture. This model calculated the concentrations of "flotsam" and "jetsam" in a series of control volumes and from this the movement of particles were calculated with respect to bulk flow, diffusion and segregation. This model required the knowledge of concentration gradients across the bed, segregation flux coefficient and the diffusion coefficient. The focus of the work by Boateng & Barr (1996a) was on the segregated bed and the heat transfer from the gas phase to the solid bed, which has important implications in calcining kilns but was not so helpful for the mixing and heat transfer between the granular material. The dynamics of mixing and segregation were not modelled and the model was only effective for the prediction of the final distribution of particles in a rolling bed.

The effect of mass ratio on segregation was studied by Ristow (1994) using equal sized particles of different densities. It was shown that the segregation velocity increased proportionally with the logarithm of the mass ratio of the particles. Furthermore, as this mass ratio was increased the final circulation zone of the segregated material was closer to the rotating centre of the bed. Significant density ratios were required to create a segregated core.

Clément et al (1995) carried out segregation work in a two dimensional experiment. They simulated the segregation by tracing the position of a single particle in a thin transverse section. A core was formed when the tracer particle was smaller than the bed particles. A trace close to the wall was formed when the tracer particle was larger than the bed particles. Perfect distribution of the tracer particle was observed when the tracer particle was the same size as the bed material. It should be noted that in their experimental work the bed material consisted of 1.5 mm steel spheres and the tracer particles were 1.0, 1.5 and 2.0 mm spheres respectively. The operating regime of the bed was the rolling regime, which they described as the rotational velocity where a surface avalanche started. For their 160 mm inner diameter cylinder and approximately 40% loading, this velocity was 1/3 rpm. Furthermore they proposed a parameter to characterise the segregation. This was the typical segregation length with a sign indicating the direction of segregation, i.e. towards or away from the centre of the bed as illustrated in Figure 3.3. This correlation needs to be further investigated since it only involved three particle sizes and no changes in particle densities or friction coefficients.

Cantelaube et al (1997) expressed the extent of segregation by an order parameter P_0, which was a measure of the normalised area of the segregated material in a reference cluster. This parameter equalled 1 for a fully segregated system and 0 for a homogenous system. The order parameter as a function of time, $P_0(t)$, was:

$$P_0(t) = 1 - e^{-\frac{t}{\tau}} \tag{3.4}$$

where t was the time passed and τ characterised the kinetics of segregation. From this correlation it was shown that the segregation time constant was independent of the concentration of fines. Furthermore, Cantelaube et al (1997) stated that the

segregation time constant was not dependent on the rotational velocity. It was quite unclear what was meant since this was contradictory to the experimental results of Williams & Khan (1973) and Pollard & Henein (1989) who showed that segregation was dependent upon the rotational velocity of the drum. The segregation was observed to be very fast, with a nearly complete segregated cluster forming within a single drum revolution. The core formation and rapid segregation was in agreement with the results from Pollard & Henein (1989). Cantelaube et al (1997) described the active layer as a fluctuating sieve allowing the smaller particles to percolate causing segregation.

In summary, a number of studies have been reviewed in this section of the thesis. Much of this work was carried out to determine the mixing and segregation in the transverse section of a rolling bed. Various models available but each has its own designated purpose. Most of the models in the literature are only qualitative and there is significant disagreement between the results of various authors. This indicates that more research is required in this area, especially with respect to quantifying the mixing and segregation and relating the models back to various operational parameters of a rotating kiln.

3.2 AXIAL MOTION IN A ROTATING DRUM

Models of motion in the axial direction of a rotary kiln often assume that the bed is perfectly mixed, or isothermal in heat exchange calculations, across any transverse section. This assumption was applicable since the radial dispersion was many magnitudes of order greater than the axial dispersion (Kelbert & Royere, 1991).

3.2.1 Motion in the axial section of a rotating drum

Pickering et al (1951) observed that the movement of particles down the inclined plane of a rotary drum was strongly influenced by the friction of the bed. Solid movement in a rotary kiln was due to the horizontal inclination of the top surface of the bed. Kramers & Crookewit (1952), Hogg et al (1974) and Kelbert & Royere (1991) reported that the axial motion can be represented as a slow plug flow in the

stagnant zone and it was shown that material passes along the axis due to the solids rolling at an incline from the top surface. The resulting combination of transverse motion and movement of particles down the axial incline results in the particles following a pseudo helical trajectory as shown in Figure 3.6.

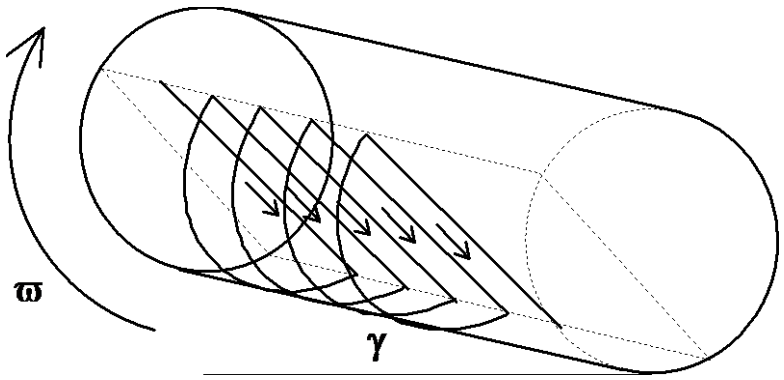

Figure 3.6: Schematic illustrating the pseudo-helical trajectory of particles through a rotary kiln.

A general relation to determine the axial velocity was derived by Perron & Bui (1990), by considering the bed as a continuum, with the only unknown parameter being the apparent viscosity of the bed. This predicted the average axial velocity but cannot be used to determine the velocities of individual particles in different paths. Boateng & Barr (1996a) considered the axial flow as a constant flux that only occurred in the active layer as the stagnant layer was densely packed. In subsequent work, Boateng & Barr (1997) found that axial motion was influenced by the active layer depth and the drum rotational velocity.

The elutriation of fines from a rotary kiln may be significant if a large gas phase velocity was used. Fines elutriation was studied by Tackei et al (1989, 1990) and may have important implications for the elutriation of particles from the top surface of the bed, especially in the case of a gas fired kiln due to the high gaseous volumetric throughput.

3.2.2 Residence times in rotating kilns

The residence time in a rotary kiln was determined from the rate of axial transport in the kiln, which in turn is dependent upon the rotational velocity of the kiln.

Predictions of residence times are important for quality control of the products. Axial transport in the rotary kiln closely resembles plug flow as shown by the tracer experiments of Pickering et al (1951), Rutgers (1965a, b), Ray et al (1994) and Sze et al (1995). A tracer experiment generally involved charging the rotary drum with a certain type of material. After the solids flow in the kiln was well established the feed was changed to a new material with different visual properties but similar characteristics such as size, density and friction. Usually only a pulse of the different material was considered. In order to compare residence times under various conditions, three parameters were suggested by Sai et al (1990). These were the mean residence time of the pulse of solids, the variance and the skewness of the residence time distribution. Rutgers (1965b) reported that for a slumping bed the residence time was 1.7 times that of a rolling bed. However this figure should only be used as an approximation since there is a wide range of rolling velocities.

The residence time of solids in a rotating drum was found by Pickering et al (1951) to be dependent on the inclination of the drum, the rotational speed of the drum and the material flow rate. An increase in the rotational velocity resulted in a decrease of the measured residence time in the rotary kiln (Lebas et al, 1995).

Pickering et al (1951) and Hogg et al (1974) observed that the residence times of smaller particles were longer than for larger particles due to the segregation of the smaller particles. These segregated particles travelled through the kiln at a slower axial velocity. Lebas et al (1995) also observed this behaviour for finer material.

Most of the time of passage determinations were not valid for rotary kilns with restricted discharge ends. The effect of the addition of such constrictions was estimated by Saeman (1951) and Sai et al (1990) and methodology suggested for the solution of residence time across a constriction. The flow rate through a constriction determined the capacity of the kiln since the mass flux in the axial direction was assumed constant to maintain the mass balance. Furthermore, Kramers & Croockewit (1952) considered the end constriction as a correction for the total hold up of the kiln calculated with no end restriction.

The ratio of axial to perpendicular movement for rolling drums was derived by Kramers & Crookewit (1952) and was dependent upon the angle of repose, the angle of inclination and the gradient of axial bed height. The residence time of the solids in the drum was calculated by dividing the kiln length by the axial displacement velocity. Saeman (1951) also found that the axial transport per bed revolution was dependent on the particle radius. This indicates that particles closer to the centre of the bed had different residence times compared to particles near the wall and this was confirmed by Hogg et al (1974). A common parameter required to determine the residence time in the drum was the axial displacement of the particle per bed revolution of the rolling bed. This was directly dependent upon the horizontal incline of the bed. Papadakis et al (1994) reported that this displacement was more pronounced in cataracting drums where the solids were lifted above the bed and upon return to the bed, their collisional energy was converted into rolling energy. This enhanced the axial particle movement as shown by Sherritt et al (1993, 1994).

3.2.3 Mixing and segregation in the axial direction

Axial mixing is considerably greater for inclined drums than for horizontal drums because of the extra shear force experienced by the particles in the inclined drum due to the inclination of the drum (Rutgers, 1965a). Maximum throughput occurs when the bed height is equal to the bed radius as this ensured a maximum active surface area, which is responsible for the axial transport and mixing. The rates of axial mixing follow either first or second order dynamics and Rutgers (1965b) found this rate is dependent on the particle size and solids loading. By introducing flights into the kiln, a reduction in residence time was observed by Rutgers (1965a). This resulted in larger axial displacements of particles per bed revolution for cataracting beds compared to rolling beds. The use of conical outlets with low friction factors caused local mixing and increased the axial dispersion coefficient.

Segregation in the axial direction was studied by Henein et al (1985) and three forms of axial segregation were suggested as shown in Figure 3.7. Radial segregation, banded segregation and end-longitudinal segregation are the three forms of axial segregation. Transverse segregation was observed to be 2 to 4 orders of magnitude

faster than axial segregation and thus has been studied in greater detail. Banded and end-longitudinal segregation depends on the angle of repose of the particles used. These configurations were also observed by Donald & Roseman (1962) but they were referred to as "de-mixes". The mixing and segregation mechanisms described in Chapter 2 also apply to the axial plane.

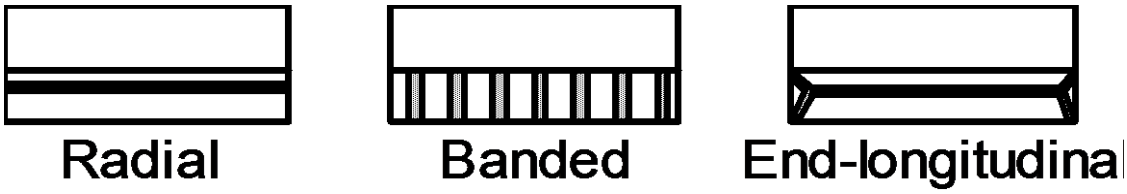

Figure 3.7: Schematic showing axial segregation patterns (Henein et al, 1985).

Sai et al (1990) found that the axial mixing was dependent on the angle of repose of the material, the inclination of the kiln, the rotational speed and the bulk density of the material. Rutgers (1965b) used the Bodenstein number to determine the dispersion of solids in residence time determinations and showed that a uniform relationship exists between the longitudinal dispersion and the total number of bed revolutions. Kelbert & Royere (1991) found that radial mixing was approximately 20 times faster than axial mixing but contributed little to the residence time distribution of the solids. The mixing in the axial direction was determined using an ideal mixer approximation for the active layer and a plug flow element with no mixing for the stagnant zone. The total length required was determined for a binary mixture by varying the feed ratio to each of the above systems. Mixing in the axial direction in a rolling bed was mainly governed by diffusion and experiments carried out by Kohring (1995) determined the axial diffusion coefficient by changing rotational velocities. Increasing the rotational rate increased the rate of diffusion of solids.

3.3 HEAT TRANSFER IN ROTARY KILNS

One of the most important applications of rotary kilns is to transfer heat to or from the bed of solids. The heat transfer studies carried out by Barr et al (1989a, b) and Boateng (1993) focused on calcining kilns where the heat transfer occurred from the gas phase to the rolling bed. Detailed studies of heat transfer between individual

particles, such as the heat transfer mechanism used in the AOSTRA-Taciuk Processor, were not found in the literature.

3.3.1 Heat transfer paths in the transverse direction of a rotary kiln

Heat transfer paths in a rotary kiln, as defined by Barr et al (1989a, b), are shown in Figure 3.8. These paths included: 1) heat transfer through conduction between the wall and the bed of solids, 2) heat losses from the outside wall of the kiln, 3) heat transfer between the inside walls of the kiln via radiation, 4) radiation heat transfer from the hot gas to the kiln walls, 5) radiation heat transfer from the hot gas to the bed of particles, 6) radiation heat transfer from the kiln walls to the gas phase and 7) radiation heat transfer from the kiln walls to the bed of solids.

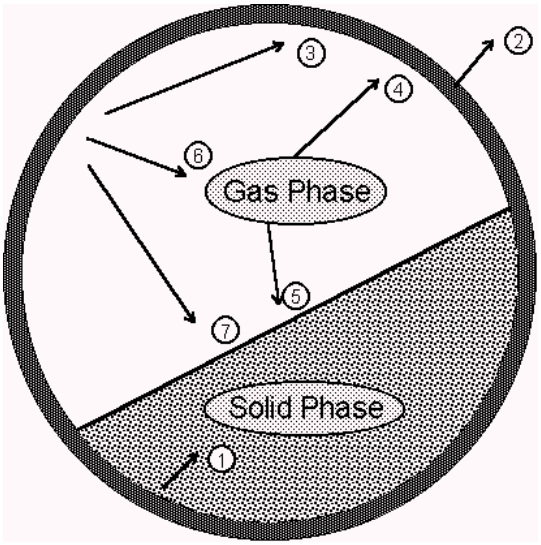

Figure 3.8: Heat transfer paths in the transverse direction of a rotary kiln (Barr et al, 1989a, b).

3.3.2 Review of rotary kiln heat transfer modelling

Barr et al (1989a, b) measured the temperature profile of the wall in a gas fired rotating kiln to predict the heat transfer to a rotating bed. They found that initially rapid heating existed in the kiln and that the ratio of the heat input to the bed to the heat loss from the bed was dependent on the ratio of the exposed bed surface to the exposed wall surface. Depending on the gas temperatures, the heat transfer from the wall covered by bed to the bed was generally much less than the overall heat transfer rate to the bed. In their experiments the free board temperatures were in the vicinity of 1700 K, which indicates that radiation was the most prominent heat transfer mechanism. Conduction from the cooler walls to the bed represented a secondary heat exchange. Furthermore, they found that the final temperature of the bed material was coupled closely to the inside surface temperature of the rotary kiln refractory. In calcining kilns, Barr et al (1989b) showed that a long residence time was required to obtain a product of uniform quality.

Kelbert & Royere (1991) modelled the overall heat transfer to a bed of particles in a rotary kiln by considering the bed as two zones. The heat transfer to the mixing zone or active layer was the result of the heat flux from the gas phase onto the active surface minus the heat transfer to the bulk in the stagnant layer through conduction. Heat transfer into the stagnant layer was considered to be due to conduction from the walls and conduction from the active layer. Mean transverse section temperatures were calculated from the heat transfer. Axial temperature profiles were calculated for different number of transverse sections and axial mixing parameters. An optimum set of parameters was found to allow a satisfactory solution of the axial temperature profile. However, the model presented did not allow for temperature gradients across the transverse section of the bed.

Boateng & Barr (1996b) developed a two dimensional grid to determine the temperature profile across the transverse section of the bed of solids in a rotary kiln. This two dimensional thermal model allowed the effects of mixing and segregation to be examined. They found that in typically well mixed bed the thermal conductivity of the bed increased due to particle motion. As the rotational velocity was increased, the

bed became more mixed and the temperature of the bed became more uniform. In a segregated bed, they found that temperature non uniformities existed within the bed. This model did not predict the dynamic temperature profile of the bed and only illustrated the steady state temperature configuration.

Leger et al (1993) proposed a simple model for the heating of freshly fed cold material into a rotating kiln. They also found that the heating of this cold material was rapid due to the mixing with the hot material.

Yang & Farouk (1997) developed a quasi three dimensional heat transfer model based on their granular flow model. Firstly, the axial temperature profile was determined and from this the temperature gradient at any cross section could be calculated.

3.4 SCALE UP THEORY.

Rose (1959) indicated that the rate of mixing was proportional to the power absorbed by the bed of solids. From this he derived that the mixing rate, which included both mixing and segregation, was dependent on the square root of the drum diameter.

Rutgers (1965a, b) defined dynamic similarity of rolling beds to occur at equal Froude numbers. This was extended by Henein et al (1983a) to also include the ratio of the drum diameter to the particle diameter and equal percent loading so that the mixing regime could be determined. These scale up criteria were only applicable to determine the flow regime of the bed.

Nityanand et al (1986) used the Froude number and the ratio of the fine particle diameter to the coarse particle diameter to scale up transverse segregation. Pollard & Henein (1989) showed that segregation occurred faster in larger rotating drums compared to smaller drums rotating at the same velocity. Their segregation rate was scaled using:

$$S_n = a.Fr^b \qquad (3.5)$$

where S_n was the normalised segregation rate, a was a constant, which was dependent on the particle size ratio and the particle shape and b had a constant value of approximately 0.5.

Williams & Khan (1973) made the important observation that in order to scale results from laboratory sized equipment to industrial sized equipment, the movement of the particles in the test must represent those in the industrial mixer. Previous scaling work as defined in this section focused on dynamic similarities of the drum rather than similar conditions for the particles.

3.5 CHAPTER SUMMARY

The rotating drum open literature was reviewed in this chapter. Firstly, the transverse bed section was considered and the rolling regime was found to be the most important motion regime in a rotating drum with respect to mixing, segregation and heat transfer. The active layer of the rolling regime was described and considered to be of utmost importance in modelling of the solid behaviour in a rotating kiln. Active layer proportions in the literature ranged from 10 to 50% of the bed height. Various attempts were made to characterise the active layer but the use of different solids or experimental conditions was shown to affect the active layer proportion. Thus it is important to characterise the active layer of the rolling regime in any experimental study carried out in a rotating kiln.

Previous work on the mixing and segregation in the rolling bed was also described. Only a few experimental studies were found in the literature and these studies did not cover a significant range of experimental variables. Wide variations in experimental results and incomplete disclosure of experimental conditions made it impossible to utilise those results to validate a dynamic rotating kiln model. The models derived to predict the mixing and segregation in a rotating kiln were limited to qualitative models. The need for a quantitative model applicable for a wide range of experimental conditions is apparent.

Literature regarding the axial movement was reviewed. This showed that the behaviour in the axial direction was a secondary process, dependent on the granular behaviour in the transverse direction.

As rotating kilns were often used in heat transfer applications, models to predict the heat transfer to the solids were also described. These models were limited to heat transfer from the gaseous phase above the bed to the solids bed. A detailed model of the heat transfer between the granular materials of the solid bed was not found in the literature. This is partly due to the lack of quantitative models to describe the mixing and segregation of granular materials in a rolling bed. The development of such a heat transfer model is necessary to predict the behaviour of the retort zone of the AOSTRA-Taciuk Processor.

Only a small amount of research was found where experimental results were used to predict the behaviour in industrial rotating kilns. Most of the scaling factors were functions of the Froude number. However these scaling parameters were only suitable to determine the motion regime and not the behaviour of the granular flow so that the mixing and segregation can be predicted. Suitable scaling factors need to be derived to apply models derived from laboratory sized equipment to industrial equipment.

The following chapters will be devoted to the objective of the thesis as set out in Chapter 1.

CHAPTER 4

Experimental design.

In this chapter the experimental materials, the design of the experimental equipment and the experimental procedures are described.

4.1 PARTICLE AND GRANULAR MEDIUM CHARACTERISATION

Oil shale from the Stuart oil shale deposit, Gladstone, Queensland, Australia was used in this work. The particle size distribution and particle size ranges for the oil shale are shown in Table 4.1. In the AOSTRA-Taciuk Processor, described in Chapter 1, Stuart oil shale will be mixed with recycled combusted spent shale. The physical properties of this combusted spent shale were also measured and shown in Table 4.1.

			Stuart Oil Shale[1]		Combusted Spent Shale[2]	
Maximum Particle Size (mm)	Minimum Particle Size (mm)	Mean Particle Size (mm)	% Retained	Cumulitative (passing)	% Retained	Cumulitative (passing)
	6.30	6.30	0.10	99.90	0.10	99.90
6.30	3.86	5.08	3.30	96.60	17.20	82.70
3.86	3.02	3.44	1.50	95.10	5.70	77.00
3.02	2.00	2.51	18.40	76.70	17.80	59.20
2.00	1.40	1.70	29.50	47.20	11.80	47.40
1.40	1.04	1.22	5.20	42.00	8.80	38.60
1.04	0.60	0.82	19.00	23.00	11.00	27.60
0.60	0.00	0.30	23.00	0.00	27.60	0.00

NOTES: 1) Stuart oil shale mean particle size is 1.47 mm.
2) Stuart combusted spent shale mean particle size is 2.00 mm.

Table 4.1: Particle size distribution of Stuart oil shale and combusted spent shale.

The orange and black shale, as described later in this chapter, is the oil shale which was coloured before being used in the mixing and segregation experiments.

4.1.1 Physical properties of Stuart oil shale

4.1.1.1 Particle sizes

The raw material was sieved into various size fractions as specified in Table 4.1. This particle size distribution was representative of the particle size distribution to be used in the AOSTRA-Taciuk Processor (personal communication, Southern Pacific Petroleum). The bulk sample was sieved into 8 size fractions. Only 0.10 % of the material was greater than 6.30 mm and the less than 0.60 mm size fraction was too small to be used in the experiments due to its electrostatic forces. The remaining six size fractions were used in the experimental work. The raw shale and combusted spent shale mean particle diameters were also calculated. The mean particle diameter for the raw shale was 1.47 mm and the combusted spent shale mean particle diameter was 2.00 mm. The particle size difference between the two materials may have important implications in the operation of the AOSTRA-Taciuk Processor due to the possible segregation of the finer material as described in Chapters 2 and 3.

4.1.1.2 Static angle of repose

The static angle of repose of a material is the angle of the slope of a heap when the material was poured into a heap. This is representative of the static particle-particle friction coefficient. In the experiments reported here the static angle of repose was measured as the maximum inclination of the bed in the rotating drum prior to slumping or rolling. This method was similar to the formation of a heap but the angle of repose was measured at the glass surface of the drum. The static angle of repose was measured for the raw shale and the coloured shale. It was found that there was negligible difference in the angle of repose for the different materials for a particular particle size. This is shown in Table 4.2. The measured static angle of repose increased for larger particles. However, Donald & Roseman (1962) suggested that smaller particles had a greater angle of repose due to the larger surface area of smaller particles, compared to larger particles and this increased the inter particle friction. On the other hand, the measurements of the static angle of repose by

Pollard & Henein (1989) show that the angle of repose was independent of particle size.

In this work, the smaller particles had less penetration into the bed of solids and were not able to support as much weight when compared to the larger particles. This is due to better particle-particle interlocking of the bed when using the larger particles. This indicates that the larger particles would form a bed that required more potential energy to overcome this interlocking. This led to the higher static angles of repose measured for the larger material.

Material Description	Size Range (mm)	Mean Particle Size (mm)	Static Angle of Repose°
Raw Shale	+3.86 - 6.30	5.08	38
Raw Shale	+3.02 - 3.86	3.44	36
Raw Shale	+2.00 - 3.02	2.51	34
Raw Shale	+1.40 - 2.00	1.70	32
Raw Shale	+0.60 - 1.04	0.82	31
Black Shale	+2.00 - 3.02	2.51	33

Table 4.2: Static angle of repose of raw and coloured shale.

4.1.1.3 Bulk density

Both the "loose" and the "tapped" bulk density were determined for each of the materials and particle sizes and these results are shown in Table 4.3. The "loose" bulk density was obtained by measuring the nett weight of material in a container of fixed volume of 1 litre. The material was poured into the container and the excess scraped off. A similar method was used for the "tapped" bulk density but the container was continually tapped whilst being slowly filled ensuring a better packed volume. The bulk density measurement was similar to the "bulk density determination for peat" method as described in ASTM D4531-86 with the exception of using a larger volume. The "tapped" bulk density was taken to be representative of the bulk density of a well packed bed of particles. In all cases the "loose" bulk density was approximately 90% of the "tapped" bulk density. It was assumed that the

bulk density of the material in the rotating drum was representative of the "loose" bulk density.

Loose Bulk Density

		Raw Shale		Raw Ash		Orange Shale		Black Shale	
Size Range (mm)	Mean size (mm)	Density (kg/m³)	St Dev (kg/m³)	Density (kg/m³)	St Dev (kg/m³)	Density (kg/m³)	St Dev (kg/m³)	Density (kg/m³)	St Dev (kg/m³)
-3.86-6.30	5.08	720	3.5	803	11.2	706	6.2	671	3.0
+3.02-3.86	3.44	698	3.7			658	4.9	656	5.9
+2.00-3.02	2.51	700	2.3	777	1.6	651	6.6	634	5.3
+1.40-2.00	1.70	695	1.7	745	2.2	653	28.2	622	2.5
+0.60-1.04	0.82	693	2.3	828	3.4			610	4.6
-0.60	0.30	687	1.1	757	7.7				

Tapped Bulk Density

		Raw Shale		Raw Ash		Orange Shale		Black Shale	
Size Range (mm)	Mean size (mm)	Density (kg/m³)	St Dev (kg/m³)	Density (kg/m³)	St Dev (kg/m³)	Density (kg/m³)	St Dev (kg/m³)	Density (kg/m³)	St Dev (kg/m³)
-3.86-6.30	5.08	799	8.7	873	8.7	786	15.7	746	19.9
+3.02-3.86	3.44	780	7.5			734	5.8	734	9.3
+2.00-3.02	2.51	779	9.3	854	3.6	751	8.5	718	8.1
+1.40-2.00	1.70	770	6.7	840	12.1	746	5.0	706	6.0
+0.60-1.04	0.82	779	14.2	1015	6.4			682	6.8
-0.60	0.30	829	6.0	966	8.3				

NOTES: St Dev is the calculated standard deviation from repeated bulk density experiments.

Table 4.3: "Loose" and "tapped" bulk densities of raw and coloured shale.

The bulk density of a granular medium should be independent of particle size. This is indeed the case for ideal solids, such as smooth uniform density spherical particles. In real particles, composition changes with different particle sizes could change the particle density of that particle size. In turn this could effect the bulk density. The smoothness of different sized particles could also affect the packing properties of that granular medium and change the bulk density. Small variations were noted in both the "loose" and the "tapped" bulk densities of the material with changes in particle size. The raw shale "loose" bulk densities are fairly constant with the exception of the 5.08 mm mean size material whose bulk density is 3% larger than the other particle sizes. This is reflected in the "tapped" bulk density. A possible explanation is that the largest particle size contains a higher concentration of heavier minerals. This seems reasonable, as the larger particles are the particles with the highest impact resistance, which could be due to the presence of denser and more shock resistant ores.

For the coloured material, the density of the largest fraction was once again larger than the density of the other size fractions. The "loose" bulk density was smaller for the coloured shale compared to the raw shale. This was due to the loss of moisture due to the rigorous drying process, which occurred during the particle colouring process as described later in this chapter. The "loose" bulk density differences between the black and the orange shale were small and thus both materials were assumed to behave similarly in the experiments and be only distinguishable by colour.

4.1.2 Chemical properties of Stuart oil shale

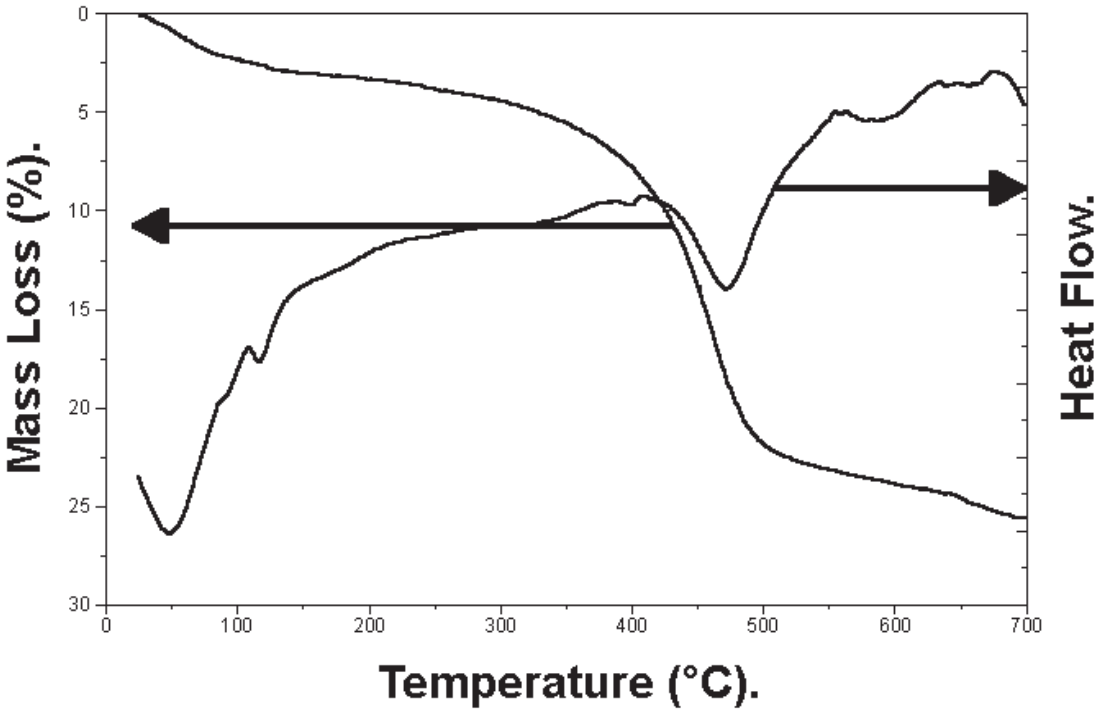

Figure 4.1: Mass loss and heat flow of Stuart oil shale.

Thermodynamic data for the Stuart oil shale was obtained and modelled by Berkovich (1999) using thermo-gravimetric analysis (TGA) and modulated differential scanning calorimetry (MDSC). From this data Berkovich (1999) calculated the rate of weight loss and the specific heat of the shale on an incremental temperature basis. This data was de-convoluted to obtain the different heats of

reaction of the mineral reactions taking place within the oil shale pyrolysis temperature window. Typical thermo-gravimetric and calorimetric results are shown in Figure 4.1. The chemical properties of Stuart oil shale were used to determine volatile evolution rates in the AOSTRA-Taciuk Processor in Chapter 9.

4.1.3 Preparation of the raw materials

Since the experimental method used a visual approach to analyse the solid behaviour, different coloured materials were required. The original colour of the raw shale was light brown. The raw shale size fractions were coloured to represent the two materials in the AOSTRA-Taciuk Processor. A good contrast was required between the colours so that the materials could be easily distinguished. Orange was chosen to colour some of the shale as this highlighted the base colour of the shale. Black was chosen as the other colour due to its high hiding power and its ability to hide particle imperfections. Waterbased inks were used to colour the particles. As can be seen from Table 4.3 both the orange and black coloured material had similar bulk densities and were therefore assumed to only be distinguishable by colour.

The colouring procedure was as follows. Firstly the material was washed to remove the surface dust and then placed on a mesh screen to dry with air being passed above and below the bed of particles to enhance drying. The material was rotated every couple of hours to prevent the formation of aggregates. After drying for 24 hours, the particles were placed in a container with a mesh bottom and dipped into a container of either black or orange ink. This coloured sample was then drained, placed on a drying rack with air passing around the rack and rotated frequently for a period of 24 hours. This colouring procedure was repeated to ensure uniform colour across the shale particles. The material was then stored in sealed bags until required.

4.2 ROTATING DRUM DESIGN

A cylindrical shell of 50 mm thickness and 570 mm inside diameter was used as the transverse section of a rotating drum as shown in Figure 4.2. This section was closed on one side using metal sheeting and enclosed using a removable glass face. A drive shaft was attached to the rear of the drum and this shaft was attached to a DC motor powered by a variable voltage power supply to control the speed. Calibration curves of the drum rotational speed with respect to voltage and drum loading are given in Figure 4.3. Rotational velocities ranged from 2 to 27 rpm over the full voltage range. Inserts for the drum were also acquired to reduce the diameter of the drum to 400 or 200 mm. These inserts were used to test the scalability of the modelling carried out on the 570 mm drum to different sized drums.

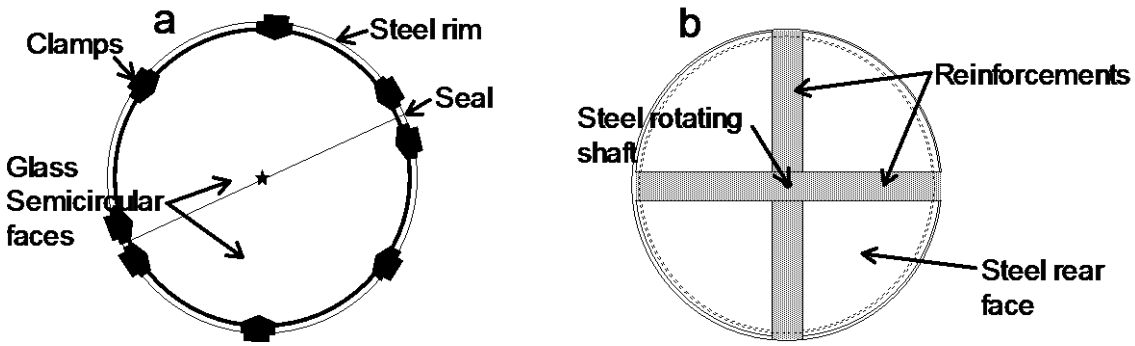

Figure 4.2: Schematic of the rotating drum section - a) front, b) rear.

The removable glass surface consisted of two removable semi circular sections to facilitate loading and unloading of the coloured shale. These glass sections were attached to the cylindrical shell using a clamp and hook arrangement. A silicon strip was placed between the glass panels to ensure a smooth inner surface and to prevent material loss from the transverse section.

The rear surface of the drum and the surrounding cabinet were painted white to provide good contrast between the coloured materials and the experimental apparatus.

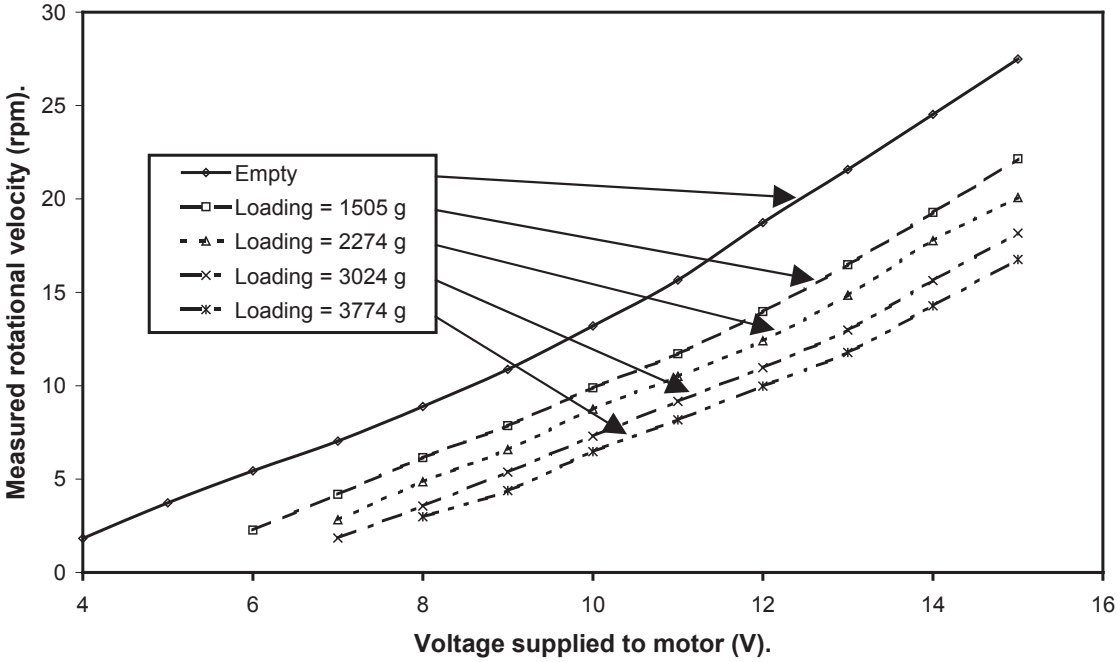

Figure 4.3: Speed calibration curves for the rotating drum.

4.3 IMAGE CAPTURE AND ANALYSIS

A Nikon F3 camera fitted with a Nikon MD-40 motor drive and a Nikon MF-10 data back was used to capture the experimental images. Fiji Sensia ISO 400 bulk film was used. This film was loaded onto a film canister and this canister was loaded into the data back of the camera. In order to prevent the images from being blurred, due to the particle motion, a high shutter speed of $1/1000^{th}$ of a second was used. Since the refresh rate of a flash was not sufficiently fast for the experiments, two 1000W lamps were used to continuously illuminate the experiment during photographic capture. Automatic capture rates were fixed at 3.8 frames per second. The maximum amount of film held in the data back allowed for a total of 240 frames. This indicates that the maximum time for any experiment was approximately 60 seconds.

The negative film was developed and scanned into a personal computer using a Nikon Coolscan LS-1000 film scanner fitted with a Nikon Auto Slide Feeder SF-100 to facilitate the scanning procedure. A maximum resolution scan of 2592 * 3888

(2700 dpi) pixels was carried out on the negative film. These images were cropped and converted to a 256 colour bitmap format using Abode Photoshop V4. Colour enhancement was carried out on these images to increase the contrast between the orange and black material by applying a custom colour palette. This colour palette consisted of 100 colour specifications for the orange material, 100 colour specifications for the black material, 50 colour specifications for the white background of the drum and 6 special colour specifications used in the image analysis work. The images were saved as sequential 256 colour bitmap files.

The enhanced colour images were read into computer memory as numerical arrays for further processing. The analysis methodology differed for the mixing and segregation experiments and will be explained in Chapters 6 and 7, respectively. Details of the bitmap file format and pseudo codes for the conversion of the images to numerical arrays are provided in the appendices.

4.4 PROPOSED EXPERIMENTS

The drum rotational velocity, the drum loading, the particle size and the drum size were varied in experiments in order to investigate the behaviour of the active layer. Characterisation of the active layer for different drum sizes allowed the scaling parameters of mixing and segregation in a rolling drum to be determined. The active layer characterisation is described in Chapter 5.

In the mixing experiments the percentage loading in the drum, the rotational velocity of the drum, the particle size and the ratio of the orange to the black material were varied to measure their affect on the mixing rate and the final amount of mixing. The "layer" configuration was used for the mixing experiments as illustrated in Figure 4.4. The mixing experiments and modelling are described in Chapter 6.

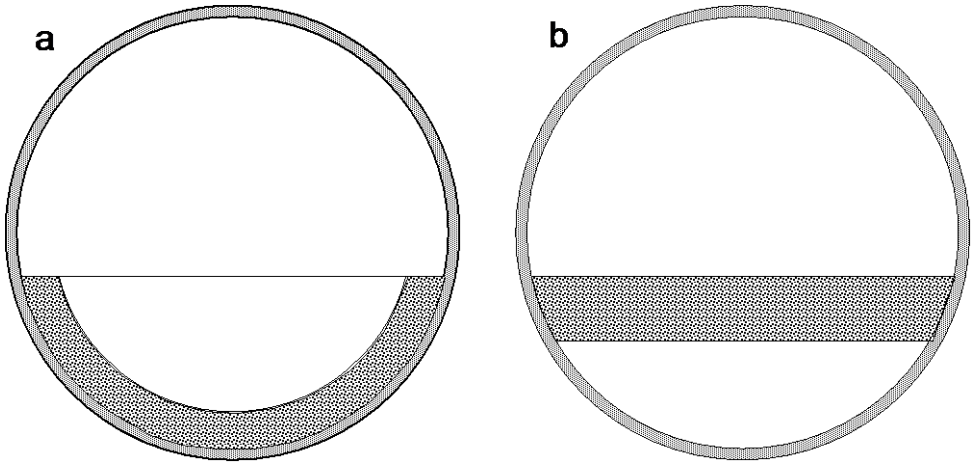

Figure 4.4: Initial bed configurations – a) smile, b) layer.

In the segregation experiments, the rotational velocity and the particle size ratio were varied. The initial configuration for the segregation experiments was a well mixed bed. Chapter 7 describes the different segregation experiments and the modelling carried out for the segregation of solids in a rotating drum.

4.5 EXPERIMENTAL PROCEDURE

Experiments were performed as follows. One of the glass panels was removed and the experimental apparatus was loaded with the solid material according to the experimental specifications. For the mixing experiments, the black material was first loaded to the required height and then the orange material was added to the top of the black material. In the case of the segregation experiments, a well mixed material was added to the drum. After the bed was loaded the glass panel was replaced. Then a photo was taken to determine the initial extent of mixing and/or segregation. The voltage was set to provide the required rotational velocity and the power was switched on to start the rotation of the experimental drum. At the same time, the camera was started and continued throughout the experiment. At the end of the experiment the film was developed and analysed as described in the section on image capture and analysis.

4.6 CHAPTER SUMMARY

In this chapter, the experimental materials and equipment have been described. A description of the experimental rotating drum and the image capture equipment was given. The full experimental method, from colouring of the raw shale to carrying out the experiments was also described. The active layer, mixing and segregation experiments were briefly described and will be described in more detail in the following chapters.

CHAPTER 5

Active layer characterisation.

The literature review in Chapter 3 showed that mixing and segregation in a rolling bed was caused by the granular flow in the active layer. Furthermore, the active layer behaviour was shown to be dependent on the materials used in the experiments. This chapter describes the work carried out to characterise the active layer in a rolling bed as a function of drum diameter, particle diameter, rotational velocity and drum loading. This characterisation will be used in the modelling of the mixing and/or segregation of solids in the rotating drum operating in the rolling regime.

5.1 IMPORTANT ACTIVE LAYER PARAMETERS

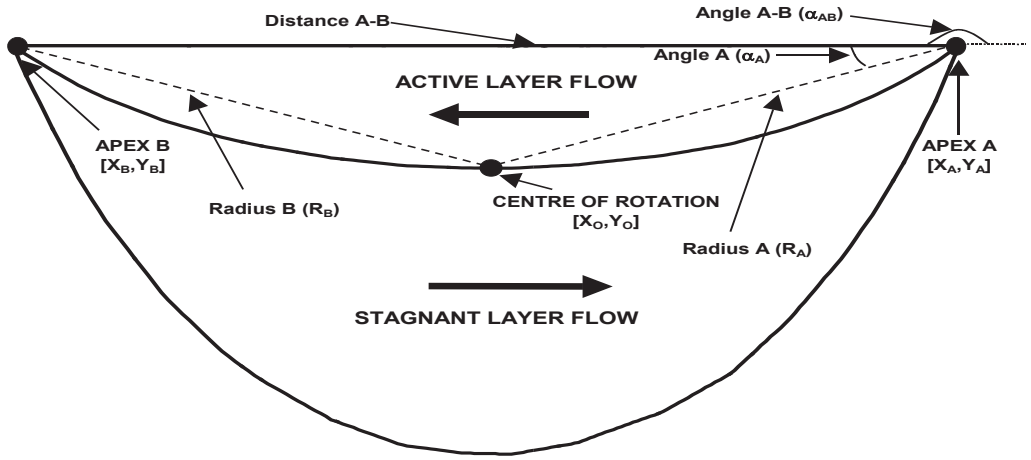

Figure 5.1: Schematic of an ideal rolling bed.

The active layer is the zone of a rolling bed where the particles move relative to each other resulting in mixing and/or segregation. In an idealised case of a rolling bed, shown in Figure 5.1, the active layer is represented by a fraction of the bed height along the exposed surface and the centre of rotation of the bed occurs at the mid chord position. In a real system the active layer is not symmetrical and the rolling bed

becomes wavelike as shown in Figure 5.2, which shows a skewed centre of rotation of the bed. Both figures show the important parameters associated with the active layer as described below.

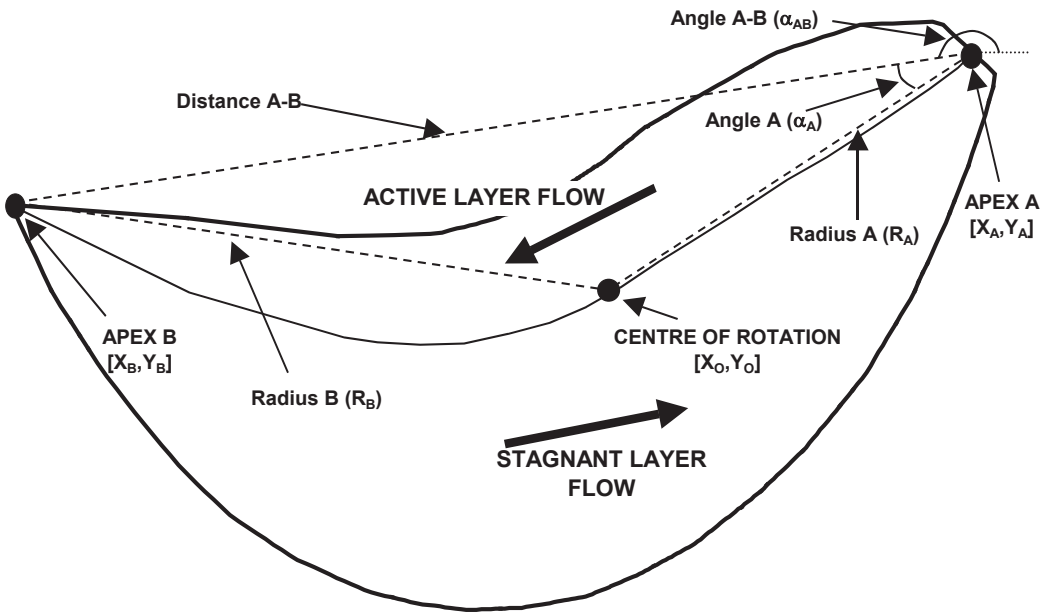

Figure 5.2: Schematic of a real rolling bed illustrating the wave like upper surface shape.

The active layer – stagnant layer interface, indicated by the curved line separating the active and stagnant layers, occurs where the material passed from the well packed stagnant layer into the active layer or vice versa. The active layer flow shows the direction of bulk material movement in the active layer, the stagnant layer flow indicates the direction of bulk flow in the stagnant layer. As can be seen, the material circulates around the centre of rotation of the bed and this centre can be considered as a stationary point in the bed. Apex A and Apex B define the extremities of the bed. These apexes are symmetrical about the centre of rotation for the ideal bed but are asymmetrical in practical situations and thus distinguishing between these apexes becomes important. The distance from Apex A to the centre of rotation of the bed is termed Radius A and Radius B is the distance from Apex B to the centre of rotation. Distance A-B is the distance between the two apexes. Angle A-B, α_{AB}, is the angle between the two apexes and the horizontal axis. Angle A, α_A, is the angle between the Distance A-B and Radius A. The measurement of these parameters was required

for the segregation work. The active layer proportion, X_{AL}, of the bed is the active layer area of the bed divided by the total transverse bed area. Thus:

$$X_{AL} = \frac{A_{AL}}{A_{AL} + A_{SL}} \tag{5.1}$$

where A_{AL} and A_{SL} are the respective transverse areas of the active and the stagnant layers.

5.2 EXPERIMENTAL PROCEDURE

Experiments were carried out to test the effect of drum loading, particle size, particle type and rotational velocity on the above active layer parameters. Collecting the data involved taking photographs of the rotating bed at a slow shutter speed. The motion of the individual particles could be observed in the form of contour lines such as shown in Figure 5.3. Active layer parameters were measured from these photographs.

The active and stagnant layers were cut out from photographs and the sections of the photographs were weighed to obtain a relative size of both the active and stagnant layers. In order to validate the weighing technique, 100 equal sized areas were cut from photographic paper and weighed to ensure that the photographic paper used was of uniform "density". The photographic paper "density" was measured to be $2.4*10^{-4}$ g/mm^2 and the average error of this paper "density" was $1.2*10^{-6}$ g/mm^2 which equals 0.5 % of the photographic paper "density".

Another copy of the photograph was used to determine the location of the centre of rotation of the bed and measure the distances from this centre of rotation to Apex A and Apex B. The centre of rotation is the point around which the material circulates shown by $[X_0,Y_0]$ in Figure 5.3. The other geometric parameters, described above, were also measured from this second copy of the photograph.

Figure 5.3: Example of contour lines in the rolling bed.

Particle size ranges tested varied from 1.70 to 5.08 mm, the drum loading was altered from 10 to 40 % of the drum volume, the rotational speed of the drum was in the rolling regime, from 2 to 25 rpm and three different drum sizes of 570, 400 and 200 mm were tested. Different particle types, such as coloured shale and raw shale, were also tested in the active layer experiments.

5.3 ACTIVE LAYER RESULTS FOR THE EXPERIMENTS IN THE 570 mm DIAMETER DRUM

5.3.1 Active layer proportion

The active layer proportion was determined by weighing the active layer and stagnant layer areas of the photographs taken in the active layer experiments. The active layer proportion was calculated by substituting the area of the layers in Equation 5.1 with the measured weights from the photographs. It was observed that particle size differences and the use of raw shale instead of coloured shale did not affect the active layer proportion of the bed.

The active layer proportion was modelled using all the available data for the 570 mm diameter drum. Figure 5.4 shows the results for the active layer proportion as a function of drum loading and rotational velocity. The empirical equation of best fit consisted of two components, the first component was a logarithmic function with respect to the rotational velocity of the drum and the second component was an exponential correction factor to allow for differences in drum loadings. The correlation is:

$$X_{AL} = 0.0981\ln(N) + 0.00438e^{(0.08744[50-L])} \qquad (5.2)$$

where N was the rotational velocity of the drum in rpm and L was the drum loading expressed as a percentage of the drums volume. Equation 5.2 can be used to determine the active layer proportion in a rolling drum.

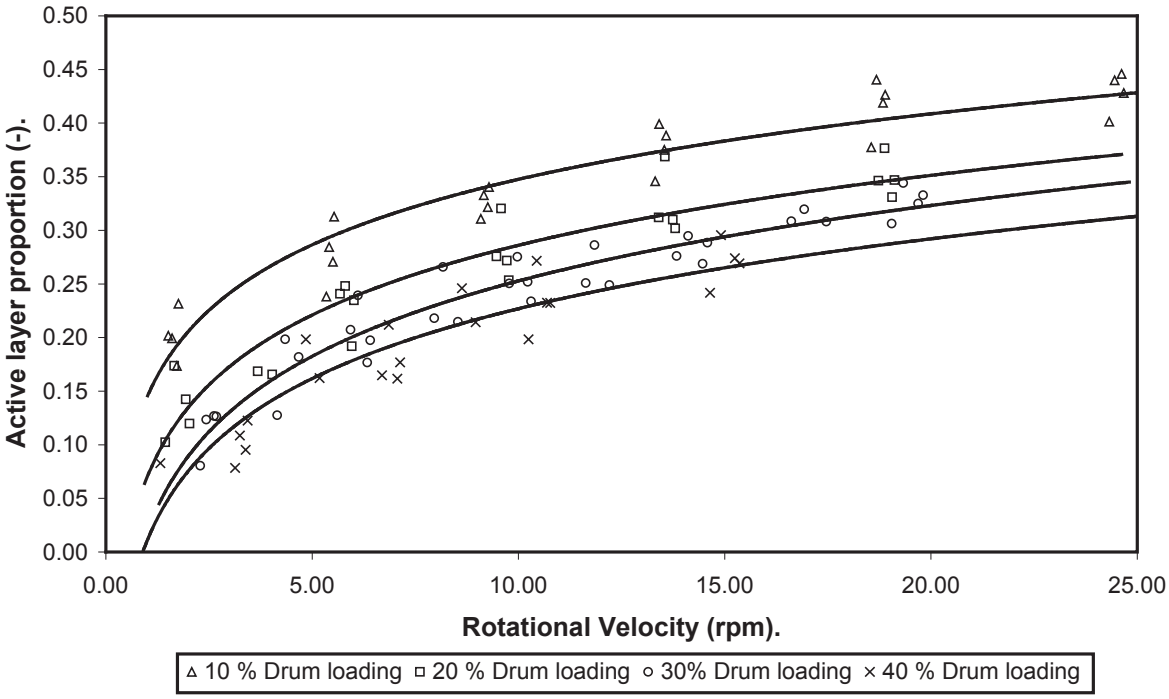

Figure 5.4: Active layer proportion as a function of rotational velocity and drum loading.

The average error for Equation 5.2, determined as the percentage error between the experimentally measured active layer proportion and the predicted active layer proportion from Equation 5.2, was 10 %. This was obtained for the experiments carried out in the 570 mm diameter drum.

5.3.2 Mean velocity and flux of the stagnant layer

At the midchord of the bed, the stagnant layer has a linear velocity profile being zero at the centre of rotation and equalling the drum speed at the drum wall (Nakagawa et al, 1992; Boateng, 1993). This velocity profile is only valid if there is no slip between the wall and the bed. Slip is avoided in the experiments since the drum wall was roughened. Thus the mean velocity in the stagnant layer, $\overline{V}_{SL}$, is:

$$\overline{V}_{SL} = \frac{\int \varpi R dR}{\int dR} = \frac{(\varpi R - 0)}{2} \tag{5.3}$$

where ϖ is the rotational velocity in rad/s and R is the radius of the drum. Figure 5.5 illustrates the velocity profile in the transverse section of a rolling bed in a rotating drum.

For the purpose of this work the flux is defined as the mean velocity of material in a zone multiplied by the transverse area of that zone. The flux in the stagnant layer, Φ_{SL}, is:

$$\Phi_{SL} = \overline{V}_{SL} * A_{SL} \tag{5.4}$$

where A_{SL} is the area of the stagnant layer calculated from the Equation 5.2 and the calculated transverse section area.

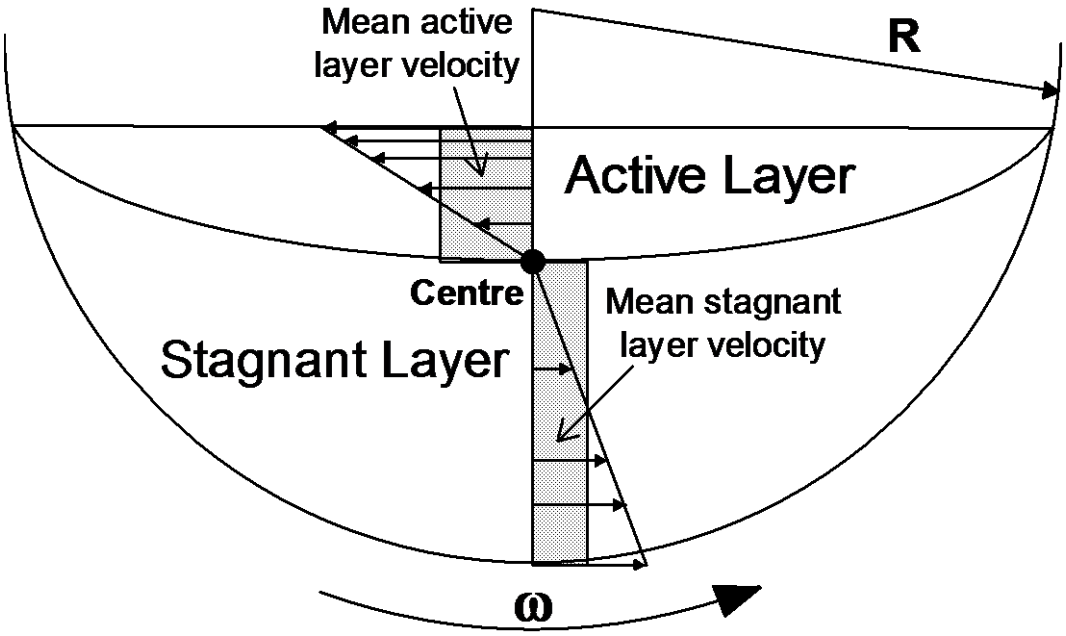

Figure 5.5: Illustration of the transverse section velocity profile as measured by Nakagawa et al (1992) & Boateng (1993).

5.3.3 Mean velocity and flux of the active layer

The mean velocity in the active layer of the bed was considered an important variable in the modelling of both the mixing and segregation in the transverse section. Mass conservation in the bed requires that the flux in the stagnant layer equals the flux in the active layer. The flux in the active layer is:

$$\Phi_{AL} = \overline{V}_{AL} * A_{AL} = \Phi_{SL} \tag{5.5}$$

Thus the mean velocity in the active layer, $\overline{V}_{AL}$, is:

$$\overline{V}_{AL} = \overline{V}_{SL}\frac{A_{SL}}{A_{AL}} = \frac{NR}{15}\frac{\left(1 - X_{AL}\right)}{X_{AL}} \tag{5.6}$$

This correlation was used to calculate the mean active layer velocities in the mixing and segregation experiments and shows the effect of drum size on the mean active layer velocity.

5.3.4 Radius A, Radius B and Angle A

The calculation of R_A, R_B and α_A are required for the segregation analysis since the images for the segregation experiments were taken at a faster shutter speed than the images for the active layer experiments, hence contour lines, such as those of Figure 5.3, were not observed.

Empirical correlations relating Radius A, Radius B and Angle A to the loading of the drum and the rotational velocity of the bed were developed from the photographic measurements. Multiple parameter linear regression was used in all cases. The resulting correlations from the linear regression were:

$$R_A = 168.82 - 2.211N + 2.808L \tag{5.7}$$

$$R_B = 193.61 + 4.606N + 2.403L \tag{5.8}$$

$$\alpha_A = 2.56 + 0.813N + 0.126L \tag{5.9}$$

where R_A is Radius A in mm, R_B is Radius B in mm and α_A is Angle A in degrees. Before the position of the centre of origin could be calculated, the gradient from Apex A to Apex B needed to be calculated. This gradient was referred to as Angle A-B, α_{AB} , in Figures 5.1 and 5.2. In the absence of the contour lines of Figure 5.3 the location of the centre of rotation of the bed can be calculated as follows:

$$[X_O, Y_O] = \left[\left(X_A + R_A(1 + \cos(\alpha_{AB} + \alpha_A))\right), \left(Y_A + R_A(1 + \sin(\alpha_{AB} + \alpha_A))\right)\right] \tag{5.10}$$

where $[X_O, Y_O]$ are the co-ordinates of the centre of rotation and $[X_A, Y_A]$ are the co-ordinates of Apex A. Equations 5.7 to 5.10 are only applicable for the current experimental setup using the 570 mm diameter drum.

5.4 SCALABILITY OF ACTIVE LAYER RESULTS

Experiments were conducted to measure the active layer proportion in different sized drums. Drum diameters of 400 and 200 mm were used. The experimental active layer proportions at different rotational speeds and drum loadings were compared to the active layer proportions calculated from Equation 5.2. The average errors for the different experiments, as shown in Table 5.1, were within the experimental error hence it can be assumed that Equation 5.2 could be applied to determine the active layer proportion for different sized drums.

	Drum Diameter	
Loading	200 mm	400 mm
10%	10.7	6.9
20%	3.4	2.6
30%	3.0	1.4
40%	2.1	4.0

Table 5.1: Deviation, as a percentage, between the experimental results and the predicted results using Equation 5.2 for the active layer proportion in the 200 and 400 mm diameter drums.

From this active layer proportion the mean velocity of the particles in the active layer in any sized drum can be calculated using Equation 5.6. This active layer velocity will be used in the modelling as a scaling parameter in line with the observations of Williams & Khan (1973) who found that suitable scaling parameters needed to represent the movement of particles. The literature showed that the active layer is responsible for mixing and segregation in a rotating kiln. Thus the active layer should be included as a modelling parameter for the modelling of mixing or segregation in a rotating drum. By incorporating the active layer properties the derived model can then be applied to predict the behaviour in different sized rotating drums by calculating the active layer velocity of the different sized drum, such as industrial rotating kiln.

5.5 CHAPTER SUMMARY

In this chapter the active layer has been characterised. A correlation was derived to predict the active layer proportion and the mean velocity of particles in the active layer. This correlation was dependent on the rotational velocity and the drum loading. The geometry of the active layer was also studied to allow the centre of rotation of the bed to be determined and will be used in a later chapter to develop a solid segregation model. The chapter was concluded with the derivation of suitable scaling parameters to allow the mixing and/or segregation of an industrial rotating kiln to be determined based on experiments carried out in laboratory sized equipment.

CHAPTER 6

Mixing in the transverse direction of a rotary drum.

The mixing mechanisms of granular materials were described in Chapter 2. Previous studies revealed that there is a lack of quantifying models to predict both the mixing rate and the final amount of mixing in the transverse direction of rotating drums. In this chapter models will be developed to predict, as a quantitative measure, the mixing rates and the final amounts of mixing so that the mixing of solids in rotating kilns can be predicted.

Before these models could be developed, new experimental methodologies were required. These new experimental methods used image analysis programming to determine the extent of mixing and will also be described in this chapter.

6.1 TRANSVERSE MIXING EXPERIMENTS

The mixing behaviour of solids in the transverse section of a rotating drum was investigated in the mixing experiments. The experimental variables tested were the rotational velocity, the percentage drum loading, the particle size and the material ratio. The rotational velocity, N, ranged from 5 to 19 rpm covering the rolling regime. Drum loadings, L, of 6 to 40% of the total drum volume were used. The particle size range, d_p, was varied from 0.89 to 5.08 mm. Experimental material ratios of the black to orange material were altered from 0.55 to 2.70. The material ratio was set equal to the experimentally measured material ratio unless the experimentally measured material ratio was less than one, in which case the material ratio equalled the inverse of the experimental material ratio.

		Experimental Conditions					
		Rotational Velocity N	Drum Loading L	Particle Size d_p	Experimental Black:Orange	Calculated Black:Orange κ	Configuration
No	Variable	rpm	% Volume	mm	-		
1	Drum Loading	8.0	6	2.51	0.65	1.54	Orange layer on top
2	Drum Loading	8.5	15	2.51	1.07	1.07	Orange layer on top
3[1]	Drum Loading	9.0	25	2.51	1.06	1.06	Orange layer on top
4	Drum Loading	8.0	39	2.51	1.11	1.11	Orange layer on top
5	Rotational Speed	5.2	25	2.51	1.10	1.10	Orange layer on top
6	Rotational Speed	6.8	26	2.51	1.03	1.03	Orange layer on top
3[1]	Rotational Speed	9.0	25	2.51	1.06	1.06	Orange layer on top
7[1]	Rotational Speed	9.8	26	2.51	1.27	1.27	Orange layer on top
8	Rotational Speed	11.7	26	2.51	1.13	1.13	Orange layer on top
9	Rotational Speed	13.9	26	2.51	1.03	1.03	Orange layer on top
10	Rotational Speed	15.1	26	2.51	0.88	1.13	Orange layer on top
11	Rotational Speed	18.5	30	2.51	1.03	1.03	Orange layer on top
12	Particle Size	10.1	25	0.89	1.22	1.22	Orange layer on top
13	Particle Size	10.0	25	1.70	0.98	1.02	Orange layer on top
7[1]	Particle Size	9.8	26	2.51	1.27	1.27	Orange layer on top
14	Particle Size	9.8	26	3.44	1.06	1.06	Orange layer on top
15	Particle Size	8.8	25	5.08	1.06	1.06	Orange layer on top
16	Material Ratio	9.8	26	2.51	0.55	1.82	Orange layer on top
7[1]	Material Ratio	9.8	26	2.51	1.09	1.09	Orange layer on top
18	Material Ratio	9.8	27	2.51	1.36	1.36	Orange layer on top
19	Material Ratio	10.0	25	2.51	1.42	1.42	Orange layer on top
20	Material Ratio	9.8	26	2.51	1.96	1.96	Orange layer on top
21	Material Ratio	9.8	27	2.51	2.70	2.70	Orange layer on top
22	Drum Loading / Particle Size	19.0	20	1.70	1.05	1.05	Orange layer on top
23	Drum Loading / Particle Size	14.3	30	1.70	1.05	1.05	Orange layer on top
24	Drum Loading / Particle Size	11.6	40	1.70	1.05	1.05	Orange layer on top
25	Test	10.0	30	2.51	1.12	1.12	Smile configuration
26[2]	Test	9.7	30	2.51	1.00	1.00	Orange layer on top
27[2]	Test	11.1	30	2.51	1.00	1.00	Orange layer on top

NOTES:

1) These experiments were used for more than one set of variables.
2) Experiment 26 was carried out in a 400 mm diameter drum. Experiment 27 was carried out in a 200 mm diameter drum.

Table 6.1: Experimental conditions for the mixing experiments.

The rotating drum was loaded according to one of the geometries shown in Figure 4.4. For the "layer" configuration, the black material was added first to the drum and a layer of orange material was placed on top of this. In the "smile" configuration, the orange material was added first to form the "smile" and the black material was used to fill the "smile". A photograph was taken of the initial stationary bed. This image was used to calibrate the colours for each experiment. After the experimental drum

was closed, the rotation was started and the camera was set on automatic. An image of the moving bed was taken every 0.26 seconds until the end of the film. This film was then processed and scanned into a personal computer using the equipment described in Chapter 4. The images were analysed to obtain a measure of the contact distance between the two materials, as described below. In all cases complete mixing was achieved within 1 minute.

In this work a quantitative measure of mixing was sought. Hence the contact distance was established. This contact distance represents the one dimensional circumferential contact between the two different materials. Previous work, such as Woodle & Munro (1991), only expressed the mixing qualitatively. In the current work it is desired to simulate an industrial process where heat transfer between different materials is important and hence the use of a quantitative parameter, such as the contact distance, is beneficial since heat transfer between materials is dependent on the amount of contact between those materials.

6.2 EXPERIMENTAL ANALYSIS METHODOLOGY

After the images were scanned into a computer as bitmaps, they were analysed using image analysis software specifically written for this task. Bitmaps are described in Appendix 1 and the pseudo-codes for the image analysis software are included in Appendix 2. The first step of the image analysis involved converting the bitmap file of the image into an array of data. This numerical array represented the colour specifications of each pixel in the image. The colour of each pixel indicated what type of particle was represented by that pixel. Three different colour specifications were considered in the mixing work, these being the black colour type for the black particles, the orange colour type for the orange particles and the white colour type for the background of the drum. The colour specifications were determined from experimental images to ensure that the colour specifications matched the colours of the materials used.

Contact between the two materials occurred if adjacent pixels represented different colour types. The total contact distance could be calculated for either the black or the orange colour specification but the orange colour specification was chosen. Since the contact distance between the orange and the black material was required it did not matter which colour was chosen as the basis. The total contact distance was quantified by calibrating the physical size represented by a pixel in the image. Contact between orange and white pixels was not considered since this did not physically represent mixing of the two materials. White-orange contact signified the presence of an orange particle next to a boundary of the drum and hence provided no contact information.

The mixing image analysis methodology may be best illustrated by means of an example. Figure 6.1 shows an enlarged extract from an image of a well mixed bed. A grid was superimposed to represent the different pixels of a bitmap. P[i,j] represent the pixel in the i^{th} row and the j^{th} column of Figure 6.1. Black pixels were defined as B, white pixels were defined as W and the orange pixels were defined by a numerical value from 0 to 4 on a freckled background. This number indicated the number of contact occurrences between that orange pixel and surrounding black pixels as described below.

The contact distance between the orange and the black particles was calculated using the orange material as a basis. Only contacts between adjacent edges were considered. Adjacent corners of different coloured pixels would only indicate that there was a point of contact and not a distance of contact. Points of contact were not included in the determination of the contact distance between the different coloured materials in the image. Edge to edge contact increased the contact of that image by 1. For example looking at the pixel in column 1 and row 1 of Figure 6.1, P[1,1], which was an orange pixel, the contact between the surrounding pixels and the current pixel was 1 since the only contact with black material was due to P[1,2]. The contact from P[1,2] was not calculated since this was not of the orange type. Moving along to P[2,2], which was another orange pixel, the contact of this pixel was 2 because of P[1,2] and P[3,2] both of which were black. Note that P[2,2] had 2 edge contacts,

which were counted and two point contacts, which were ignored. Contact with the background material was not considered since this was not representative of the mixing between the black and the orange materials. The pixels in Figure 6.1 marked with a W indicated they were of the background type and not relevant to the mixing. The pixels marked with B represented the black material and the orange material is represented in Figure 6.1 by numbers from 0 to 4. These numbers indicate the amount of contact between that orange pixel and surrounding black pixels. Calculating the total contact distance between the orange and the black material for the array as shown in Figure 6.1 indicated a total contact of 61 edges. To convert this to a distance, the resolution of the image was calibrated. The pixels were square and in most cases each pixel side was approximately 0.18 mm but this was different for each experiment due to slight camera adjustments and was calculated for each experiment. Thus a contact distance of 10.98 mm was calculated for Figure 6.1. The same contact distance was obtained if the contact was measured for the black material. This procedure was applied to the whole image and gave a measure of the contact distance between the different materials in the bed for that image.

	Columns														
Rows	**1**	**2**	**3**	**4**	**5**	**6**	**7**	**8**	**9**	**10**	**11**	**12**	**13**	**14**	**15**
1	1	B	B	1	0	1	1	0	0	0	0	0	0	0	0
2	1	2	1	0	2	B	B	1	0	0	0	0	0	0	1
3	B	B	2	2	B	B	2	0	0	0	0	0	0	1	B
4	B	B	B	B	B	3	0	1	1	1	1	0	0	1	B
5	B	B	B	B	B	B	3	B	B	B	B	1	0	1	B
6	1	3	B	2	1	2	B	B	B	B	B	2	0	1	B
7	1	B	B	1	0	1	B	2	1	1	2	B	1	W	W
8	1	B	2	0	0	1	B	1	W	W	W	W	W	W	W
9	1	B	1	0	W	W	W	W	W	W	W	W	W	W	W
10	W	W	W	W	W	W	W	W	W	W	W	W	W	W	W

W	Background or white pixel
B	Black coloured pixel
0	Orange coloured pixel showing
1	the contact with neighbouring
2	black coloured pixels
3	

Figure 6.1: Extract of an image from a well mixed bed.

By analysing all the images using the above procedure and obtaining a contact measurement for each image, the change in mixing contact was determined. Using the image capture rate of the camera, the mixing rates of the experiments were calculated.

6.3 EXPERIMENTAL MIXING RESULTS

Figure 6.2 shows images from a typical mixing experiment. In Figure 6.2a the initial bed configuration is shown. The initial point of mixing was taken at the point where the bed became fully developed as a rolling bed. This occurred a short time after the rotation was started since the material was initially stationary and the upper surface of the bed was horizontal. The initial point of mixing is shown in Figure 6.2b, which clearly shows the wavelike structure of the bed, which indicates the fully developed rolling regime. Figure 6.2c shows the bed after a complete bed revolution after the initial point of mixing. As can be seen the bed has become more mixed. The well mixed bed is shown in Figure 6.2d.

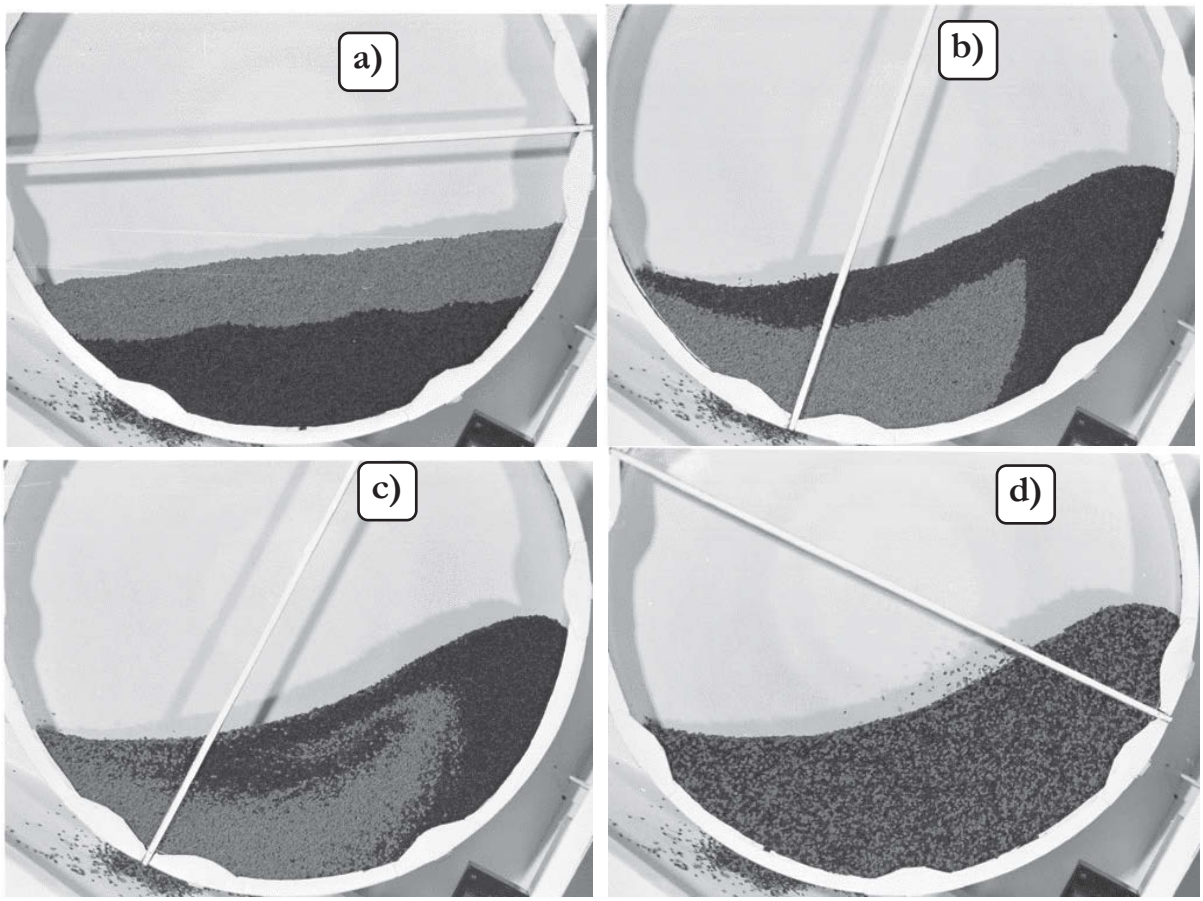

a) initial bed configuration, this image was used to calibrate the colours of the materials, b) initial point taken for the calculation of the mixing rate showing the development of the rolling regime, c) image one complete bed revolution after the initial mixing point showing the widening of the orange material and d) fully mixed bed configuration.

Figure 6.2: Sample photos from a typical mixing experiment.

Figure 6.3 shows the results from a typical mixing experiment. The plot shows the contact distance for a series of images plotted against the experimental time. Both the mixing rate and the final contact distance were calculated for each experiment. The results showed that the mixing occurred at a constant rate. Small fluctuations were observed about the final contact distance. The experimental error of the mixing rate and the final contact distance were also calculated.

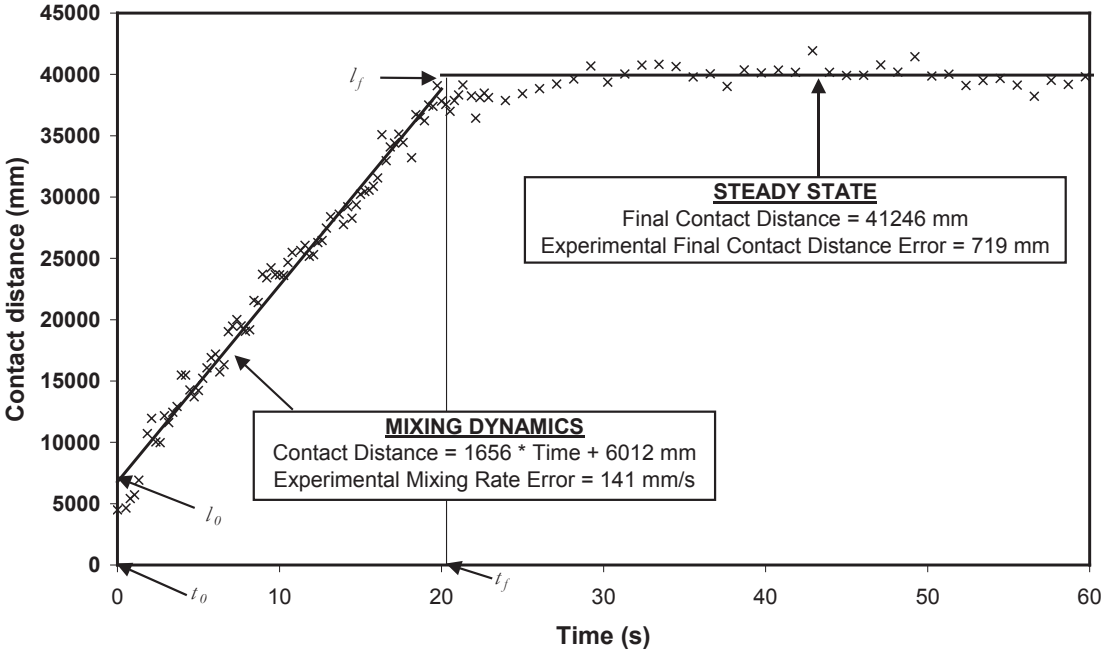

Figure 6.3: Typical results for a mixing experiment, this graph shows the results for experiment 3.

The mixing rate, Γ, was calculated over the linear "mixing dynamics" section of Figure 6.3. The resulting equation was of the following type:

$$\Gamma = \frac{(l_f - l_0)}{(t_f - t_0)} \tag{6.1}$$

where l_f was the final contact distance and l_0 was the initial contact distance, in mm, between the orange and black materials obtained from images similar to Figure 6.2b. t_f was the time when the final contact distance was first reached and t_0 was the time corresponding to the initial contact distance, taken as 0.

Table 6.2 contains the experimental mixing rates and the experimental mixing rate errors as well as the calculated data for the mixing experiments that were used in the modelling of the mixing rate. The experimental mixing rate error was calculated by averaging the relative errors between the overall experimental mixing rate and the mixing rate calculated for the individual data points.

		Experimental Variables		*Calculated and Modelling Variables*				
		Experimental Mixing Rate Γ	**Experimental Mixing Rate Error**	**Active layer Percentage**	**Active layer velocity** $\overline{V}_{AL}$	**Active Layer Parameter** ϕ	**Predicted Mixing Rate From Model**	**Predicted Mixing Rate Deviation**
No	**Variable**	**mm/s**	**%**		**mm/s**	**mm³/s**	**mm/s**	**%**
1	Drum Loading	975	22	41	348	328741	494	49
2	Drum Loading	1326	11	30	576	849801	1277	4
3[1]	Drum Loading	1656	9	25	792	1397108	2099	27
4	Drum Loading	1897	16	22	870	1733693	2605	37
5	Rotational Speed	1296	11	20	623	962611	1446	12
6	Rotational Speed	1984	17	22	703	1193040	1793	10
3[1]	Rotational Speed	1656	9	25	792	1397108	2099	27
7[1]	Rotational Speed	2441	9	26	836	1419802	2133	13
8	Rotational Speed	2440	9	28	911	1666058	2503	3
9	Rotational Speed	2409	12	29	995	1935432	2908	21
10	Rotational Speed	3235	9	30	1045	2004546	3012	7
11	Rotational Speed	3290	7	31	1219	2622433	3940	20
12	Particle Size	3167	15	27	836	1994858	2997	5
13	Particle Size	2665	16	26	830	1805696	2713	2
7[1]	Particle Size	2441	9	26	836	1419802	2133	13
14	Particle Size	1496	9	26	830	1160047	1743	17
15	Particle Size	947	19	25	783	519060	780	18
16	Material Ratio	1654	17	26	838	1180029	1773	7
7[1]	Material Ratio	2441	9	26	836	1503368	2259	7
18	Material Ratio	2010	11	26	842	1398547	2101	5
19	Material Ratio	1845	10	26	830	1330790	2000	8
20	Material Ratio	1502	13	26	841	1119301	1682	12
21	Material Ratio	1271	16	26	842	783465	1177	7
22	Drum Loading / Particle Size	3604	16	35	1068	2350170	3531	2
23	Drum Loading / Particle Size	5183	11	28	1072	2619874	3937	24
24	Drum Loading / Particle Size	3429	9	25	1035	2737878	4114	20
		Minimum	7				**Minimum**	2
		Maximum	22				**Maximum**	49
		Average	12				**Average**	14
25	Test	2113	9	25	893	1674010	2515	19
26[2]	Test	1217	8	25	615	835875	1256	3
27[2]	Test	356	23	26	328	228779	344	3

NOTES:

1) These experiments were used for more than one set of variables.
2) Experiment 26 was carried out in a 400 mm diameter drum. Experiment 27 was carried out in a 200 mm diameter drum.

Table 6.2: Experimental mixing rates and calculated data for the modelling of the mixing rates.

The final contact distance, l_f, of an experiment was taken as the average of the steady state contact distances of the mixing experiment. The experimental error of the steady states was calculated as the average error from this steady state value. Table 6.3 contains the experimental final contact distance and the experimental final contact distance error. The calculated data, used in the modelling of the final contact distance is also shown in Table 6.3 and is described below.

		Experimental Variables		*Calculated and Modelling Variables*		
		Experimental Final Contact Distance l_f	**Experimental Final Contact Distance Error**	**Final Contact Distance Parameter** λ	**Predicted Final Contact Distance from Model**	**Final Contact Distance Deviation**
No	**Variable**	**mm**	**%**	**mm³**	**mm**	**%**
1	Drum Loading	13022	4	164049	8661	33
2	Drum Loading	23457	3	476973	25182	7
3[1]	Drum Loading	41246	2	815327	43046	4
4	Drum Loading	64813	3	1236529	65284	1
5	Rotational Speed	42027	3	809213	42723	2
6	Rotational Speed	43844	4	851471	44954	3
3[1]	Rotational Speed	41246	2	815327	43046	4
7[1]	Rotational Speed	47524	2	775979	40969	14
8	Rotational Speed	44456	2	814924	43025	3
9	Rotational Speed	40254	3	851174	44939	12
10	Rotational Speed	43229	2	826417	43632	1
11	Rotational Speed	44869	3	982466	51870	16
12	Particle Size	65394	6	1031337	54450	17
13	Particle Size	54137	3	970601	51244	5
7[1]	Particle Size	47524	2	775979	40969	14
14	Particle Size	31526	2	666085	35167	12
15	Particle Size	24705	4	369404	19503	21
16	Material Ratio	24765	10	615593	32501	31
7[1]	Material Ratio	47524	2	833473	44004	7
18	Material Ratio	44320	2	766944	40492	9
19	Material Ratio	38388	2	707349	37345	3
20	Material Ratio	30266	4	570588	30125	0
21	Material Ratio	21311	7	338376	17865	16
22	Drum Loading / Particle Size	40047	7	761407	40199	0
23	Drum Loading / Particle Size	60785	4	1142110	60299	1
24	Drum Loading / Particle Size	71198	4	1522814	80398	13
		Minimum	2		**Minimum**	0
		Maximum	10		**Maximum**	33
		Average	4		**Average**	10
25	Test	37500	2	948945	50101	34
26[2]	Test	22148	2	488575	25795	16
27[2]	Test	5399	5	122144	6449	19

NOTES:

1) These experiments were used for more than one set of variables.
2) Experiment 26 was carried out in a 400 mm diameter drum. Experiment 27 was carried out in a 200 mm diameter drum.

Table 6.3: Experimental final contact distances and calculated data for the modelling of the final contact distances.

6.4 ANALYSIS OF THE EXPERIMENTAL MIXING RESULTS

As described in Chapter 3, the transverse section of a rolling bed consists of both an active and a stagnant layer. The active layer is responsible for all the mixing in a rotating drum (Boateng, 1993).

6.4.1 Stepwise mixing behaviour

The first 10 seconds of mixing from Figure 6.3 are redrawn in Figure 6.4. Enlarging the experimental results in this manner showed that the mixing occurred through a series of steps. For experiment 3 these steps were approximately 2 seconds in length and this time equalled the calculated time that the material spent in the stagnant layer during one bed revolution in experiment 3. The time spent in the stagnant layer was calculated from the geometry of the rotating drum, the bed loading and the rotational velocity. An increase in the contact distance occurred when the two different materials entered the active layer together and subsequently mixed. The time spent in the active layer was much shorter when compared to the stagnant layer due to the mass flux conservation of the active and stagnant layers as described in Chapter 5. The magnitude of the steps were approximately constant showing that the mixing rate was indeed constant. As time progressed, the two materials become more mixed and the distinction between the steps was reduced until the steps were not observed at the steady state, ie when all material entering the active layer was well mixed. This stepwise behaviour was sufficient proof to show that the mixing only occurred in the active layer of the bed of solids in a rotating drum and validates the use of the active layer in subsequent modelling.

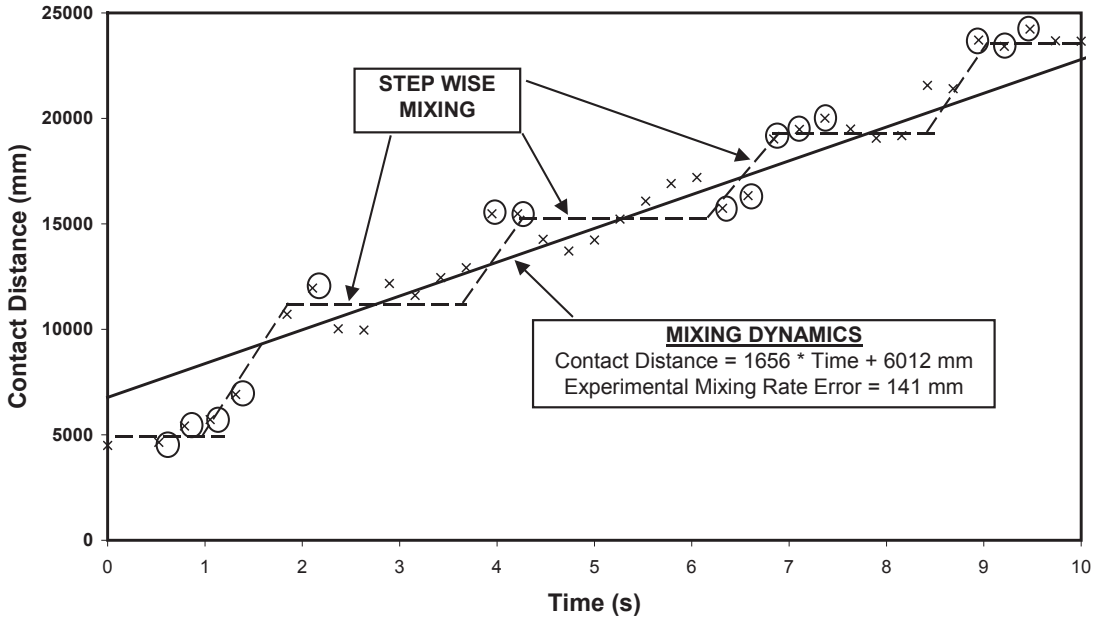

Figure 6.4: Enlarged view of the initial part of Figure 6.3 illustrating the step nature of mixing of experiment 3.

6.4.2 Mixing rates and final contact distances

The mixing rate was observed to be of a linear nature for all the experiments, as shown in Figure 6.3. The effects of the different parameters on the mixing rates and final contact distances are discussed in this section of the thesis. Figures 6.5 to 6.8 illustrate the effects of the different parameters used in the experiments. The dashed lines in these figures represent the mixing rates and the solid lines in the figures represent the final contact distances. The error bars in those figures represent the average experimental errors of either the mixing rate or the final contact distances and will be discussed below.

6.4.2.1 Rotational velocity effects

The effect of rotational velocity, *N*, on the mixing rate is shown in Figure 6.5. A linear increase in the mixing rate was observed by increasing the rotational velocity of the drum. From the active layer proportion correlation, Equation 5.2, an increase in rotational velocity increases the active layer proportion of the bed. Thus at higher

rotational velocities there was more material in the active layer and from the mean active layer velocity correlation, Equation 5.6, this material travels faster within the active layer. This is shown in the active layer velocity column of Table 6.2. This indicated that at the higher rotational velocities there was more material in the active layer and a higher driving force to mix due to the increased velocity. This leads to faster mixing rates at higher rotational velocities as observed in the rotating drum. For the rotational velocity experiments, all the experiments obtained similar final contact distances, as indicated by the horizontal solid line of Figure 6.5. This was expected since similar initial bed configurations were used for each of the rotational velocity experiments. The small differences in the final contact distances were due to the small differences in the initial configurations of the experiments.

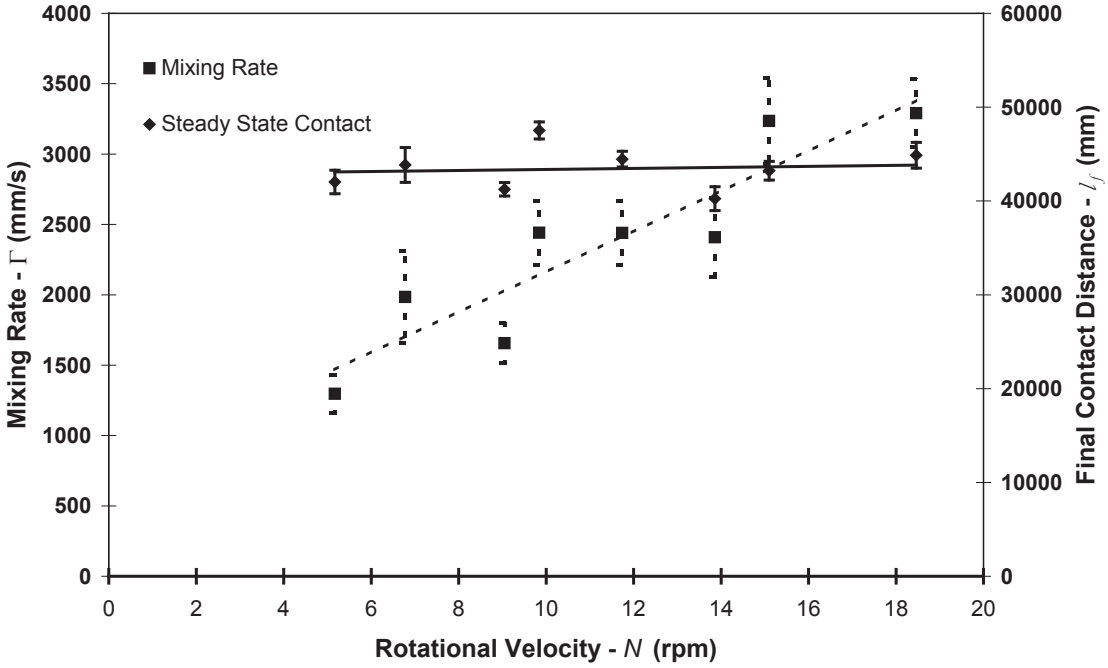

Figure 6.5: Measured mixing rates (Γ) and final contact distances (l) with respect to the rotational velocity (N) of the drum.

6.4.2.2 Drum loading effects

Figure 6.6 shows the mixing results for the drum loading experiments. The mixing rate increased linearly as the drum loading, *L*, increased. This can once again be attributed to the active layer. As the drum loading increases, the active layer proportion of the bed decreased but the actual size of the active layer and the mean

active layer velocity increased. This results in an increased mixing rate as the loading was increased. A linear dependence was observed between the final contact distance and the drum loading in the loading experiments. This was expected since in the presence of more material, a larger amount of contact can be obtained between the materials.

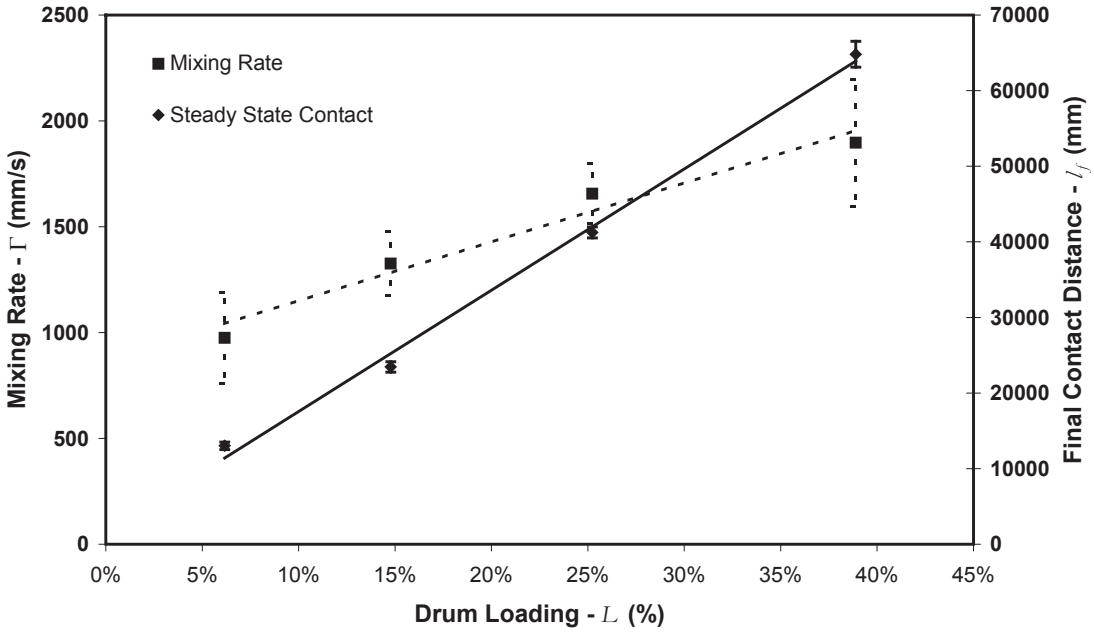

Figure 6.6: Measured mixing rates (Γ) and final contact distances (l_f) with respect to drum loading (L) by percentage volume.

6.4.2.3 Particle size effects

The particle size, d_p, effect is shown in Figure 6.7. This figure shows a linear increase in mixing rate by decreasing the particle size. Since the drum loading and rotational speeds were constant throughout the particle size experiments, the active layer proportion and active layer velocities were also constant and cannot explain the current behaviour. However, a certain volume of smaller particles has a larger surface area compared to an equal sized volume of larger particles. Thus the total possible contact distance in a fixed size active layer would increase with decreasing particle size. This was reflected by the increase in mixing rate for the smaller particles. A higher final contact distance was obtained for smaller particles. A linear dependence was observed between the final contact distance and the particle size.

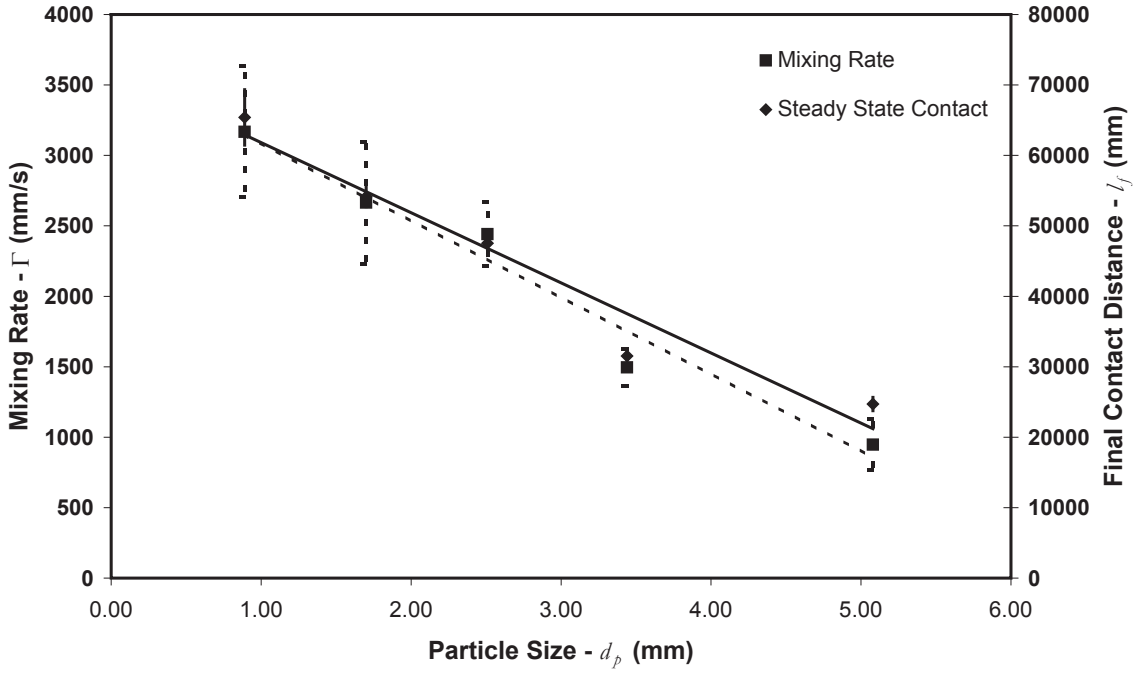

Figure 6.7: Measured mixing rates (Γ) and final contact distances (l_f) as a function of particle size (d_p).

6.4.2.4 Material ratio effects

The results obtained from varying the proportion of the black to orange material in the drum are shown in Figure 6.8. The mixing rate varies linearly over the material ratio range tested. This trend cannot be explained using the active layer properties since the rotational velocity and drum loading were similar for the material ratio experiments resulting in equal mean active layer velocities. As the calculated material ratio increased the mixing rate decreased. This can be explained by considering the total contact distance possible for each of the materials. As the material ratio increased there was an excess of one type of material and a shortfall for the other type of material in the bed, which resulted in a quicker mixing of the lesser material. However if this material entered the active layer uniformly, the tendency to mix in each bed revolution decreased since there was less material to mix. Increasing the ratio of the materials resulted in a linear reduction of the final contact distance in the bed. A maximum final contact distance would be obtained for a material ratio of 1. In this case the total perimeters for the orange or the black material equalled. If the ratio is increased, the perimeter of one material increases but the total perimeter of

the other material decreases. Since contact only occurred between the two different materials, a decrease in the total perimeter of one material would result in a lower final contact distance and this is reflected by the results of Figure 6.8.

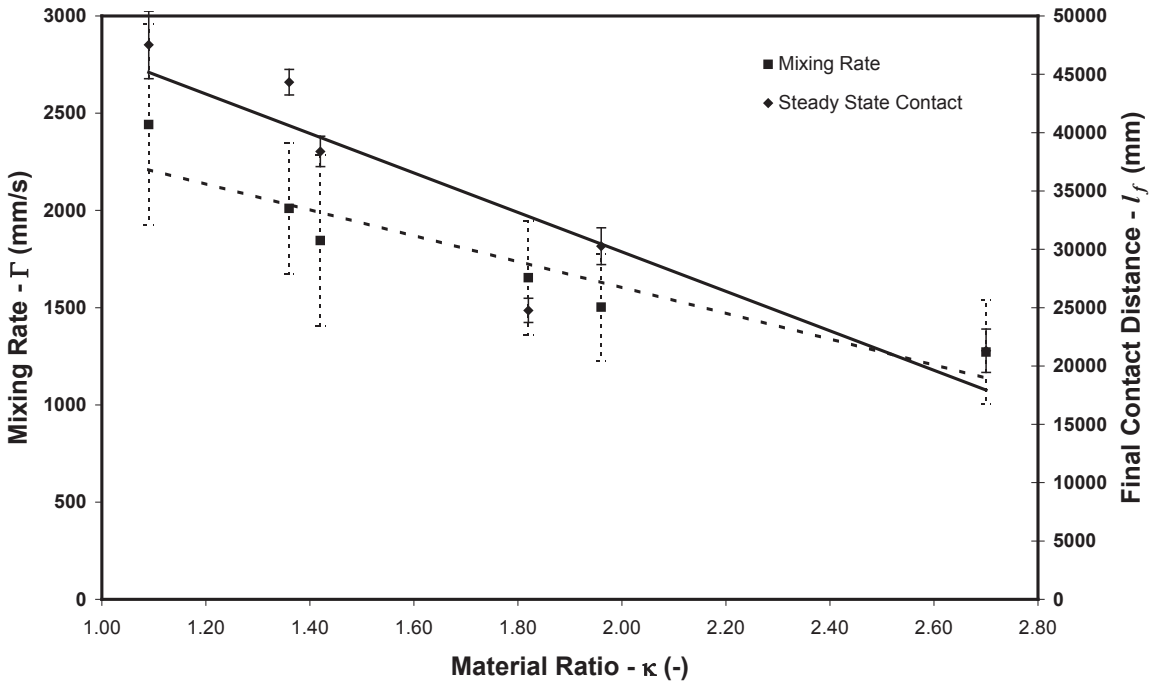

Figure 6.8: Measured mixing rates (Γ) and final contact distances (l_f) with respect to calculated material ratios (κ).

6.4.3 Analysis of the experimental errors

The experimental errors for the final contact distance were used as a measure of the indeterminate experimental error of the experiments. This experimental error included fluctuations in the material count. These fluctuations arose due to the seal between the two panes of glass or the clamps holding the glass face to the drum, both of which caused some material and thus contact distance to be hidden at certain times during the experiments.

Incorrect film exposure was another source of experimental error. However, checking the ratios of the colours in each image eliminated this. If the image was not exposed correctly the ratios of the black to orange pixels would differ significantly

compared to other images from the same experiment. In that case the image was discarded and not used in the image analysis.

The average relative experimental error for the final contact distance for all the experiments was 4%. The average relative experimental error for the mixing rate for all the experiments was 12%. The maximum errors were 10% and 22% for the experimental final contact distances and the experimental mixing rates respectively. The experimental errors described for the final contact distances were also applicable to the mixing rate data. One further aspect of the mixing rate experimental error to be considered was due to the step nature of mixing. This behaviour forced data away from the constant rate line and is illustrated the circled data points of Figure 6.4. This stepwise mixing behaviour caused the experimental mixing rate errors to be larger than the experimental final contact distance errors.

6.5 MODELLING OF THE MIXING IN THE TRANSVERSE DIRECTION OF A ROLLING DRUM

In this section of the thesis, the experimental mixing results are analysed and modelled so that they can be used to predict the mixing rates and the final amount of mixing in a rolling drum as a quantitative measure. Suitable scaling criteria need to be included in the model so that it can be used to predict the mixing in different sized drums.

6.5.1 Mixing rate modelling

The experimental results showed that the mixing rate was linearly dependent on the drum's rotational velocity, the loading of the drum, the mean particle size and the material ratio. Thus the mixing rate can be expressed as:

$$\Gamma = f_1(N, L, d_p, \kappa) \qquad (6.2)$$

However to develop a mixing rate model which can be applied to any drum the scaling factors need to be included in this mixing rate model. The results from Chapter 5 and the stepwise behaviour of the mixing rate show that the mixing occurs in the active layer. Since the rotational velocity and the drum loading affect the solid behaviour in the active layer these parameters will be replaced by active layer properties as part of the model development. The mean active layer velocity is used as one of these parameters as this velocity is a measure of how fast the material is traveling in the active layer, which affects the mixing rate. The size of the active layer is also important and will be the second active layer parameter. Therefore Equation 6.2 can be rewritten as follows:

$$\Gamma = f_2(\overline{V}_{AL}, A_{AL}, d_p, \kappa) \tag{6.3}$$

The particle size and material ratio effects are shown in Figure 6.7 and Figure 6.8 respectively. It was observed that increasing the particle size or the material ratio resulted in a linear decrease in the mixing rate. In the modelling of the mixing rate, it was assumed that the mixing rate could not become negative and this in turn placed restrictions on the particle size and the material ratio that could be used in the model. Thus the overall effect of the particle size with respect to the mixing rate was:

$$\Gamma = f_3(d_{p,MAX} - d_p) \tag{6.4}$$

where $d_{p,MAX}$ is the limiting particle size, beyond which the mixing rate was assumed to be zero.

A similar correlation was derived for the material ratio effect:

$$\Gamma = f_4(\kappa_{MAX} - \kappa) \tag{6.5}$$

where κ_{MAX} is the limiting material ratio, beyond which the mixing rate was assumed to be zero.

Equation 5.6 showed that the mean active layer velocity is a function of the rotational velocity of the drum, and to a lesser extent the loading of the drum. This indicates that the mixing rate should respond to changes in the active layer velocity

similarly as it would respond to changes in the rotational velocity of the drum. Equation 6.6 shows this relationship:

$$\Gamma = f_5(\overline{V}_{AL}) \tag{6.6}$$

Finally, changes in the drum loading resulted in changing the area of the bed. However the mixing only occurred in the active layer and thus the transverse area of the active layer was required, shown in Equation 6.7:

$$\Gamma = f_6(A_{AL}) \tag{6.7}$$

From the experimental results linear relationships were observed in many cases, thus f_3, f_4 and f_5 were linear in nature. However the behaviour of the active layer area was not easily determined as it was dependent on the rotational velocity, the drum loading and the size of the drum. A range of functions were tested and it was found that the mixing rate varied linearly with the square root of the active layer area. An active layer parameter, ϕ, was developed to combine all the parameters that had an effect on the mixing rate and is shown in Equation 6.8:

$$\phi = \overline{V}_{AL}.\sqrt{A_{AL}}.(d_{p,M} - d_p).(\kappa_M - \kappa) \tag{6.8}$$

The active layer parameter was calculated for all experiments and the mixing rate was correlated using this active layer parameter. Figure 6.9 shows that a linear relationship exists between the active layer parameter and the mixing rate. This linear relationship passes through zero, which makes it physically realistic. For example, if the bed was stationary, $\overline{V}_{AL}$ and A_{AL} would both be zero and hence the mixing rate should also be zero. The mixing rate was calculated as follows:

$$\Gamma = 1.503*10^{-3}\ \phi \tag{6.9}$$

The confirmation data points in Figure 6.9 indicate the experimentally measured mixing rates for experiments 25 to 27 and will be discussed below.

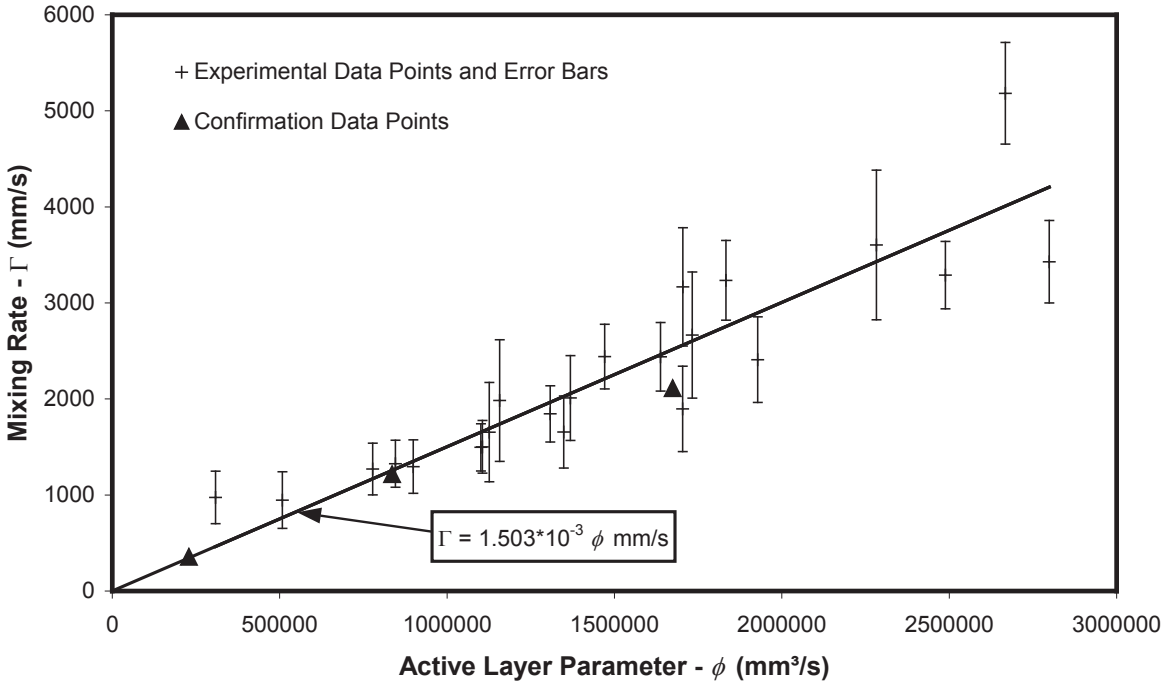

Figure 6.9: Modelling of the mixing rate (Γ) as a function of the active layer parameter (ϕ).

The deviations between the predictions from the mixing rate model and the experimental mixing rate results were calculated as a percentage difference between the predicted mixing rate and the experimental mixing rate. The average deviation was 14% and the maximum deviation was 49%. The largest deviation occurred at the lowest value of the active layer parameter.

6.5.2 Final mixing contact distance modelling

The important parameters for determining the final contact value of solids in a rotating drum were the drum loading, the particle size and the material ratio. It was observed that all these parameters linearly affected the final contact value. Once again, for scaling purposes, the drum loading was replaced by the transverse area of the bed. The rotational velocity did not affect the final mixing contact distance. The final contact distance parameter, λ in mm³, correlation is shown in Equation 6.10:

$$\lambda = A_{BED}.(d_{p,\,MAX} - d_p).(\kappa_{MAX} - \kappa) \qquad (6.10)$$

where A_{BED} is the transverse area of the bed in mm². The final mixing contact distance was plotted against the final contact distance parameter as shown in Figure 6.10. Once again this correlation modelled reality by satisfying the lower limits of the final contact distance parameter, namely passing through the origin. The final contact distance, l_f, was found to be:

$$l_f = 5.280*10^{-2}\ \lambda \qquad (6.11)$$

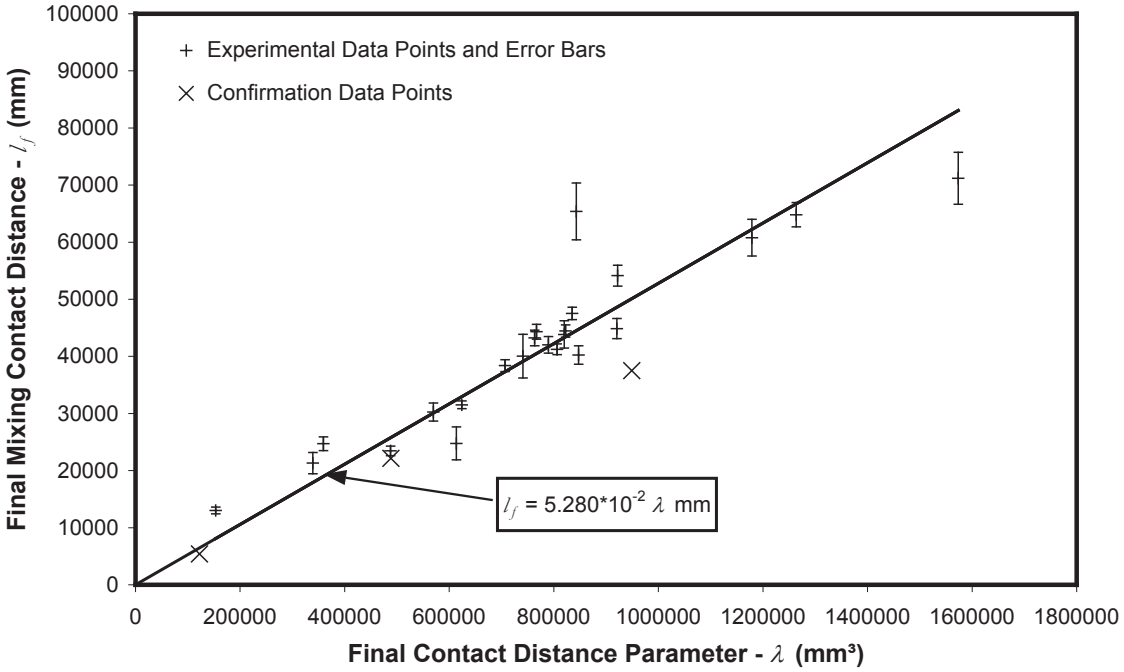

Figure 6.10: Modelling of the final mixing contact distance (l_f) as a function of the final contact distance parameter (λ).

The deviation between the predicted final mixing contact distance of the model and the experimental results was defined as the relative difference between these two values expressed as a percentage. The average and maximum deviations for the final contact distance were 10% and 33% respectively.

6.6 APPLICATION AND VERIFICATION OF THE MIXING MODEL

The mixing model of solids in a rolling bed of a rotating drum consists of two parameters, the determination of the mixing rate and the final contact distance of the bed. In order to use the mixing model, the bed must to be characterised so that the active layer parameter and the final contact distance parameter can be calculated. Thus the active layer percentage as modelled earlier needs to be predicted. From this value the active layer velocity and the active layer area can be calculated. The mean particle size and the material ratio should be known from the experimental setup. Once the active layer parameter is determined, the mixing rate can be calculated. To determine the final contact distance between the two different materials, the final contact distance parameter needs to be calculated. This is done using the bed specifications. By combining the final contact and the mixing rate, the time required to obtain a fully mixed bed can be determined.

Results from Experiments 25 to 27 are shown in Figures 6.9 and 6.10 as the confirmation data points. These experiments were used to test the applicability of the mixing model. Experiment 25 was used to test a different configuration of the bed. The configuration used in experiment 25 conformed to the "smile" configuration as shown in Figure 4.4a with the orange material on the outside of the black material. Experiments 26 and 27 were carried out in smaller drums of 400 mm and 200 mm diameter respectively, and these results were used to validate the scaling capabilities of the model.

The mixing rates of the experiments carried out in the smaller drums were predicted to within 3% of the experimental mixing rates. This was less than the average experimental mixing rate error of 12%. However the determination of the mixing rate of Experiment 25 was 19%. This is still less than the maximum experimental error of the mixing rate experiments. For Experiments 25 to 27, the final contact distance predicted from the model was greater than the experimentally measured

final contact distance. The deviations were larger than the average deviation of the final contact distance model but within the maximum deviation of the final mixing contact distance model.

The successful scaling of the mixing model, using Experiments 26 & 27, was attributed to the use of the active layer proportion correlation of Chapter 5. The model derived here was only tested at the end of a rotational drum but could predict the mixing behaviour in the bulk of a rolling bed if the active layer characteristics in the bulk of the bed are known. Boateng & Barr (1997) noted that the active layer becomes larger away from the end wall indicating a lower velocity. From the active layer parameters this would indicate a slower mixing rate in the bulk of the bed compared to the mixing rate observed at the wall.

6.6 TRANSVERSE MIXING SUMMARY

A new experimental method has been developed to measure the mixing of solids in a rotary kiln using image analysis. Images were taken of the rotating bed and a program was written to analyse these images to determine the contact distance between the different coloured materials.

The experiments carried out tested rotational velocities from 5 to 19 rpm, particle sizes from 0.89 to 5.08 mm, drum loadings from 6 to 40 % by volume and material ratios from 0.55 to 2.70. The mixing rate and the final contact distance were measured from the mixing experiments.

It was observed that the mixing rates for all experiments were linear in nature. Closer observations showed that this linearity was made up from a series of steps. Increases in mixing rates were due to increased rotational velocity and drum loading, while decreases in mixing rate were due to increased particle size and material ratio. The mixing rates were modelled with respect to an active layer parameter, which in turn was a function of the mean active layer velocity, the transverse area of the active layer, the particle size and the material ratio. A linear relationship was found between this active layer parameter and the mixing rate in the drum.

The final contact distance did not vary with rotational speed but increased with increased drum loadings, decreased by increasing the particle size and decreased by increasing the material ratio. The final contact distance was modelled as a function of the final contact distance parameter, which was a function of the transverse bed area, the particle size and the material ratio. A linear relationship was determined for the final contact distance calculation.

The derived models were tested on independent experiments. These independent experiments were carried out for different bed configurations and different drum sizes. Accurate predictions were made of the experimental mixing rates and final contact distances using the models derived in this chapter. These models allow a quantitative measure of the mixing behaviour in a rotating drum to be predicted.

CHAPTER 7

Segregation in the transverse direction of a rotating drum.

Segregation of solids occurs when solid particles of varying sizes and/or densities are mixed. The size and/or density differences result in the heavier and/or smaller particles being concentrated toward the centre of the solid bed in a rolling drum to form a segregated core. Figure 7.1 shows a rolling bed illustrating the position of the segregated core. Segregation has important energy efficiency implications in the operation of industrial rotating kilns (Barr et al, 1989a, b) by hindering heat transfer from the flame in the gaseous phase to the segregated core.

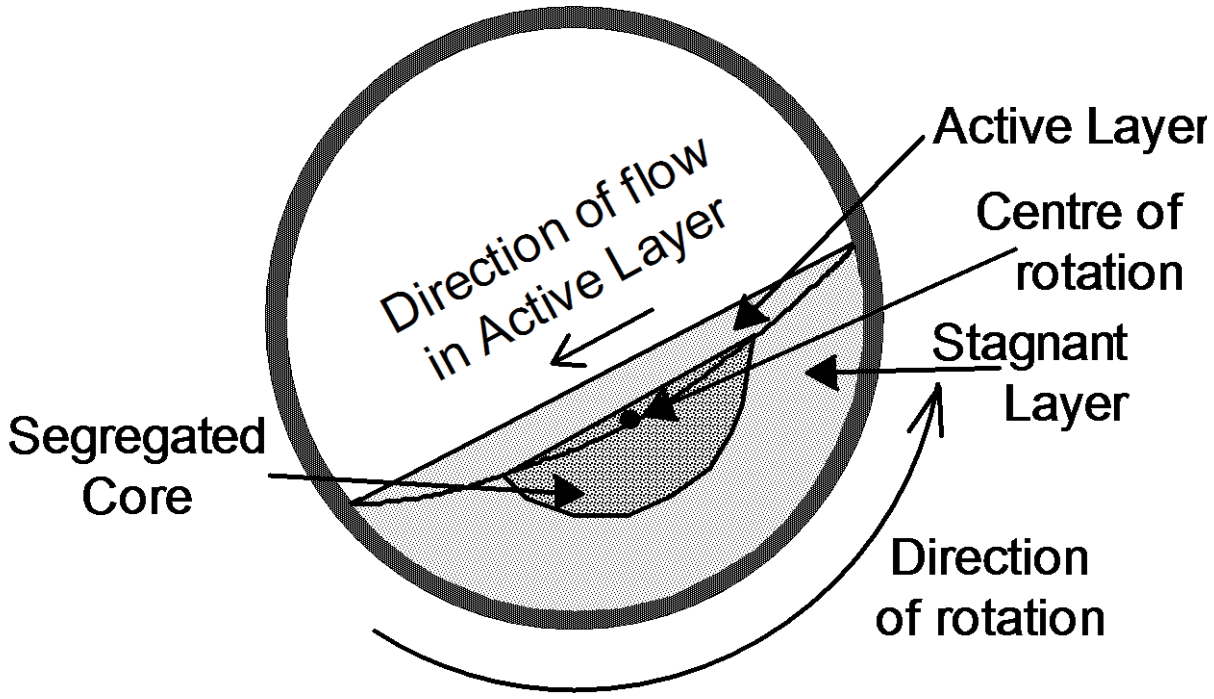

Figure 7.1: Rolling bed showing segregated core and the centre of rotation.

In this chapter a model is developed to predict transverse segregation of granular material in a rolling drum. Previous work (Pollard & Henein, 1989) has shown that the particle size ratio and the rotational velocity strongly affect the segregation behaviour of solid flows. In this work, the effects of the particle size ratio and the mean active layer velocity are studied. The mean active layer velocity was used as this

would represent the velocity of the material in the active layer, where the segregation occurs. Experiments were carried out to measure the effect of these parameters on the segregation dynamics and the final extent of transverse segregation. These experimental results were used to derive a predictive model of transverse segregation.

7.1 TRANSVERSE SEGREGATION EXPERIMENTS

Coloured shale with mean particle sizes as shown in Table 7.1 was used in the experiments. The bulk densities of the different sized coloured material were given in Table 4.3 and it was found that these were not significantly different. Thus segregation due to density differences, as shown by Ristow (1994) would not occur.

The particle size ratios tested ranged from 5.71, for the 5.08 and 0.89 mm material, to 1.37, for the 3.44 and 2.51 mm material. Material less than 0.60 mm diameter was not used in this work due to the inability to colour such small particles. However, it was assumed that due to their electrostatic properties, the smallest particle size would adhere to the surface of the larger particles and thus not take part in segregation. This assumption was made based on the observations of Bridgewater (1976).

Rotational velocities were varied in the experiments from 3 to 23 rpm. The lowest velocity coincided with the start of the rolling regime whereas the highest velocity occurred at the maximum rotational speed of the experimental drum. The transverse segregation experiments and results are presented in Table 7.1.

Images of the bed were taken to measure both the segregation dynamics and the final segregated configuration. The initial configuration of the bed for the segregation dynamics experiments was a well mixed bed. After the bed was loaded, with well mixed material, and the glass panel replaced, rotation was started and images of the drum were taken from the initially well mixed condition until the final segregated state. For the segregation dynamics experiments, images were taken every second for 60 seconds whilst the bed was in motion. For the final segregated state

Experiment Number	Particle Size Ratio	Drum Rotational Velocity N	Segregation Time	Final Inner Layer Concentration Proportion	Final Outer Layer Concentration Proportion
UNITS	**mm/mm**	**rpm**	**s**	-	-
28a	1.37	2.91	2.0	1.21	0.92
28b	1.37	5.73	3.5	1.25	0.91
28c	1.37	8.47	2.5	1.18	0.93
28d	1.37	12.51	-	1.16	0.94
28e	1.37	17.51	-	1.12	0.96
28f	1.37	23.23	-	1.08	0.97
29a	1.48	2.90	3.0	1.01	1.00
29b	1.48	4.76	-	1.09	0.97
29c	1.48	6.70	-	1.09	0.97
29d	1.48	8.47	-	1.10	0.96
29e	1.48	10.56	-	1.10	0.97
29f	1.48	12.51	-	1.09	0.97
29g	1.48	14.94	-	1.08	0.97
29h	1.48	17.51	-	1.07	0.97
29i	1.48	20.34	-	1.06	0.98
29j	1.48	23.23	-	1.05	0.98
30a	1.91	2.90	5.0	1.49	0.82
30b	1.91	5.72	2.5	1.36	0.87
30c	1.91	8.46	3.5	1.29	0.89
30d	1.91	12.50	-	1.25	0.91
30e	1.91	17.49	-	1.20	0.93
30f	1.91	23.21	-	1.12	0.96
31a	2.02	3.89	5.0	1.48	0.82
31b	2.02	6.73	1.5	1.34	0.87
31c	2.02	9.64	-	1.29	0.89
31d	2.02	13.64	-	1.22	0.92
31e	2.02	21.71	-	1.13	0.95
32a	2.82	2.90	8.0	1.84	0.69
32b	2.82	5.72	6.0	1.45	0.83
32c	2.82	8.46	3.5	1.45	0.83
32d	2.82	12.49	-	1.36	0.86
32e	2.82	17.49	-	1.24	0.91
32f	2.82	23.21	-	1.13	0.96
33a	2.99	2.87	-	1.91	0.67
33b	2.99	6.67	-	1.71	0.74
33c	2.99	10.51	-	1.52	0.81
33d	2.99	14.87	-	1.40	0.86
33e	2.99	20.27	-	1.25	0.91
34a	5.71	2.48	-	1.94	0.66
34b	5.71	5.62	-	1.73	0.74
34c	5.71	8.38	-	1.60	0.78
34d	5.71	11.22	-	1.56	0.80
34e	5.71	15.81	-	1.36	0.87
34f	5.71	21.30	-	1.22	0.92
			Average Error	**2.5%**	**1.5%**
			Minimum Error	**0.7%**	**0.3%**
			Maximum Error	**5.3%**	**4.8%**
35[1]	3.87	10.55	-	1.67	0.75
36a[1]	2.02	2.99	-	1.80	0.72
36b[1]	2.02	13.77	-	1.32	0.89

NOTES:

1) These experiments were carried out to test the model based on experiments 28 through 34.

Table 7.1: Segregation experiments and results.

experiments, 20 images were taken after the bed had been rotating for a minute and had attained its final segregated configuration. These images were taken whilst the bed was in motion. After development, the images were analysed to determine the amount of segregation of each image, as explained below. All experiments were carried out in the rolling regime, as this is the desired motion regime of an industrial rotating kiln.

7.2 EXPERIMENTAL ANALYSIS METHODOLOGY

Segregation of the fine material occurred such that the fine material moved towards the rotational centre of the bed. In order to measure the segregation, the segregation analysis software measured the concentrations of the different coloured particles at various distances from this rotational centre. This methodology is outlined in this section of the thesis.

Before the materials could be allocated to different zones of the bed, the geometry of the rolling bed needed to be recorded. This was achieved by defining the edges of the rolling bed. A typical image representing the development of the bed regime for each experiment was manually selected. The centre of rotation of the selection was determined after specifying the locations of Apex A and Apex B of the image, as shown in Figure 7.2, using the equations derived in Chapter 5. From this centre of rotation an array was constructed which contained data of both the distance from the centre of rotation to the selection edge and the angle at the centre for all points of the selection. This array, called the bed outline, was sorted, reduced in size to speed up image processing, saved and used in the analysis of the experimental images. The data was selectively reduced to ensure that the loss of information for the bed outline was minimal. Figure 7.2 shows a typical example of the bed outline. Furthermore, Figure 7.2 also shows the division of layers, the inner layer representing 50% of the radius of the bed outline at any angle from the rotational centre.

For each image in an experiment, Apex A and Apex B were manually located. From the specification of these points the centre of rotation of the current image was determined. The distance and the angle for the pixels of the image were calculated and compared with the data in the bed outline array. If the distance of the current

pixel occurred outside the bed outline radius at the calculated angle, the pixel was ignored. It the pixel occurred within the bed outline radius the count of that pixel type, in the layer in which the pixel occurred, increased by 1.

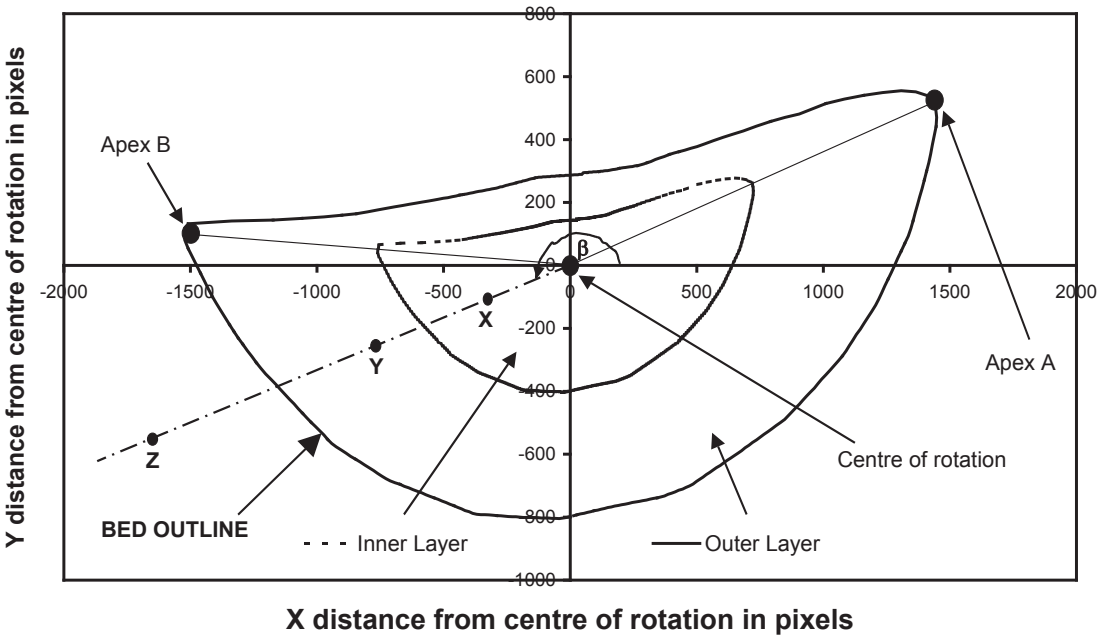

Figure 7.2 – Bed outline used in the segregation analysis.

An example is given to clarify the segregation analysis mechanism. Consider that a typical image was scanned and the current pixel being analysed corresponds to point Z in Figure 7.2. This occurred at angle β. The distance from the centre of rotation of the bed to Z was compared to the radius of the bed outline at that angle, β. The distance to Z was greater than the outline radius and hence point Z was not included in the count of valid data points. When point Y, which was assumed to be orange, was encountered, it was found that this point occurred within the outline. In fact it occurred in the outer layer and thus the orange count of the outer layer was increased by 1. Point X was dealt with similarly but increased the count of its colour type in the inner layer.

By applying the image analysis method to the whole image, the total count of orange and black pixels in each layer was measured. A concentration proportion, defined as the ratio of the concentration of the segregating material in each layer to the mean concentration of the segregated material in the bed, was used to express the

distribution of the segregating material. For the j[th] layer, the concentration proportion, P_j, was defined as:

$$P_j = \frac{O_j/(O_j + B_j)}{O_t/(O_t + B_t)} \tag{7.1}$$

where O_j was the count of orange pixels – representative of the smaller particles - in the j[th] layer, B_j was the count of black pixels – representative of the larger particles - in the j[th] layer, O_t was the total count of orange pixels in the bed and B_t was the total count of black pixels in the bed.

Comparing this data for different images at different times allowed the segregation dynamics to be determined. It should be noted here that numerous layers could be used in the image analysis method to obtain a more defined distribution of fine particles in the bed. However when using more than 2 layers the computational time increased significantly and the accuracy decreased, especially for the inner layers, due to the smaller sample size of the inner layer.

7.3 EXPERIMENTAL SEGREGATION RESULTS

The segregation results consisted of both the dynamics of segregation, taken as the time for the bed to reach its final segregated composition from an initially well mixed bed and the final segregated composition of the bed.

The segregation occurred too fast to be measured and hence the segregation dynamics were only observed in a few experiments. Due to this, no correlation between segregation time, particle size ratio and rotational velocity could be derived. The segregation times, when they could be measured, were taken as the time required to reach the fully segregated bed from the initially well mixed bed and are shown in Table 7.2. Figure 7.3 illustrates typical segregation results when the segregation time could be measured.

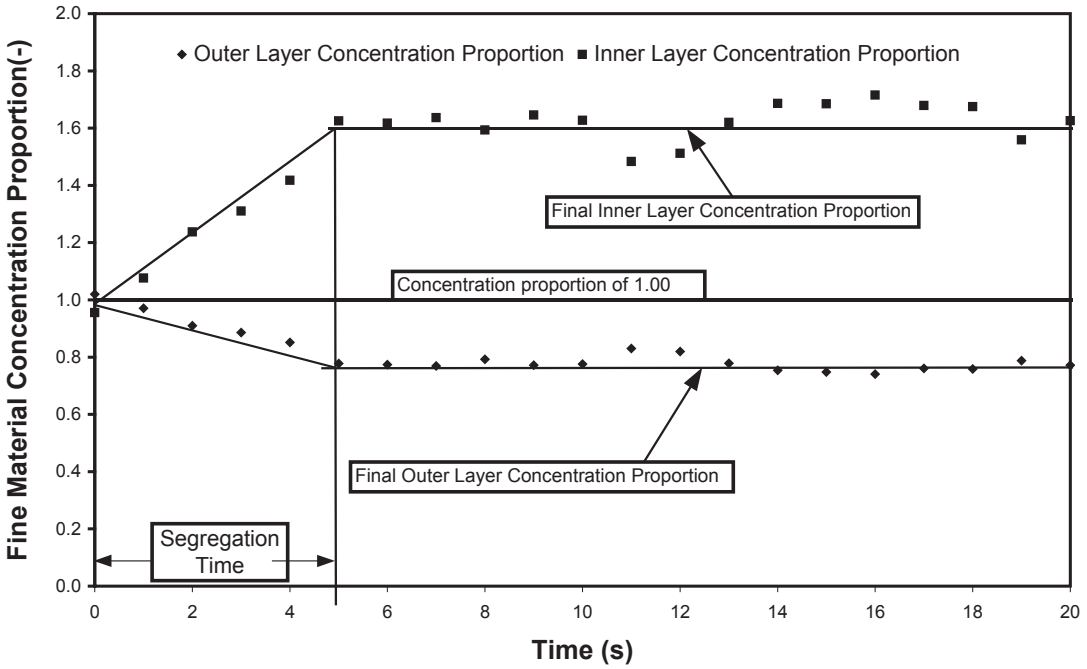

Figure 7.3: Results from a typical segregation experiment.

The final segregated concentration proportion was calculated as the average of the concentration proportions in each layer for the 20 images taken of the fully segregated bed. This corresponds to the average of the fine material concentration proportion after the initial segregation time as shown in Figure 7.3. The fine material was found to move towards the center of the bed for all experiments but this tendency was reduced with the use of smaller particle size differences and higher active layer velocities.

The experimental final concentration proportion is shown in Table 7.1 for both the inner and outer layers of the bed. For all experiments it was observed that the final extent of segregation decreased as the rotational velocity increased. Typical bed configurations for experiment 32 with the different rotational velocities are shown in Figure 7.4. Figure 7.4 A corresponds to the final bed configuration of experiment 32a.

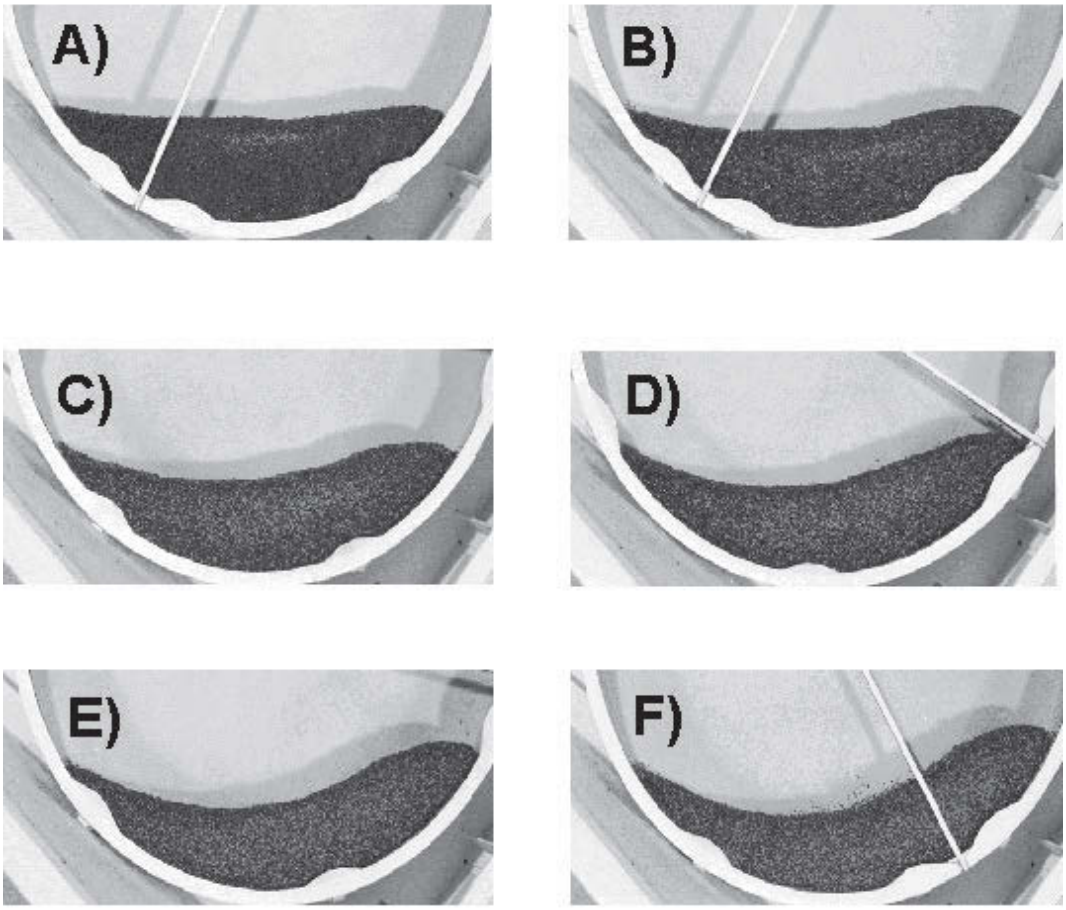

a) 2.90 rpm, b) 5.72 rpm, c) 8.46 rpm, d) 12.49 rpm, e) 14.87 rpm and f) 23.21 rpm
Fig 7.4: Sample final segregation beds for experiment 32.

7.4 ANALYSIS OF THE SEGREGATION RESULTS

The active layer was described in Chapter 5. Using the active layer parameters allows the experimental results to be easily compared and applied to different rotating kilns as shown with the mixing modelling of Chapter 6. Hence the segregation modelling will also be based on the active layer properties. The active layer proportion and active layer velocity are calculated for the segregation experiments and shown in Table 7.2.

7.4.1 Segregation dynamics

Experiment 31a used a particle size ratio of 1.91, a rotational velocity of 2.90 rpm and a drum loading of 15%. This corresponded to an active layer velocity of 0.36 m/s. The segregation time for experiment 31a, as shown in Table 7.1, was 5.00 seconds. For the experimental conditions of experiment 31a, the bed of particles rotated approximately once every 5 seconds, which corresponded to the measured segregation time. However, it must be noted that the experiments were started with an initial stationary bed and that it took a few seconds for the rolling regime to become fully developed in the bed. Thus the bed was fully segregated within one bed revolution. This behaviour was observed for all segregation experiments and indicated that segregation was completed as the granular material passed through the active layer.

At higher rotational velocities the segregation times were not measured since the segregation occurred too fast to be observed. The faster segregation rates found in this work when compared to other work in the literature can be explained by noting the observations of Pollard & Henein (1989) who found that the segregation rate was significantly faster in a 400 mm diameter drum than in a 200 mm diameter drum. The mean active layer velocity in Pollard & Henein's (1989) 200 mm drum was 0.247 m/s whereas it was 0.266 m/s in their 400 mm drum. A drum of 570 mm diameter was used in the current work and the mean active layer velocities were greater than 0.34 m/s in all experiments. Thus the segregation times decreased as the active layer velocity increased. This result can be extended to industrial drums by assuming that the segregation dynamics are completed within a single bed revolution at higher active layer velocities such as those experienced in large industrial rotating drums. Furthermore, as will be shown below, the use of the higher active layer velocities reduced the amount of segregation due to the higher mixing rates as observed in Chapter 6.

Experiment Number	Active Layer Proportion %AL	Active Layer Velocity	Predicted Inner Layer Concentration Proportion	Predicted Outer Layer Concentration Proportion
UNITS	-	m/s	-	-
28a	20	0.34	1.17	0.94
28b	27	0.47	1.15	0.95
28c	31	0.57	1.13	0.96
28d	34	0.71	1.11	0.97
28e	38	0.86	1.09	0.98
28f	41	1.02	1.07	0.99
29a	20	0.35	1.21	0.93
29b	25	0.43	1.19	0.94
29c	28	0.51	1.18	0.94
29d	30	0.58	1.16	0.95
29e	33	0.65	1.15	0.96
29f	34	0.72	1.14	0.96
29g	36	0.79	1.12	0.97
29h	38	0.87	1.11	0.97
29i	39	0.95	1.09	0.98
29j	40	1.02	1.07	0.99
30a	20	0.36	1.39	0.86
30b	26	0.48	1.33	0.88
30c	30	0.59	1.29	0.90
30d	34	0.73	1.23	0.92
30e	37	0.88	1.16	0.95
30f	40	1.04	1.09	0.98
31a	19	0.48	1.37	0.87
31b	25	0.61	1.31	0.89
31c	28	0.73	1.25	0.91
31d	32	0.88	1.17	0.94
31e	36	1.14	1.04	0.99
32a	20	0.35	1.77	0.71
32b	26	0.47	1.66	0.76
32c	30	0.58	1.56	0.79
32d	34	0.72	1.42	0.84
32e	37	0.87	1.28	0.89
32f	40	1.03	1.13	0.95
33a	20	0.34	1.86	0.68
33b	28	0.50	1.69	0.74
33c	33	0.64	1.55	0.79
33d	36	0.78	1.41	0.85
33e	39	0.93	1.25	0.90
34a	14	0.46	1.83	0.70
34b	22	0.59	1.68	0.75
34c	26	0.71	1.56	0.80
34d	29	0.83	1.44	0.84
34e	32	1.00	1.27	0.90
34f	35	1.18	1.08	0.97
		Average Deviation	**4.6%**	**2.6%**
		Minimum Deviation	**0.2%**	**0.0%**
		Maximum Deviation	**19.4%**	**9.1%**
35[1]	33	0.65	1.63	0.77
36a[1]	17	0.43	1.40	0.86
36b[1]	32	0.86	1.18	0.94

NOTES:

1) These experiments were carried out to test the model based on experiments 28 through 34.

Table 7.2: Calculated segregation parameters used in the segregation modelling.

7.4.2 The final segregated bed

A typical experimental plot of the final segregated concentration proportion for experiments 30a to 30f is shown in Figure 7.5. The error bars shown on Figure 7.5 represent the experimental error from the average value. For larger particle size ratios, the bed had a higher concentration proportion of the fine material in the inner layer and a lower concentration proportion in the outer layer.

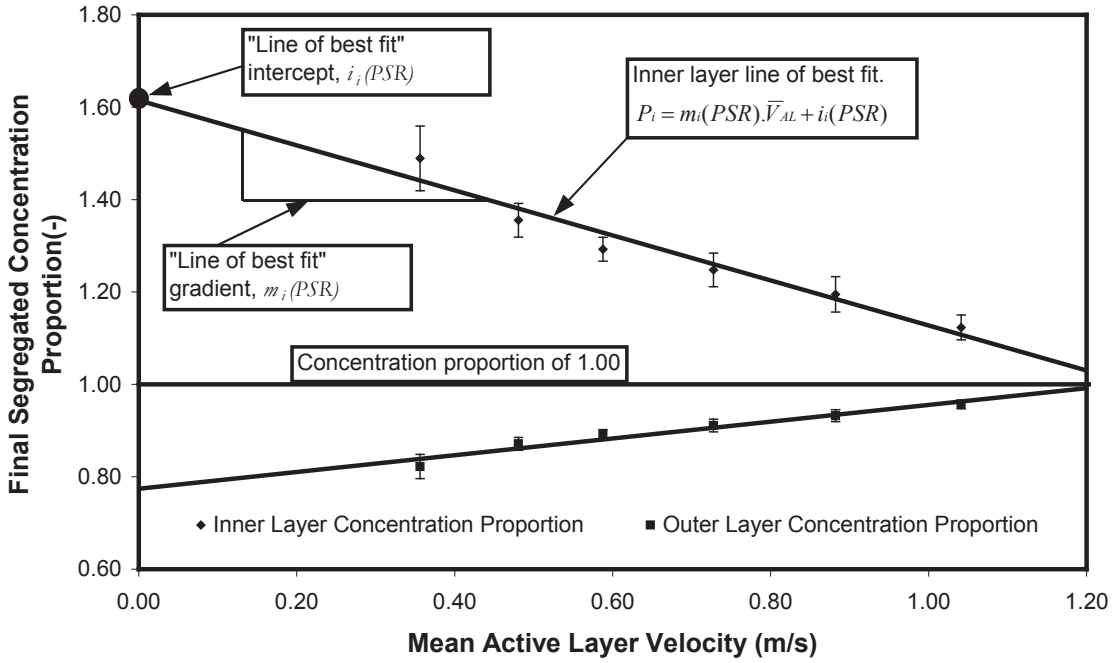

Figure 7.5:Concentration proportion for the inner and outer layer for experiments 30a to 30f.

The average experimental errors for the final inner and outer layer concentration proportion for all experiments were 2.5 and 1.5 % respectively and the maximum errors were 5.3 and 4.8 % respectively. It should be noted that the errors in the inner layer were larger than the errors in the outer layer since the inner layer consisted of a significantly smaller sample size and thus any fluctuations became more prominent.

7.5 MODELLING OF THE SEGREGATION IN THE TRANSVERSE DIRECTION OF A ROLLING DRUM

The results from Table 7.1 show that decreasing the particle size ratio reduced the extent of segregation. This was expected since the ease by which smaller particles percolated through the voids was dependent on the size of the voids. Williams & Khan (1973) found that the size of these voids was dependent on the size of the larger particles. Figure 7.5 shows a linear relation between the active layer velocity and the final segregated concentration proportion for experiments 30a to 30f. The linear relation has the form:

$$P_j = m_j.\overline{V}_{AL} + i_j \qquad (7.2)$$

where $\overline{V}_{AL}$ was the mean active layer velocity, m_j and i_j were the gradient and intercept for the "line of best fit".

Analysis of the other particle size ratios produced graphs similar to Figure 7.5 but with different gradients and intercepts for the line of best fit. It was noted that the "lines of best fit" became steeper with larger particle size ratios, which indicated that m_j and i_j were only functions of particle size ratio and Equation 7.2 can be rewritten as:

$$P_j = m_j(PSR).\overline{V}_{AL} + i_j(PSR) \qquad (7.3)$$

where $m_j(PSR)$ and $i_j(PSR)$ were the gradient and intercept functions for the different particle size ratios respectively.

The model developed predicted the gradient and the intercept functions of the concentration proportion for each set of particle size ratios. Figure 7.6 shows the different values of the gradient and the intercept of the "lines of best fit" for each particle size ratio range for the inner layer. To ensure that the model was physically realistic with respect to the known and experimental boundary conditions, i.e. for a particle size ratio of 1, no segregation occurs in the bed, the gradient correlation was forced through 0 and the intercept correlation was forced through 1 at this particle size ratio. Limiting values of the gradient and intercept were observed at higher particle size ratios and are shown in Figure 7.6 as the final gradient and the final

intercept respectively. These were obtained by averaging the final values of the gradient and intercept of the "lines of best fit" for the larger particle size ratio experiments. The values of the gradient and intercept needed to be determined so that the concentration proportion could be determined using Equation 7.3.

As can be seen from Figure 7.6, there was a small range of particle size ratio, close to 1, where no segregation was observed and thus the values of $m_j(PSR)$ and $i_j(PSR)$ were equal to the values at the boundary conditions. A final limit was also observed for the larger particle size ratios, such as those greater than 2.92. The region in between these limits was linear and can be easily correlated.

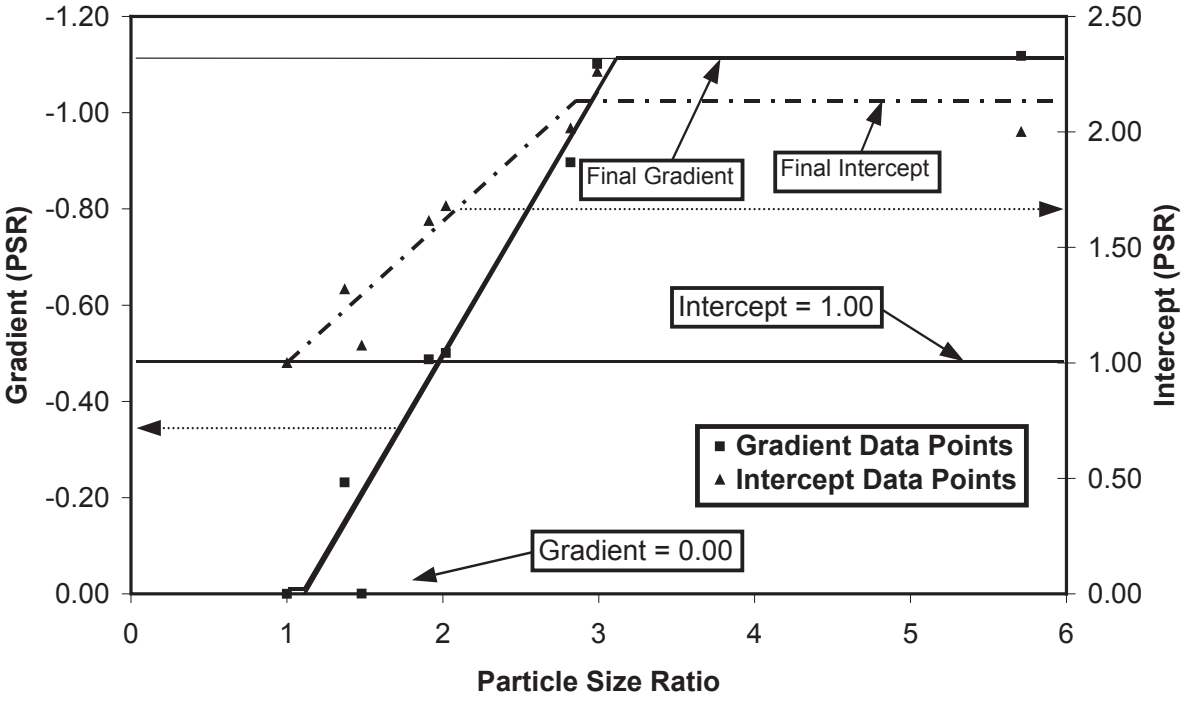

Figure 7.6: Modelling of m(PSR) and i(PSR) for the inner layer.

The prediction of $m_j(PSR)$ and $i_j(PSR)$ needed to be within the ranges of the boundary conditions and the final points for the model to be useful. Table 7.3 illustrates how the values of the gradients and intercepts were calculated for each layer. The data from Table 7.2 were used to calculate the accuracy of the model by predicting the concentration proportion for each of the experiments used in the model derivation. The deviation, expressed as an absolute percentage between the experimental concentration proportion and the value predicted form the model, was

calculated for each experimental data point. The average deviation for the inner layer prediction was 4.6% and for the outer layer this average deviation was 2.6%. These deviations are 1-2 % higher than the average experimental errors but are within the maximum experimental error range, which was 5.3 % for the inner layer and 4.8% for the outer layer. For the 44 experiments carried out, 13 model predictions for the inner layer and 6 model predictions for the outer layer had an error deviation larger than the maximum experimental errors. These larger errors occurred at the extremities of the data sets, such as at the lowest and highest velocities. This is due to the limited overlap of experimental data that are normally associated with the extremities of data sets.

	Lower Limit	PSR Dependent Range	Upper Limit
Inner Layer			
m(PSR)	-1.03	-0.56 * PSR + 0.62	0.00
i(PSR)	1.00	0.61 * PSR + 0.37	2.29
Outer Layer			
m(PSR)	0.00	0.19 * (PSR - 1)	0.38
i(PSR)	0.53	-0.23 * PSR + 1.23	1.00

Table 7.3: Parameters used in the segregation model.

7.6 APPLICATION AND VERIFICATION OF THE SEGREGATION MODEL

Experiments 35, 36a and 36b were carried out but not included in the data set used for the modelling of the segregation. These experiments were used as independent experiments to test the predictive capability of the developed segregation model. The experimental conditions, experimental results and predicted modelling results are shown in Tables 7.1 and 7.2 respectively.

The deviation between the model prediction and the experimental results were calculated and are shown in Table 7.4. For Experiment 35 the model deviations for both the inner and outer layer were less than the average deviation of the segregation model. For experiment 36a the deviation for the inner layer prediction was 22.2%

and for the outer layer this deviation was 19.4%. These deviations were larger than the maximum deviations of the segregation model. However the prediction for Experiment 36b for the inner layer had a deviation of 10.6% and 5.6% for the outer layer, which was well within the maximum deviation of the model. These results do indicate that the segregation model could be used to accurately predict the segregation in a rolling bed.

Experiment Number	Inner Layer Deviation %	Outer Layer Deviation %
35	2.4	2.7
36a	22.2	19.4
36b	10.6	5.6
Average Model	4.6	2.6
Maximum Model	19.4	9.1

Table 7.4: Summary of the deviations for Experiments 35, 36a and 36b.

After using the current segregation model to determine the concentration proportion of each of the layers the actual amount of fine material in each of the two layers can be calculated. The concentration in each layer was simply the predicted concentration proportion multiplied by the overall bed concentration, which should be known from the experiment or plant specifications. The amount in each layer can be calculated by multiplying the concentration of each layer by the volume of that layer, remembering that the inner layer represents 50% of the bed radius from the centre of rotation at any point and the outer layer represents the transverse area of the bed outside of the inner layer. Thus the inner layer represents ¼ of the transverse section bed area and the outer layer represents ¾ of the transverse bed area.

Since the model was expressed in terms of the mean active layer velocity, it was anticipated that the model could be applied accurately to different sized drums since the active layer percentage correlation was measured for different sized drums and found to be independent of the drum size as shown in Chapter 5. Figure 7.5 indicates

that at mean active layer velocities beyond 1.20 ms^{-1} reverse segregation would occur. However, Nityanand et al (1986) showed that reverse segregation only occurred when the bed was operated in the centrifuging regime. Thus, at higher active layer velocities segregation will not take place in a rolling bed.

7.7 CHAPTER SUMMARY

A new method, using image analysis, was developed in this chapter to measure the segregation of solids in the transverse section of a rotating drum, operating in the rolling regime. This new data analysis method was applied to various experiments to study the effect of particle size ratio and mean active layer velocity on both the segregation dynamics and the final segregated configuration.

The segregation dynamics were only observable for a few experiments and therefore could not be modelled. However, by comparing the present work to earlier work showed that segregation occurred faster in larger drums due to the increase of the mean active layer velocity. From these studies it was assumed that the time for the material to fully segregate in an industrial rotating drum would be very short due to the higher active layer velocities experienced in industrial rotating drums.

The derived correlations for the final concentration proportions to determine the concentration proportions were dependent on the active layer velocity and the particle size ratio. Comparison of the experimental results and model predictions showed that the model could be applied accurately. Further to this, the active layer velocity can be predicted for different sized rotating drums using the results of Chapter 5 and thus the segregation model can be applied to predict the segregation behaviour of solids in different sized rotating drums.

CHAPTER 8

Simulation of the mixing and segregation of solids in the transverse section of a rotating drum.

In this chapter the behaviour of the solid mixing and segregation in the transverse section of a rotating drum was simulated. This involved the design of a suitable grid to represent the transverse section of a rolling drum and the translation of the models derived in Chapters 6 & 7 to suit this grid. The simulation was tested against experimental data.

As described in Chapter 3, the transverse section of a rolling bed consisted of an 'active layer' and a 'stagnant layer'. The behaviour of the solids in these layers was different and hence different elements were required to simulation of these layers.

8.1 "STREAM" DEFINITION

The simulation used an approach between classical lumped parameter modelling and discrete elemental analysis modelling. A "stream" was defined as an entity that consisted of flow rates for a range of materials, each of which could be at a different temperature. The amount of mixing between the materials was also included in a "stream". The best way to illustrate the "stream" was to include the C++ computer code of a "stream" as shown in Figure 8.1.

The "stream" variable consisted of an array of ASH and SHALE material variables. ASH and SHALE were used in the "stream" definition to represent the two different materials present in the retort zone of the AOSTRA-Taciuk Processor. These arrays represented the different material sizes, their flow rates and their temperatures. For example, ASH[0] corresponded to the smallest ash size. Since the material size was

used in the definition, the material size was not required in the "stream" structure. The flow of the material, FLOW, and the temperature, TEMP, in each "stream" could be specified. FLOW was measured in m^2/sec and TEMP was measured in K. TEMP is used in the granular heat transfer and will be described in Chapter 9.

```
struct Material
{
        double  FLOW;
        double  TEMP;
};


class Stream
{
        public:
                double     ExtentOfMixing;
                // ASH and SHALE streams of the following particle ranges
                // -0.60, +0.60-1.40, +1.40-2.00, +2.00-3.02, +3.02-3.86, +3.86-6.30
                // ASH[ 0] refers to 0-0.60 mm, ASH[ 1] refers to 0.60-1.40 mm etc
                Material    ASH[ 7];
                Material    SHALE[ 7];
};
```

Figure 8.1: C++ computer code for the definition of the "stream" structure.

These "streams" were used in the 'stagnant layer' and the 'active layer' control volumes as described below.

8.2 'STAGNANT LAYER' CONTROL VOLUMES

The 'stagnant layer' control volume represented an element of residence time only since no mixing or segregation occurred within the 'stagnant layer', as shown in the experiments and the literature review. However, heat transfer between the two materials and the volatile evolution from the shale occurred in the 'stagnant layer' and this will be considered in Chapter 9.

Figure 8.2 shows a schematic of the 'stagnant layer' control volume. The size of the control volume was dependent on the geometry of the drum and only two "streams" occurred within the 'stagnant layer' control volume. These "streams" were the Stagnant Layer Feed and the Stagnant Layer Product. In the current simulation, the Stagnant Layer Product equalled the Stagnant Layer Feed but with a time delay. This time delay and the geometry of the control volumes will be described in Section 8.5. The temperatures of the "streams" will differ in Chapter 9 due to the inclusion of the heat transfer mechanism and the volatile evolution of the shale. The volatile evolution of Figure 8.2 is not defined as a "stream". The volatile evolution represents the volatiles evolved from that control volume as calculated using the imbedded heat transfer and volatile evolution models of Chapter 9.

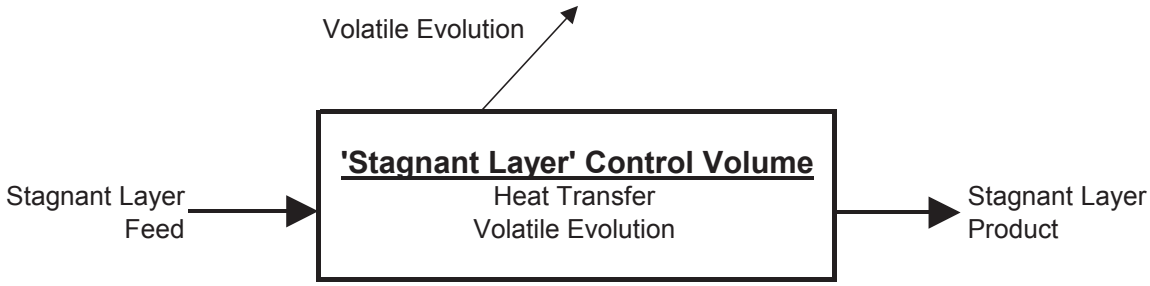

Figure 8.2: Schematic of a 'stagnant layer' control volume.

The 'stagnant layer' control volume was also defined as a "stream". Each 'stagnant layer' control volume contained functions to determine the important parameters of the control volume. These functions allowed the mean particle sizes, the mean temperatures and the total flows of the materials to be calculated.

8.3 'ACTIVE LAYER' CONTROL VOLUMES

An 'active layer' control volume represented a small part of the 'active layer'. It was shown in Chapters 6 and 7 that the 'active layer' was responsible for the mixing and segregation in the bed. Thus procedures were required to allow these mechanisms to occur in the 'active layer' control volumes.

The 'active layer' control volume had the same basic structure as the 'stagnant layer' control volume but had extra "streams" and included mixing and segregation mechanisms. Figure 8.3 illustrates an 'active layer' control volume.

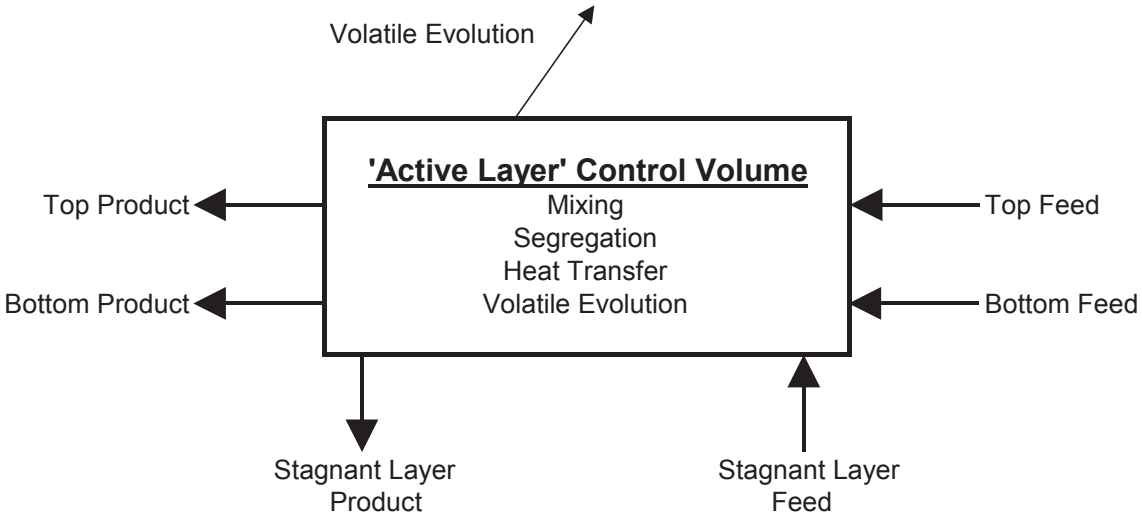

Figure 8.3: Schematic of an 'active layer' control volume.

8.3.1 Streams of the 'active layer' control volume

Each 'active layer' control volume had a maximum of three "streams" as feeds. These could be a "stream" from the 'stagnant layer', a "stream" from either the upper or lower control volume of the previous 'active layer' control volumes. A maximum of three product "streams" also existed for each 'active layer' control volume. There was a possible feed to the stagnant layer or either an upper or lower feed to the next 'active layer' control volumes. The number of "streams" depended on the position of the control volume within the 'active layer'.

8.3.2 Mixing in the 'active layer' control volume

The mixing model derived in Chapter 6 was directly applied to the solids in an 'active layer' control volume. It was assumed that applying the mixing model derived for the

complete 'active layer' to individual 'active layer' control volumes allowed the overall mixing behaviour of the 'active layer' to be determined. This model requires the determination of the 'active layer' parameter, which is dependent upon the mean velocity in the control volume, the transverse area of the control volume, the mean particle size diameter and the ratio of materials in that control volume. Since the mean velocity of the control volume is dependent on the size and position of the control volume, the control volumes needs to be characterised, which will be described in the grid selection section below. The cross sectional area of the 'active layer' control volume was calculated from the geometry of the bed. The mean particle size and the material ratio were calculated for each control volume in each time step to account for the fluctuations in these parameters due to material flow.

The 'active layer' parameter was calculated and then the mixing rate was calculated using Equations 6.8 and 6.9. The mixing rate was multiplied by the sampling time, τ_{SAMP}, to calculate the new amount of mixing in the control volume in that time sample. This new amount of mixing was then added to the previous amount of mixing in that control volume. The final mixing contact, l_f, for the control volume was determined using Equations 6.10 and 6.11, to ensure that mixing in the control volume did not exceed the maximum contact for that control volume. Thus the amount of mixing in a control volume, $l(t)$, at time t was calculated as:

$$l(t) = MINIMUM\left[l_f, l(t-1) + \Gamma(t).\tau_{SAMP}\right] \tag{8.1}$$

The addition or removal of material from an 'active layer' control volume added or removed the respective amount of mixing to or from that control volume. These values were stored in the ExtentOfMixing variable of "stream".

8.3.3 Segregation in the 'active layer' control volume

The segregation model derived in Chapter 7 was applied to the 'active layer' control volumes. It was assumed that the segregation of the 'active layer' as a single entity

could be approximated by applying the segregation model to the individual 'active layer' control volumes. For the segregation mechanism, the Stagnant Layer Product and the Bottom Product of the 'active layer' control volume were considered as a single "stream" and the segregating material favoured this combined "stream". This approach only required the determination of the segregated material proportion in the segregating "stream" and, if segregation occurred, forced material greater than the mean particle size to the Top Product "stream". The movement of material as such was essential to maintain the mass balance in the control volumes. The proportion of the finer material was calculated using Equation 7.3 and Table 7.3 but in the simulation the particle size ratio was taken as the ratio of the mean particle size in the control volume divided by the particle size of the segregating material. Only particle sizes less than the mean particle size were considered in the segregation mechanism.

Segregation was assumed to only be dependent on the particle size differences. The density differences between the ash and the shale were not considered since the experimental work was based solely on size differences. Thus for the segregation mechanism, the ash and the shale of the same size were considered as a single material. After the segregation, this segregated material was re-divided into its ash and shale components.

The segregation model derived in Chapter 7 assumed that a uniform active layer velocity was encountered. From the velocity profile of Nakagawa et al (1992) and as shown in Section 8.4, the velocity in the 'active layer' control volumes were different. The experimental segregation model did illustrate that for a mean velocity, a certain proportion of the finer material would move closer to the rotational centre of the bed. From the 'active layer' control volume velocities, the segregation was determined in the individual 'active layer' control volumes. The mean velocity in each control volume was known from the mixing method and thus the ratio of each material, moving closer to the centre or further away from the centre was calculated, since numerous particle sizes were used in this work, which required numerous segregation correlations to be solved simultaneously.

Thus the proportion of each particle size for each material was calculated. The actual material content into the "stream" depended on the control volume size, the flow of the "streams" and the ratio of the segregating material.

8.4 SELECTION OF A GRID SYSTEM TO REPRESENT A ROLLING BED

The grid of the control volumes used in the simulation, as shown in Figure 8.4, consisted of the previously defined 'stagnant layer' and 'active layer' control volumes. These control volumes were combined to represent the transverse section of a rolling bed.

In order to discuss the grid a few definitions are required. 'Stagnant layer' and 'active layer' control volumes were defined above and are illustrated by the individual polygons of Figure 8.4. An 'active layer' zone consisted of the 'active layer' control volumes between the 'stagnant layer' – 'active layer' interface and the free surface of the bed. These were made up of 2 or 3 individual 'active layer' control volumes representing the different layers within an 'active layer' zone. At the extremities of the 'active layer', the 'active layer' zone only consisted of one 'active layer' control volume. A 'stagnant layer' zone consisted of the 'stagnant layer' control volumes between the edge of the bed and the centre of rotation. 'Stagnant layer' layers were defined as the 'stagnant layer' control volumes between two annuli. These definitions are illustrated in Figure 8.4. By using numerous control volumes it was anticipated that the mixing, segregation, heat transfer and volatile evolution could be simulated accurately, especially in larger kilns. The different layers allowed the segregation of the materials to be predicted. The staggering of the 'active layer' control volumes facilitated the bringing together of the materials and allowed them to mix. This new approach allowed mixing to occur between layers as the materials passed through the 'active layer'.

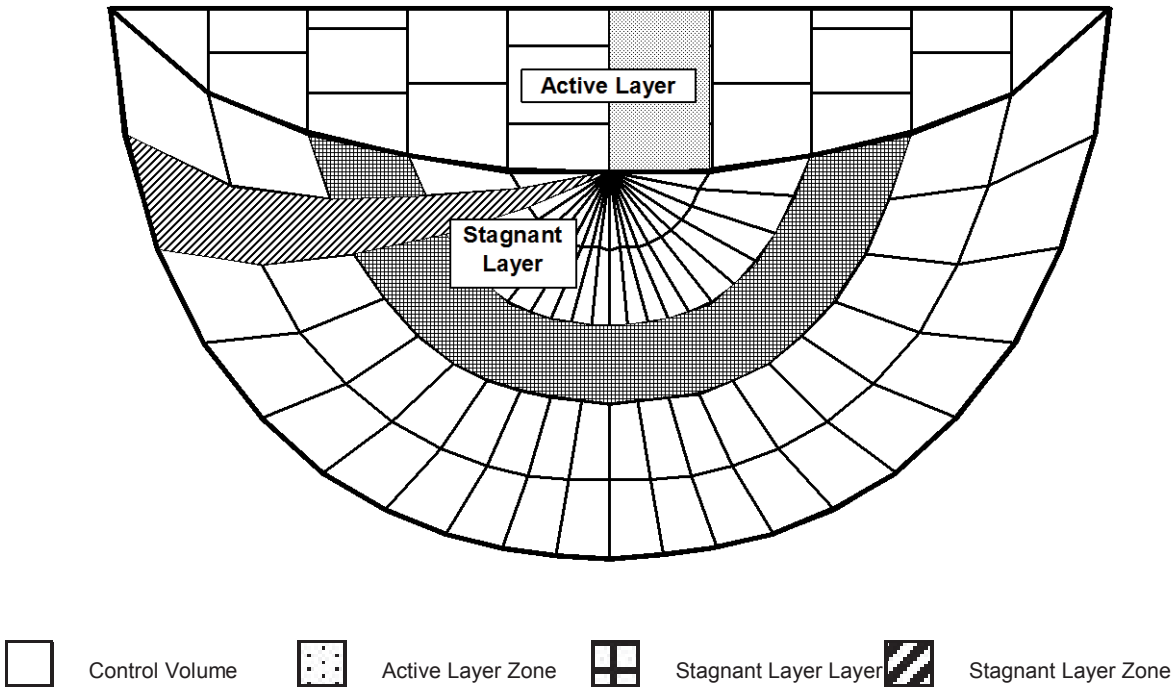

Figure 8.4: Schematic of the control volume grid used in the simulation.

A total of 5 'stagnant layer' layers were used in the simulation and 20 'stagnant layer' zones were used. This indicated that a total of 100 'stagnant layer' control volumes were used to simulate the 'stagnant layer'. The 'active layer' consisted of 10 'active layer' zones and a total of 22 'active layer' control volumes.

The 'stagnant layer' control volumes passed material from one 'stagnant layer' control volume into the next 'stagnant layer' control volume in its layer. At the extremities of the 'stagnant layer' layers the 'stagnant layer' control volumes were fed by or fed the 'active layer' control volumes.

The 'active layer' control volumes were interlaced to facilitate the mixing process. This was done to allow material at different levels in the 'active layer' to mix. Note that the bringing together of these streams did not indicate mixing. Mixing only occurred as a result of the mixing model. However allowing the materials to join in this manner provided the potential required for mixing.

8.5 SPECIFICATION OF THE SIMULATION

The sizes of the control volumes were calculated using the specifications of the rotating drum. From the drum size and drum loading, the transverse bed area was calculated. From the drum loading and the rotational velocity, the 'active layer' proportion was calculated using Equation 5.2. This allowed the total transverse area of the 'active layer' and 'stagnant layer' to be calculated.

8.5.1 'Stagnant layer' control volume characterisation

In the simulation, the 'stagnant layer' was assumed to consist of five individual layers. It was assumed that the angle subtended by each of these layers at the centre of rotation of the bed were equal. The areas of the different layers were calculated as a proportion of the total bed area using a modified annulus area calculation method. The five 'stagnant layer' layers were assumed to be equidistant. The area of the individual 'stagnant layer' control volumes was obtained by dividing the area of the 'stagnant layer' layer by 20 as each layer was made up of 20 control volumes.

The velocities in the control volumes of a 'stagnant layer' layer were equal. These were calculated at the mid chord position as the velocity at mid chord was linear as shown by Nakagawa et al (1992). The rotational velocity of the drum at the drum wall and the zero velocity point at the centre of rotation were used as the boundary conditions and the mean velocities in the different layers were calculated by interpolating between those boundary conditions.

The residence times in the 'stagnant layer' control volumes were determined from the angular velocity of the drum and the angle subtended at the centre of rotation of the 'stagnant layer' control volumes. Since the 'stagnant layer' was well packed, all the residence times of the 'stagnant layer' control volumes were assumed to be equal.

A flux was developed in the 'stagnant layer'. The flux was defined as the transverse area of the 'stagnant layer' control volume divided by the residence time in that control volume. The flux was used as a material balance between different control volumes. All the fluxes of the control volumes in any 'stagnant layer' layer were equal.

8.5.2 'Active layer' control volume characterisation

The areas of the active layer control volumes were determined geometrically by developing an equation of the 'active layer' – 'stagnant layer' interface. This correlation allowed the area of the 'active layer' zones to be determined. The width of each 'active layer' zone was a 10^{th} of the bed chord length. The individual 'active layer' control volume areas were determined by dividing the zone height into two or three sections, depending on the location of the zone. To maintain the material balance, the flux in any 'active layer' zone must equal the flux of the previous 'active layer' zone plus or minus the fluxes from the 'stagnant layer'. This flux balance was used to determine the residence time of the 'active layer' zones. The mean velocity of the 'active layer' zones was then calculated by dividing the width of the control volume by the residence time. Assuming that the velocity profile was linear in each 'active layer' zone, a mean velocity in each 'active layer' control volume was calculated using interpolation based on the height and position of the control volume. From this mean velocity the residence time in that control volume was calculated. The flux for each 'active layer' control volume was calculated from the area of the control volume and the residence time. The total flux of the individual 'active layer' control volumes in an 'active layer' zone equalled the original flux in the 'active layer' zone indicating that the 'active layer' zone was correctly represented by the individual 'active layer' control volumes. The calculation of the 'active layer' control volumes in this manner indicated that the material moved faster in the higher 'active layer' control volumes compared to the lower ones.

8.5.3 Simulation sampling time

The residence time of each control volume was calculated as mentioned above. The residence times were then compared in order to determine a minimum residence time. This was important so that the flow through any control volume would not exceed the flux of any control volume in the sampling time. To facilitate the calculation and reduce the computational requirements it was necessary to move the material from one 'stagnant layer' zone to the next periodically. The sampling time was taken as smallest residence time rounded down to the nearest integral of the 'stagnant layer' residence time as shown below:

$$\tau_{SAMP} = \frac{\tau_{SLCV,\,res}}{\mathrm{int}\left(\dfrac{\tau_{SLCV,\,res}}{\tau_{\min}} + 1\right)} \tag{8.2}$$

where τ_{SAMP} is the calculated sampling time, $\tau_{SLCV,res}$ is the residence time in the 'stagnant layer' control volumes and τ_{min} is the minimum residence time of all the control volumes in the grid. In each sampling time, a respective amount of the control volumes was removed from the 'active layer' control volumes and added to the next 'active layer' control volumes. Then the properties of the control volumes were re-evaluated and the mixing and segregation mechanisms updated. After each $\mathrm{int}\left(\dfrac{\tau_{SLCV,\,res}}{\tau_{\min}} + 1\right)$ timesteps the material in the 'stagnant layer' control volumes was moved from one control volume to the next.

8.5.4 Material balance

In order to verify that the simulation was running correctly, the dynamic material balance was checked in the simulation to ensure that material was not generated or lost due to computational errors. A balance on the flux was carried out to ensure that the movement of materials was representative of the physical system. It was found that fluxes across any control volume at any time balanced and thus the

implementation of the movement of material between control volumes was considered correct.

8.6 MIXING AND SEGREGATION PERFORMANCE OF THE SIMULATION

In order to simulate the behaviour of an industrial rotating kiln, the simulation derived must be validated with experimental data. This section described the comparison of the simulation model results to the experimental results.

8.6.1 Mixing

Two important parameters used to describe the mixing behaviour predicted by the simulation were the final contact distance between the two materials and the time required to reach this final contact distance, referred to as the mixing time. The simulation mixing time was taken as the time required to reach 95% of the final simulation contact distance. The experimental mixing time was the experimental final contact distance divided by the mixing rate. Table 8.1 shows a comparison between experimental and simulation results for a few selected mixing experiments.

	Experimental Final Contact	Simulation Final Contact	Final Contact Deviation	Experimental Mixing Time	Simulation Mixing Time	Mixing Time Deviation
Experiment	m	m	%	s	s	%
3	41	42	2	25	43	72
25	38	51	37	18	45	153
26	22	25	15	18	41	124
27	5	6	16	15	37	144
Average			17			123

Table 8.1: Experimental and simulation mixing results.

Good agreement was observed between the experimental and the simulation final contact distances. The deviations between the experimental and the simulation results for the final contact distances were approximately equal to the deviations

observed by the final contact distance model. This indicated that the simulation accurately predicted the final mixing contact distances as described by the mathematical final contact distance model of Chapter 6.

Significant deviations were observed between the experimentally measured mixing times and those predicted by the simulation. Figure 8.5 shows the experimental and the simulation mixing results for Experiment 3.

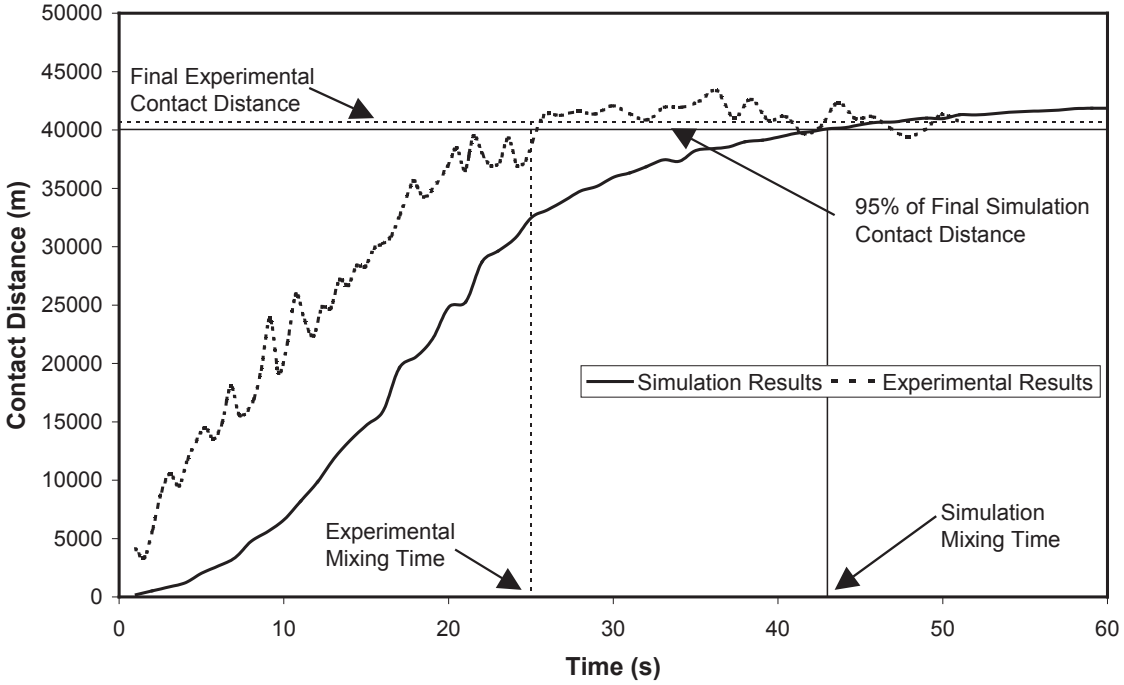

Figure 8.5: Experimental and simulation results for Experiment 3.

The initial mixing rate from the simulation is less than the experimentally measured mixing rate. It takes approximately 5 seconds for the mixing rate of the simulation to increase and then it equals the experimental rate, shown by the parallel regions of the mixing curves. After the mixing of the simulation is approximately 70% completed, the simulation mixing rate decreases and the mixing predicted by the simulation follows exponential decay.

Further tests were carried out on the simulation to determine why this mixing rate deviated significantly. The simulation was used to predict the mixing behaviour of

the velocity experiments of Chapter 6. The simulation results are compared to the experimental results in Table 8.2.

		Experimental		Simulation		
	Active Layer Velocity	Final Contact Distance	Mixing Time	Final Contact Distance	Mixing Time	Mixing Time Deviation
Experiment	mm/s	m	s	m	s	%
5	623	42.0	32	42.2	94	190
6	703	43.8	22	44.4	63	187
3	792	41.2	25	42.1	43	72
7	836	47.5	19	41.2	33	69
8	911	44.5	18	44.9	32	75
9	995	40.3	17	45.0	25	47
10	1045	43.2	13	43.7	19	42
11	1219	44.9	14	51.0	16	19

Table 8.2: Comparison of the speed mixing experiments to the predicted simulation results.

The deviation between the experimental and simulation mixing time was calculated. This deviation decreased as the 'active layer' velocity increased. The simulation was constructed of a series of 'active layer' and 'stagnant layer' control volumes. The velocities in the different 'active layer' control volumes were not constant, as assumed in the mixing models of Chapter 6. The 'active layer' control volumes closest to the stagnant layer had a lower velocity and the higher 'active layer' control volumes had higher velocities compared to the mean 'active layer' velocity. This is illustrated in Figure 8.6 by the grey and black coloured control volumes of the 'active layer' control volumes, respectively. The mixing rate is dependent on the velocity in the control volumes. Due to the grey control volumes of Figure 8.6, the mixing in those control volumes was slower compared to the overall experimental mixing rate. This reduced the overall mixing rates of the whole 'active layer' and resulted in the total predicted mixing time of the simulation being larger than the experimental mixing time.

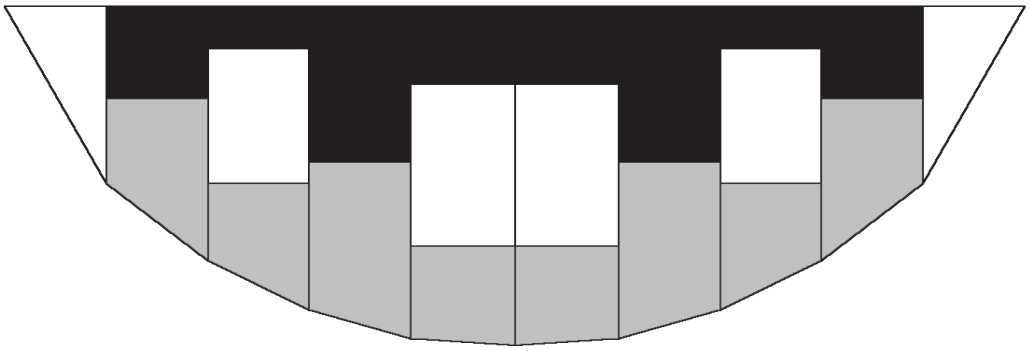

Figure 8.6: 'Active layer' schematic illustrating the different velocity regions.

However, the deviation between the experimentally measured mixing time and the mixing time predicted from the simulation was plotted against the mean 'active layer' velocity as shown in Figure 8.7. An inverse relationship is observed between the deviation and the mean 'active layer' velocity. This relationship was not quantified but illustrated that simulations conducted at higher 'active layer' velocities accurately predicted the experimental behaviour of mixing in a rotating drum.

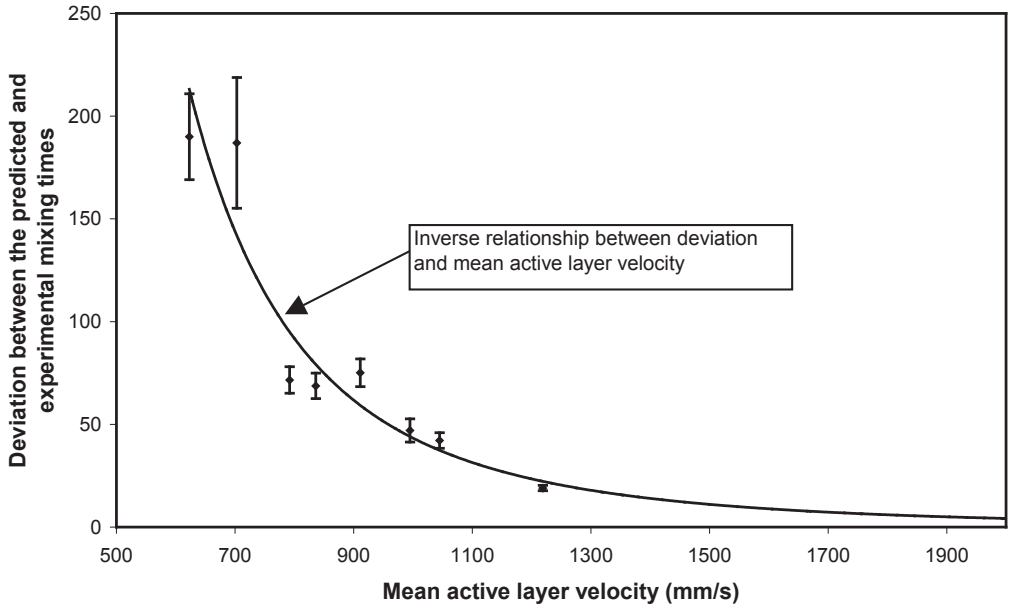

Figure 8.7: Deviation between the predicted and experimental mixing times as a function of the mean 'active layer' velocity.

8.6.2 Segregation

As noted in Chapter 7, the dynamics of segregation could not be determined and were assumed to be very fast in an industrial rotating kiln. In this section of the thesis, the simulation behaviour of segregation was tested. Experiments were conducted using the simulation model to determine the mean particle size in the different layers of the bed, which in turn would reflect the amount of segregation.

The segregation model used only two layers and determined a proportion of material in each layer with respect to the total proportion of that material in the bed. The mean particle size could be calculated by multiplying the ratios of the materials with the particle sizes of those materials and the overall proportion of that material in the bed. The simulation used five layers and these layers were reduced to two for comparison between the simulation and the experimental results. Layers 1, 2 and half of 3 represented the outer layer and layers 4, 5 and the other half of layer 3 represented the inner layer. The experimental and simulation particle sizes are shown in Table 8.3.

	Experimental Mean Diameter		Simulation Mean Diameter		Deviation between Simulation and	
Experiment	Inner Layer	Outer Layer	Inner Layer	Outer Layer	Inner Layer	Outer Layer
	mm	mm	mm	mm	%	%
35	1.7	2.7	1.2	3.1	29.3	17.8
36a	3.2	4.3	2.6	4.1	20.8	5.4
36b	3.6	4.0	2.6	4.2	27.3	3.8
Average					25.8	9.0

Table 8.3: Comparison of the mean particle size in the inner and outer layer for the experimental and simulation segregation results.

The simulation predicted that more of the fine material accumulated in the inner layer compared to the experimental results. This is illustrated by the larger particle size differences in Table 8.3.

Once again the lower mean 'active layer' velocities of the grey control volumes account for this. According to the segregation model of Chapter 7, lower velocities resulted in more material being segregated. The division of the 'active layer' into 22 individual 'active layer' control volumes resulted in the lower velocities, compared to the mean 'active layer' velocity, in the grey control volumes of Figure 8.6. This resulted in a decrease of the mixing rate but also resulted in additional segregation. The segregation behaviour is expected to decrease with increased 'active layer' velocities, such as those encountered in industrial rotating kilns.

8.7 CHAPTER SUMMARY

A grid was developed that was suitable for the simulation of the mixing and segregation of solids in the transverse section of a rotating drum. This grid consisted of two distinct zones, the 'active layer' and 'stagnant layer', each of which had differently functioning control volumes.

The simulation was tested against laboratory experiments and found to agree very well with the prediction of the final amount of contact between two materials. Large deviations were observed between the experimental mixing times and those observed from the simulation. These deviations were inversely proportional to the mean 'active layer' velocity. The simulation could be used to accurately predict the mixing behaviour at higher rotational velocities, such as those encountered in industrial rotating kilns due to their larger drum diameter. Segregation differences were observed between the experimental and segregation results. Once again these deviations were due to the different velocities of the individual control volumes compared to the mean 'active layer' velocities. In larger drums, the velocity of the 'active layer' increases and hence the segregation would decrease.

CHAPTER 9

Simulation of the retort zone of the AOSTRA-Taciuk Processor.

Two aims of this thesis were to derive a granular heat transfer model applicable to the AOSTRA-Taciuk Processor and then to predict the behaviour of the retort zone of the AOSTRA-Taciuk Processor. The simulation derived and confirmed in Chapter 8 will be extended in this chapter to include the granular heat transfer between the two materials and the thermal reactions of the materials in the AOSTRA-Taciuk Processor so that the AOSTRA-Taciuk Processor can be simulated.

9.1 DERIVATION OF THE GRANULAR HEAT TRANSFER MODEL

As shown in Figure 2.8, there are various paths where heat is transferred to or from a particle. These heat transfer mechanisms included conduction, convection and radiation. The model developed here will focus on the heat transfer between the two different materials that will be used in the AOSTRA-Taciuk Processor. The heat transfer to the drum walls or from the gas phase above the bed to the bed of solids will not be included in this model.

9.1.1 Granular heat transfer model assumptions

Due to the use of hard particles with minimum contact, conduction heat transfer between the particles was assumed to be negligible (Molerus, 1997). Conduction into the particle was assumed to be fast thus the heat transfer was limited to convection or radiation to or from the surface of the particles.

Natural convection was assumed to take place from the gases at the mean temperature of the control volumes, which were described in Chapter 8, to the individual particle types and temperatures in the control volumes. This convection can results in heat transfer to or from the particles depending on the temperature difference between the particles and the mean temperature of the control volume. It was assumed that the gas phase, due to its lower heat capacity was at the mean temperature of the solids in a control volume. It was also assumed that only natural convection between the solid and the gas occurred because the velocities in the control volumes were too low for forced convection to occur. The gas properties required for the determination of the Nusselt number, as described below, were evaluated at the mean gas temperature of each control volume.

Radiation was assumed to only take place from the hot material, the ash, to the cold material, the preheated shale. Radiation to the drum and gas phase and vice versa was not considered as this is beyond the scope of this simulation. The gases were assumed to be non participating for the radiation heat transfer calculation. Participating gases, such as H_2O and CO_2, would hinder the radiative heat transfer through the gas phase.

The total heat transfer was assumed to be the addition of the natural convective heat transfer and the radiative heat transfer.

The heat transfer process taking place in the kiln is unsteady heat transfer process, however the heat transfer was assumed to be pseudo steady state so that the heat transfer rate could be determined. This was justified by using small time steps in the simulation and large temperature differences between the different materials compared to the temperature changes of the materials in a time step. After calculating (and balancing) the heat transfer rates, the new temperature of the materials and the amount of volatile evolution occurring within that control volume and time step were determined. These new temperatures were then used to determine the heat transfer rate for the next time step.

9.1.2 Natural convection heat transfer

To determine the natural convection heat transfer from the solid particles, the heat transfer coefficient was calculated by using the Nusselt, $\overline{Nu_{\tilde{L}}}$, number (Thomas, 1992):

$$\overline{Nu_{\tilde{L}}} = \frac{\bar{h}.\tilde{L}}{k} \tag{9.1}$$

where $\bar{h}$ is the heat transfer coefficient from the solid surface, $\tilde{L}$ is the characteristic length of the particle, which for a sphere is $\pi D/2$ and k is the gaseous phase thermal conductivity. $\overline{Nu_L}$ can be calculated using:

$$\overline{Nu_{\tilde{L}}} = \left(a + 0.331b.Ra_{\tilde{L}}^{1/6}\right)^2 \tag{9.2}$$

where a is 1.77 for spheres, b equals $\frac{1.17}{\left[1+(0.5/\mathrm{Pr})^{9/16}\right]^{8/27}}$, $Ra_{\tilde{L}}$ is the Rayleigh number and Pr is the Prandtl number. $Ra_{\tilde{L}}$ and $\overline{Nu_{\tilde{L}}}$ were determined for each particle size and material type. The heat transfer coefficients will differ for different particle sizes and temperature differences. The convective heat transfer rates to or from the different material, $Q_{c,i}$, were calculated using Equation 9.3:

$$Q_{c,i} = \bar{h}_i A_i \left(T_{mean} - T_i\right) \tag{9.3}$$

where the subscript i denotes the material type, A_i is the heat transfer area taken as the total surface area for material i, T_{mean} was the mean gas temperature in the control volume and T_i was the temperature of material i.

The heat transfer, $q_{c,i}$, was then calculated for each material type and size using:

$$q_{c,i} = Q_{c,i}.\tau_{SAMP} \tag{9.4}$$

where τ_{SAMP} is the time step or sampling time as determined in Chapter 8. Finally, the total convective heat transfer from the ash was compared and balanced with the total convective heat transfer to the shale. It was important to balance the total heat transfer to ensure that the heating or cooling of the materials was realistic. The

smallest total heat transfer magnitude was taken as the real total heat transfer and the other heat transfer values were adjusted accordingly.

9.1.3 Radiation heat transfer

The radiation heat transfer was important due to the high temperatures and the large particle sizes used in the AOSTRA-Taciuk Processor (Saatdjian & Large, 1988). Radiation heat transfer occurred from the hot material, the ash, to the cold material, the shale. The ash referred to in this chapter is the hot combusted spent shale described in Chapter 1. The mean temperatures of the ash and shale were calculated. The radiation heat transfer rates, $Q_{r\text{-}SHALE}$, to the shale from the ash were determined for each shale size, *i*, from the mean ash temperature, $\overline{T}_{ASH}$, as:

$$Q_{r-SHALE,i} = \sigma \varepsilon A_{Rad} \frac{l(t)}{l_f} . \frac{A_{SHALE,i}}{\sum A_{SHALE,i}} \left(\overline{T}_{ASH}{}^4 - T_{SHALE,i}{}^4 \right) \tag{9.5}$$

where σ is the Stefan-Boltzmann constant, ε is the emmissivity of the solids, which was taken to be representative of the emmissivity of soils of 0.90 (Thomas, 1992), A_{Rad} is the area of radiation heat transfer, which was equal to the minimum of either the total ash or the total shale surface area, $\frac{l(t)}{l_f}$ is the extent of mixing from Chapter 6, $A_{SHALE,i}$ is the surface area for the i^{th} shale sample. $T_{SHALE,i}$ is the mean temperatures of the i^{th} shale component in the control volume. The radiation heat transfer rate from the ash was calculated by switching the ash and shale values in Equation 9.5.

The total radiation heat transfer, $q_{r,i}$, for each material, *i*, was calculated using:

$$q_{r,i} = Q_{r,i} . \tau_{SAMP} \tag{9.6}$$

The radiation heat transfer to the shale was compared and balanced with the radiation heat transfer from the ash to ensure that the heat transfer was physically realistic.

9.1.4 Total heat transfer between the granular materials

Now the total heat transfer to or from a material in a control volume was taken as the sum of the convective and radiative heat transfers. Thus:

$$q_i = q_{c,i} + q_{r,i} \tag{9.7}$$

However, the process being modelled was an unsteady state process and thus the heat transfer resulted in changes to the temperatures of the materials. The heat transfer needed to be re-evaluated at each time step due to changes in mixing, segregation and material temperatures. This is considered in the next section.

The specific enthalpy of the material, $\overline{H}(t)$, was calculated using:

$$\overline{H}_i(t) = \overline{H}_i(t-1) + \frac{q_i(t)}{m_i} \tag{9.8}$$

where $\overline{H}_i(t-1)$ is the specific enthalpy of the material prior to the heat transfer in the latest time step, $q_i(t)$ is the heat transfer in the last time step, m_i is the original mass of that material type and size. The specific enthalpy was expressed per mass of original material.

9.1.5 Calculation of the new material temperatures and the amount of volatile evolution

In order to calculate the new temperatures of the materials and the amount of volatile evolution, the thermal behaviour of the materials had to be known. Berkovich (1999) studied the thermal behaviour of the Australian oil shales and ashes and his models were used in this part of the thesis to complete the modelling of the retort zone of the AOSTRA-Taciuk Processor. The enthalpy data was determined for shale with the composition shown in Table 9.1. Only one shale type was tested using the newly developed simulation.

Material	Composition	Reaction Temperature Range	Reaction Enthalpy	Decay Constant
	%	K	J/g	K
Water	25	343-393	564.75	17.37
Kerogen[1]	20	743-793	159.85	21.71
Smectite[1]	20			
Kaolinite[1]	5			
Illite[1]	5			
Quartz	10	844-858	-1.04	4.34
Pyrite	2	738-748	5.81	4.34
Gypsum	1	400-410	5.91	4.34
Siderite	3	740-750	17.55	4.34
Dolomite[2]	3	>950	41.94	21.71
Calcite[2]	6	>990	101.89	21.71
TOTAL	100		896.66	

Notes:
1) These materials reacted in the same temperature range and thus the reaction enthalpy of the kerogen included the enthalpy of the other reactions.
2) The temperature range was assumed to be 40 K for the determination of the decay constant.

Table 9.1: Shale sample used in the simulation.

The model by Berkovich (1999) was used to determine the enthalpy of the shale and ash at different temperatures. For the shale, this enthalpy was the sum of the sensible heat and the reaction heat due to the decomposition of various minerals. For the ash, the enthalpy was simply the sensible heat as it was assumed that the reactions occurring during the thermal decomposition were irreversible. The specific enthalpy profiles of the shale and ash of Table 9.1 are shown in Figure 9.1 and expressed the enthalpy of the material in J/g of original material against the temperature of the material. Berkovich (1999) assumed that the reactions were completed at a single temperature and this assumption produced the steps observed in the "shale specific enthalpy" curve shown in Figure 9.1. However the decomposition reactions occurred over a significant temperature range. The temperature range and the enthalpy of reaction of these components are shown in Table 9.1. These steps of specific

enthalpy were larger than the changes in specific enthalpy occurring in a simulation time step. The steps were thus approximated using exponential decay curves by assuming that the reaction started at the lower temperature and was 90% completed at the higher temperature of the temperature range shown in Table 9.1. Since the enthalpy at all temperatures was expressed in J/original g of material, the heat transfer was facilitated by allowing simple addition and subtraction of specific enthalpies to the materials as shown in Equation 9.8.

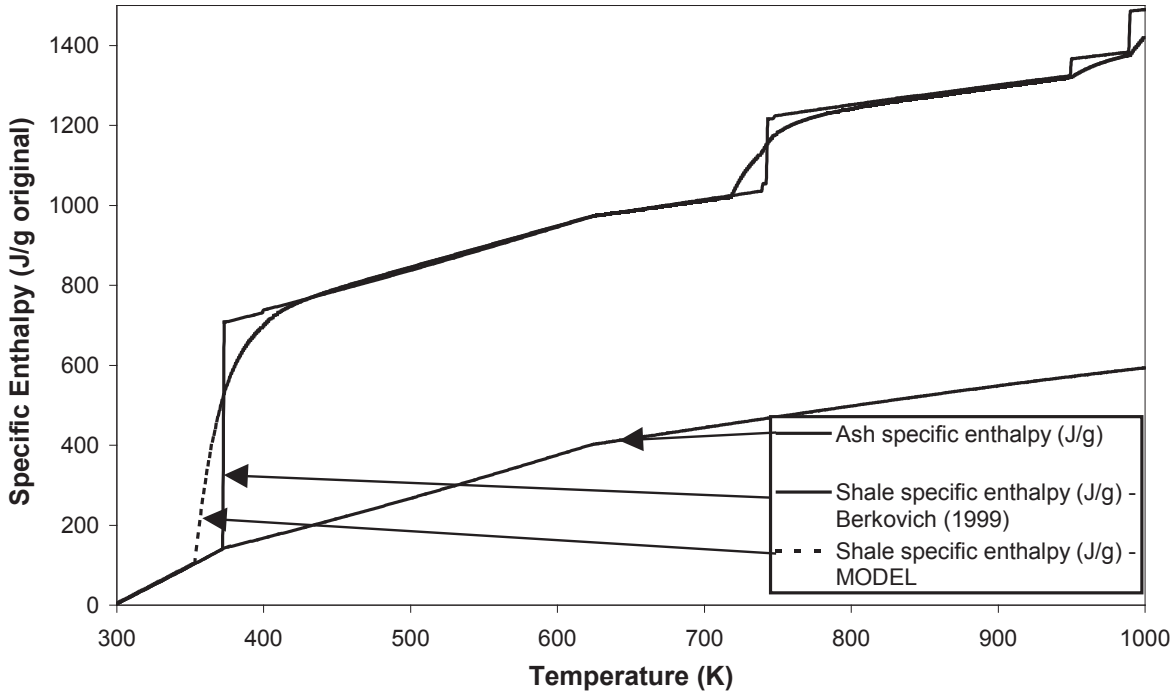

Figure 9.1: Enthalpy content of the shale and ash sample described in Table 9.1 (Berkovich, 1999).

The total enthalpy of the material was determined using the initial enthalpy of the material and the heat transfer predicted by Equation 9.7. From this new enthalpy, the temperature of the material can be found using the data from Figure 9.1. The total volatile evolution can be determined using the new temperature and the thermo-gravimetric analysis data shown in Figure 9.2.

Figure 9.2 is the mass loss curve, obtained from a thermo-gravimetric analysis of a Stuart oil shale sample. The amount of mass lost can be evaluated at any temperature

between 300 and 1000 K. This mass loss was representative of the amount of volatile evolution and the amount of moisture loss. To determine the amount of volatile evolution, the moisture loss was subtracted from the total mass loss. This moisture loss was assumed to include any mass loss below 523 K as this was the temperature at which the shale entered the retort zone in the AOSTRA-Taciuk Processor. Figure 9.2 has been corrected so that it corresponds to the moisture content of the shale specified in Table 9.1. As can be seen, the mass loss between 523 K and the kerogen peak at approximately 750 K was approximately 20%, corresponding to the material specification of kerogen. The shale was the only material that underwent pyrolysis and mass loss. The ash, which already was fully pyrolysed, could not regain the mass it lost due to the irreversibility of the reactions, and thus its thermal characteristics were quite different.

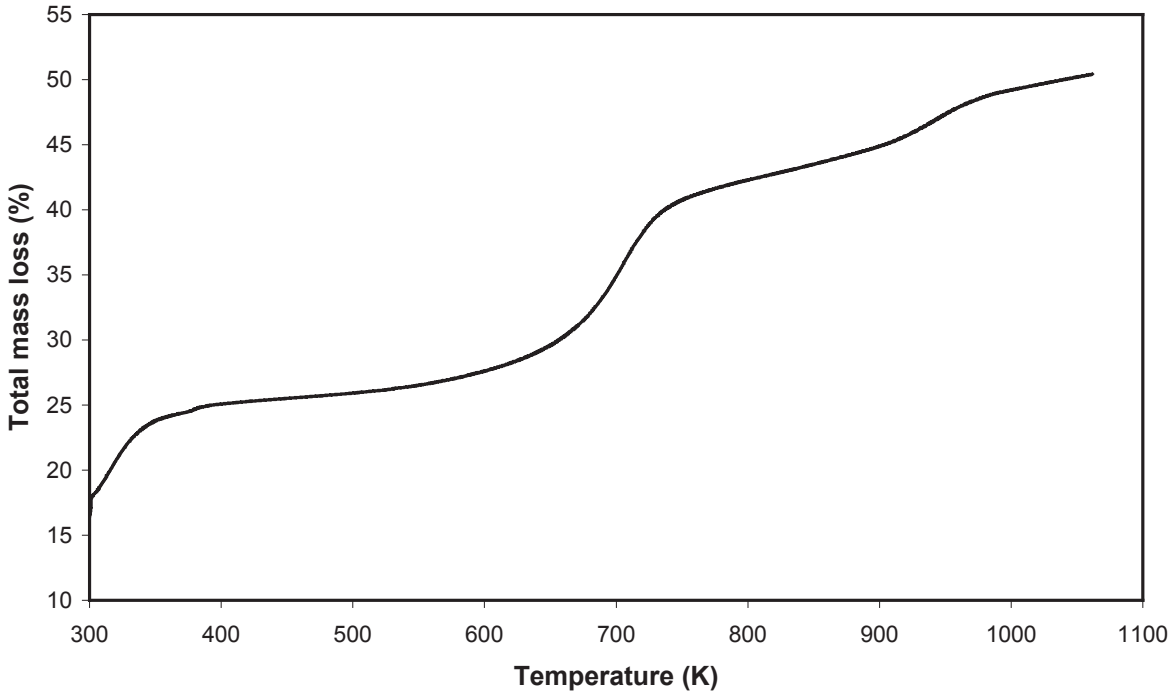

Figure 9.2: Mass loss of the shale sample described in Table 9.1.

9.2 SIMULATION OF THE RETORT ZONE OF THE AOSTRA-TACIUK PROCESSOR

In Chapter 8 a simulation model was developed for a rotating kiln and the mixing and segregation mechanisms of this simulation were also validated. Deviations were observed between the experimental and simulation results but it was shown that increasing the drum size reduced these deviations. Increasing the drum size resulted in faster mean active layer velocities, which reduced the deviation between the experimentally measured and the simulation predicted mixing times. Increasing the drum diameter also reduced the segregation effect.

The heat transfer mechanism described in section 9.1 was added to the simulation and the dynamic behaviour of the retort zone of the AOSTRA-Taciuk Processor was tested in this section of the thesis.

9.2.1 Material properties

The physical and chemical properties of the materials are shown in Table 9.1. Only one sample of shale and ash was used to simplify the simulation. The simulation could be extended to allow different material compositions to be used but that was not within the scope of the research. The shale sample used to test the simulation is representative of the Stuart oil shale deposit (Berkovich, 1999).

9.2.2 Case studies of the AOSTRA-Taciuk Processor operation

Industrial data for the AOSTRA-Taciuk Processor was not available and thus could not be used for the validation of the simulation. To test the heat transfer model four different operational variables were varied and the retort zone of the AOSTRA-Taciuk Processor behaviour was studied. These variables were the mean particle size, the initial temperature of the materials, the ratio of the materials and the rotational

velocity of the drum. The different test cases are summarised in Table 9.2. The rate of volatile evolution was calculated in each case and compared to the rate of volatile evolution for the standard case, as shown in Case 2.

9.2.3 Results from Case 2

The results from Case 2 were compared to the results from the other simulation tests. A detailed study was completed on Case 2 to test the performance of the simulation.

		Material Properties				
Case number	**Drum size**	**Composition**	**Mean Size[1] (Shale/Ash)**	**Initial Temperature (Shale/Ash)**	**Ratio (Shale:Ash)**	**Rotational Velocity**
	m		mm/mm	K/K	-	rpm
1	6	As per Table 9.1	1.00/1.00	548/1048	0.32	5
2	6	As per Table 9.1	1.54/2.11	548/1048	0.32	5
3	6	As per Table 9.1	1.70/1.70	548/1048	0.32	5
4	6	As per Table 9.1	2.51/2.51	548/1048	0.32	5
5	6	As per Table 9.1	3.44/3.44	548/1048	0.32	5
6	6	As per Table 9.1	5.08/5.08	548/1048	0.32	5
7	6	As per Table 9.1	1.54/2.11	498/998	0.32	5
2	6	As per Table 9.1	1.54/2.11	548/1048	0.32	5
8	6	As per Table 9.1	1.54/2.11	598/1198	0.32	5
9	6	As per Table 9.1	1.54/2.11	548/1048	0.26	5
2	6	As per Table 9.1	1.54/2.11	548/1048	0.32	5
10	6	As per Table 9.1	1.54/2.11	548/1048	0.49	5
11	6	As per Table 9.1	1.54/2.11	548/1048	0.58	5
12	6	As per Table 9.1	1.54/2.11	548/1048	0.69	5
13	6	As per Table 9.1	1.54/2.11	548/1048	0.32	3
14	6	As per Table 9.1	1.54/2.11	548/1048	0.32	4
2	6	As per Table 9.1	1.54/2.11	548/1048	0.32	5
15	6	As per Table 9.1	1.54/2.11	548/1048	0.32	6
16	6	As per Table 9.1	1.54/2.11	548/1048	0.32	7

NOTES:
1) The shale and ash size specifications for the AOSTRA-Taciuk Processor were 1.54 mm and 2.11 mm respectively. These particle sizes were obtained using a mixture of the experimental particle sizes.

Table 9.2: Details of the case studies.

9.2.3.1 Mixing and segregation of Case 2

The mixing of the bed in the AOSTRA-Taciuk Processor is shown in Figure 9.3. This figure indicates that the mixing reached the maximum point of mixing after 39 seconds. The bed de-mixed itself after reaching this maximum. This was very unusual and was not observed for the mixing tests of Chapter 8. A possible explanation for this was due to the segregation of materials since multi-sized materials were used in Case 2 and only a single sized particle ranges were used in the simulation experiments of Chapter 8.

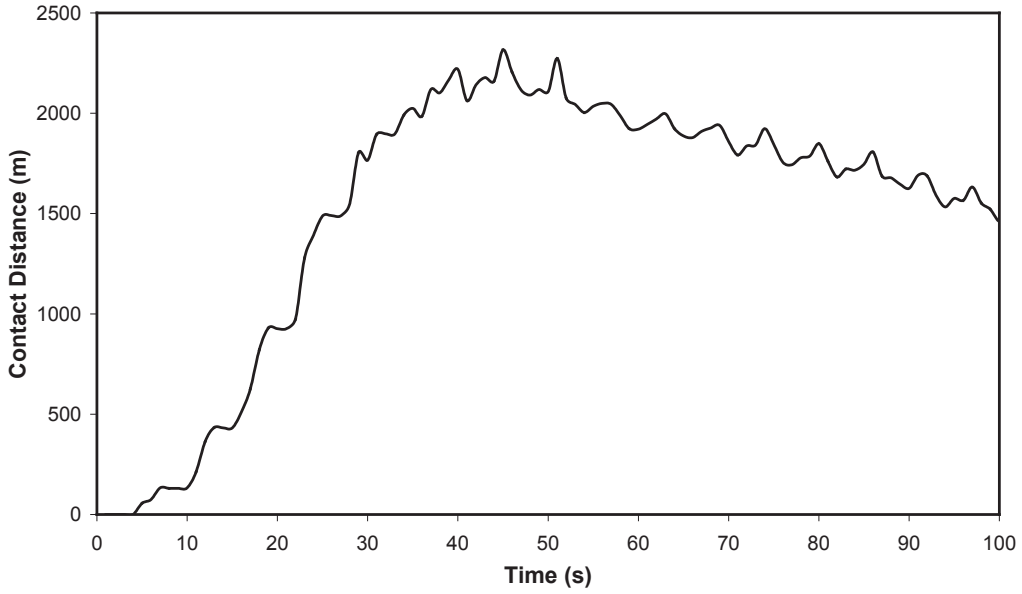

Figure 9.3: Mixing dynamics of Case 2.

The mean particle sizes, after 220 seconds of simulation time, in the different 'stagnant layer' layers are shown in Figure 9.4. 'Stagnant layer' 1 was closest to the wall and 'stagnant layer' 5 was closest to the rotational centre of the bed. As can be seen, there was significant size segregation at this time. The mean 'active layer' velocity in Case 2 was 7.01 ms^{-1} and using the segregation model of Chapter 7, segregation would not occur at this velocity. However velocities in some 'active layer' control volumes were less than the mean calculated velocity. The lowest velocity of

1.60 ms^{-1} occurred in the grey 'active layer' control volumes of Figure 8.6 and these low velocities allowed the materials to segregate.

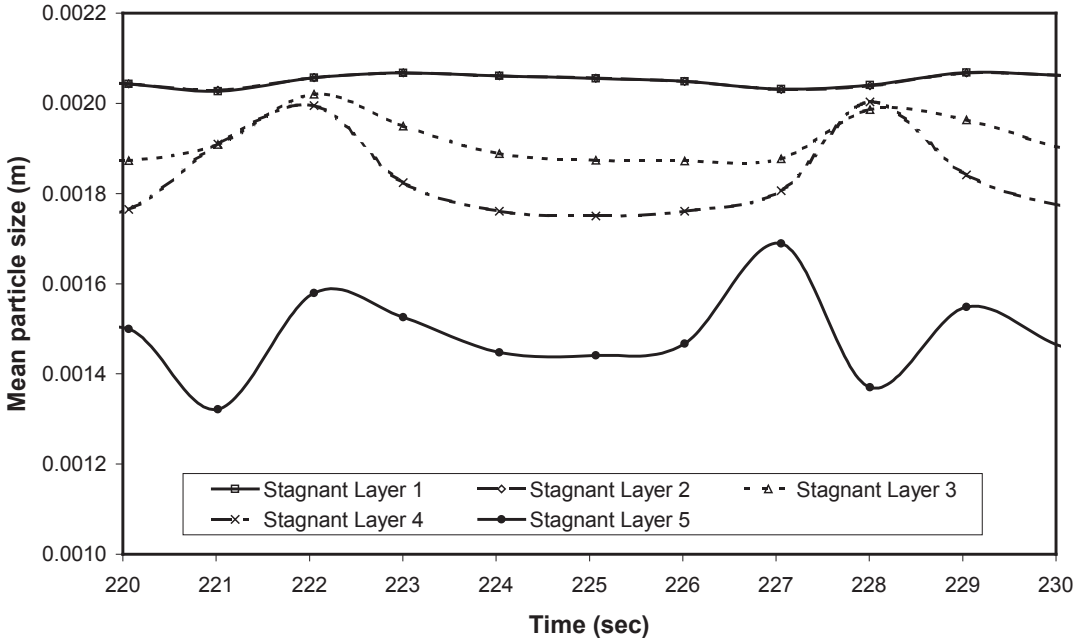

Figure 9.4: Final segregated configuration of Case 2.

These results indicated that segregation is important in industrial rotating kilns. This segregation would not be observed if the 'active layer' was considered as a single entity, as it was in the experiments, rather than the 22 individual control volumes that were used in the simulation. This is an advantage of using 22 single control volumes to simulate the 'active layer' rather than one single entity.

9.2.3.2 Heat transfer, mean shale temperature and volatile evolution of Case 2

The important aspect of this part of the simulation was to test the heat transfer model derived earlier in the chapter. Figure 9.5 shows the mixing extent and the mean temperature of the shale. The mean shale temperature was closely linked to the mixing extent of the material.

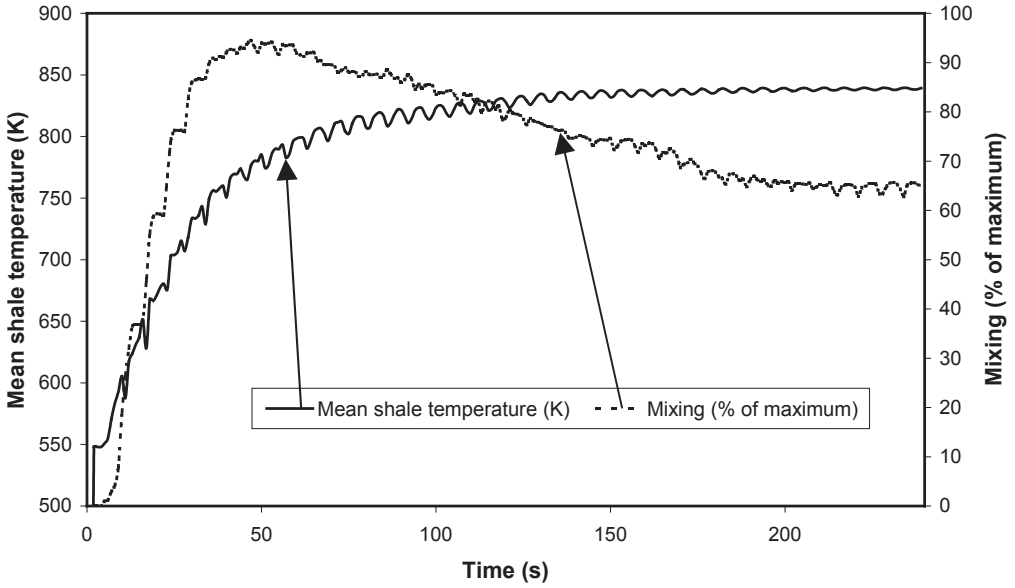

Figure 9.5: Mean shale temperature and mixing extent for Case 2.

It was noted that fluctuations occurred in the mean shale temperature. This indicated that the mean shale temperature decreased at certain times in the simulation. The drops in the mean shale temperature coincided with the time required for the bed to move through one complete revolution. Furthermore, the temperature dropped as the mixing extent increased. Thus it was considered that the drop in the mean shale temperature was due to the movement of material from the 'stagnant layer' into the 'active layer'. The experimental results shown in Figure 6.2 indicate that most of the mixing occurred near the interfaces of the different materials. The presence of these high zones of contact distance resulted in higher heat transfer rates in those zones. Due to the higher heat transfer rates the shale was heated beyond the average shale temperature. This was especially the case for the 'stagnant layer', which had a significant residence time. As the material moved from the 'stagnant layer' into the 'active layer', the hot shale was mixed with cooler shale. As the "stream" structure of Chapter 8 only allowed for one temperature of each material type and size, a new temperature was calculated for the new combined "stream". This temperature calculation used the enthalpy balance for the shale. However, the enthalpy balance is not linear and thus the new shale temperature is not equal to the mean shale

temperature of the different feeds. This non linearity caused the periodic fluctuations observed in the mean shale temperature.

9.2.4 Results from the case studies

The case studies described in Table 9.2 were simulated and the volatile evolution was calculated. In each case the dynamics of the volatile evolution was plotted in the main chart of Figures 9.6 to 9.9. The inset in these figures represented the final volatile evolution for each case.

9.2.4.1 Mean particle size effects

The mean particle size effect was tested from 1.00 mm to 5.08 mm. Case 2 had a mean shale size of 1.54 mm and a mean ash size of 2.11 mm as described in Table 9.1. Cases 1, 3, 4, 5 & 6 had the same shale and ash particle sizes of 1.00, 1.70, 2.51, 3.44 and 5.08 mm respectively.

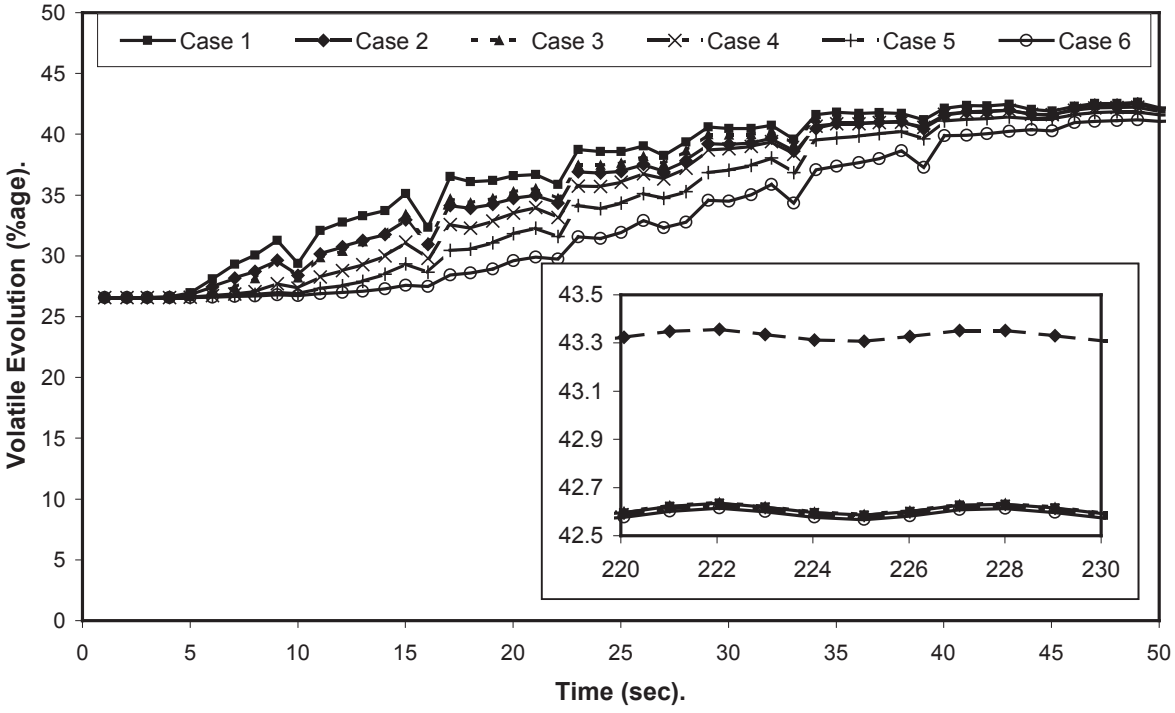

Figure 9.6: Simulation results for testing different mean particle sizes.

The decrease in particle size ensured faster mixing as per the mixing mechanism of Chapter 6. This was reflected in Figure 9.6 by faster evolution of volatiles. By using smaller particle sizes the heat transfer occurred more rapidly because the rate of particle heating was inversely proportional to the size of the particle. The final volatile evolution results for the different particle sizes are shown in the inset of Figure 9.6. It should be noted that all the cases, except for Case 2, reached the same final state. This indicated that using a mixture of particle sizes compared to a single particle size resulted in more volatiles being produced. This was due to the enthalpy of the particles, as the enthalpy of particles was dependent on the size of the particles. In Cases 1 and 3 to 6, the ratio of enthalpy of the shale to the ash was identical as the same material size and ratios were used. However in Case 2 the enthalpy of the ash was higher than the enthalpy of the shale due to the higher mean particle size. This allowed more heat to be exchanged so that the shale reached a higher temperature compared to the other cases. This higher temperature resulted in a higher amount of final volatile evolution.

A further observation should be made regarding the fluctuations observed in Figure 9.6. The temperature fluctuations were described in the previous sections. The volatile evolution is closely related to the temperature of the shale as shown in Figure 9.2. The periodic decreases in volatile evolution were due to the drop in the mean shale temperature described above. Physically it would be impossible for the shale to regain the volatiles that were evolved at a higher temperature and this was a limitation of the "stream" structure. These fluctuations should be ignored and the volatile evolution should be extrapolated across the troughs.

9.2.4.2 Initial temperature of the materials effects

Different initial temperatures of the materials were tested. It was expected that this should strongly affect the heat transfer rate and the total amount of volatile evolution. These results are shown in Figure 9.7.

By increasing the initial temperatures of the shale and the ash the rate of volatile evolution increased. This was due to the larger heat transfer rate, especially with respect to the radiation heat transfer. The net result being that the final volatile evolution also increased by increasing the initial temperatures.

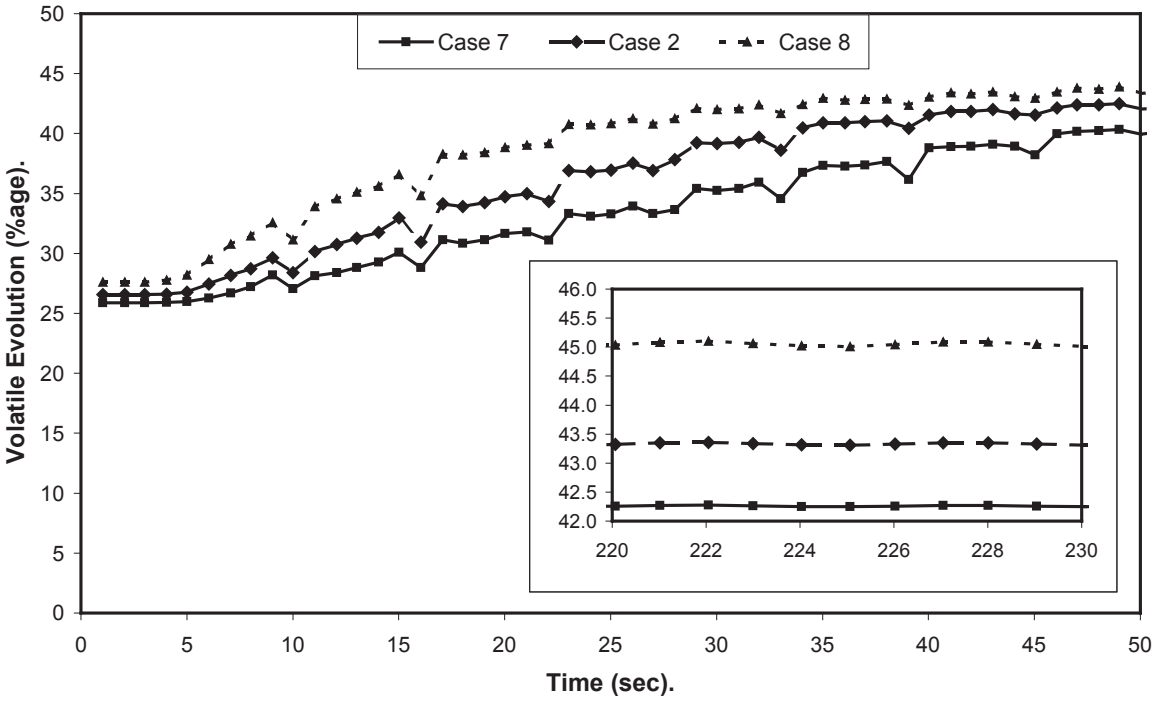

Figure 9.7: Simulation results for testing different initial material temperatures.

9.2.4.3 Ratio of the materials effects

Five different material ratios were considered. It was expected that decreasing the shale to ash ratios should increase the mixing rate and thus the heat transfer. This was reflected by the increased rate of volatile evolution with smaller shale to ash ratios shown in Figure 9.8. As expected from an energy balance, increasing the ratio of the shale to the ash reduced the final shale temperature and thus reduced the total volatile evolution.

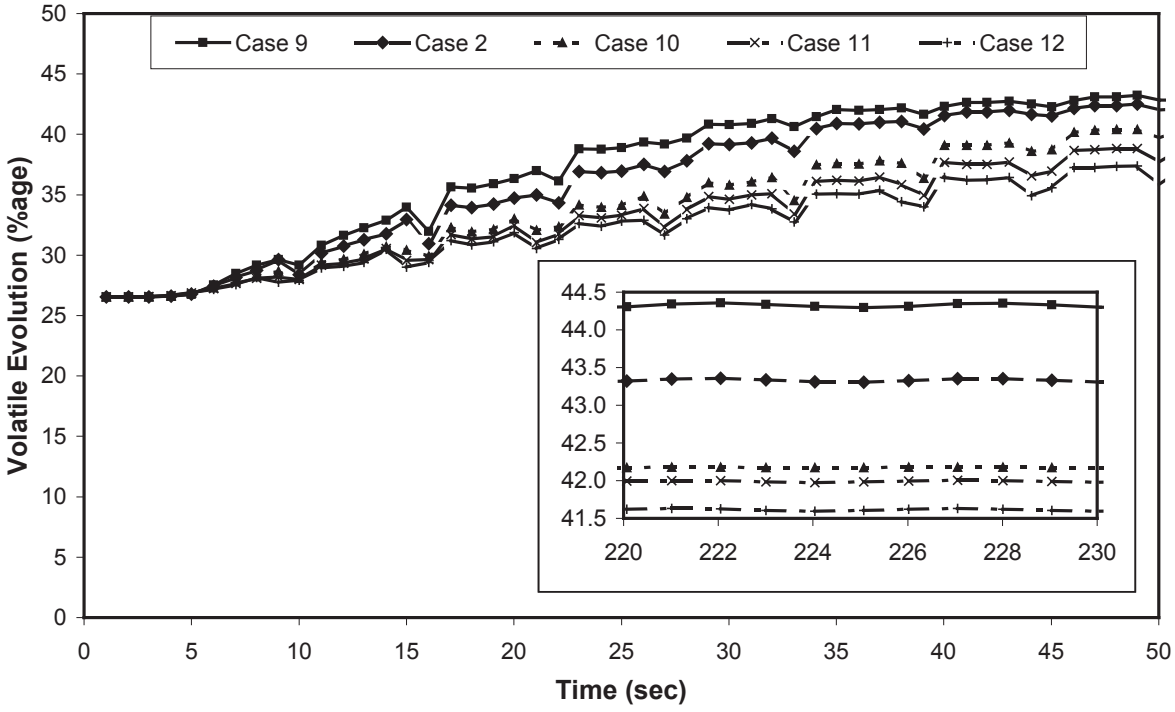

Figure 9.8: Simulation results for changes in the material ratio.

9.2.4.4 Rotational velocity effects

Changing the rotational velocity changed the mixing rate as shown in Chapter 6. The effect of changing the rotational velocity on volatile evolution is shown in Figure 9.9.

Increasing the rotational velocity increased the rate of mixing and thus increased the rate of volatile evolution. Figure 9.9 shows that the periodic fluctuations in the volatile evolution discussed in section 9.2.4.1 were indeed dependent on the rotational velocity since the period of fluctuations in Figure 9.9 corresponded to the time of rotation of the material in the bed.

The rotational velocity also affected the final amount of volatile evolution. This is unexpected in that the rotational velocity should not affect the final amount of mixing, only the mixing rate.

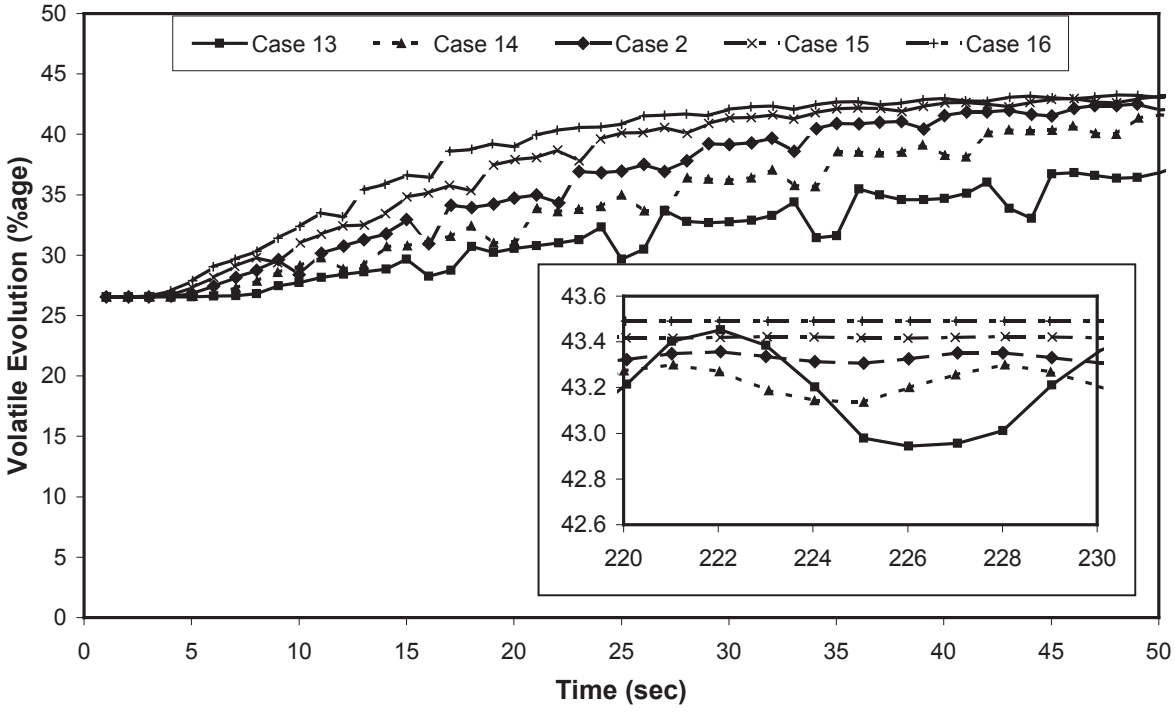

Figure 9.9: Simulation results for different rotational velocities.

However, the final contact distance was measured and this final contact distance increased when increasing the velocity. This arose due to the segregation of the material, since multi-sized feeds were used in the simulation. The simulations carried out at the lower velocities were more segregated compared to the results from the simulation at the higher velocities. Since the shale and the ash had different mean particle sizes, the segregation resulted in having more shale concentrated towards the centre and the larger ash material towards the edge of the bed. The total heat transfer was reduced because of this separation of the shale and the ash. The reduction in heat transfer reduced the amount of volatile evolution.

9.3 LIMITATIONS OF THE SIMULATION

The cases studied in this chapter tested only a few possible parameters that may have important implications on the behaviour of the retort section of the AOSTRA-Taciuk Processor. The assumptions made in the heat transfer model must be noted

before applying the model. Furthermore, the model was limited to a single type of oil shale. The prediction of the volatile evolution only estimates the amount of volatiles that will leave the AOSTRA-Taciuk Processor, it does not predict the quality of these volatiles.

9.4 CHAPTER SUMMARY

In this chapter the simulation as derived in Chapter 8 was extended to include the granular heat transfer between the preheated shale and the combusted spent shale in the AOSTRA-Taciuk Processor.

The heat transfer model combined convective and radiative heat transfer mechanisms. The amount of volatile evolution was calculated from the thermodynamic study of oil shales by Berkovich (1999) and the developed granular heat transfer model.

Industrial data was not available to test the simulation so a case study was carried out to suggest how the volatile evolution of the shale would be affected by changing certain operational parameters. The case study suggested that the volatile evolution rate in the AOSTRA-Taciuk Processor could be increased by reducing the particle size. It was found that the final amount of volatile evolution was greater by using a multi-sized particle range compared to using a uniform particle size. Increasing the initial temperatures of the materials resulted in a higher volatile evolution rate and a higher final amount of volatile evolution. By reducing the ratio of shale to ash, the volatile evolution rate and the final volatile evolution was also increased. However, it is not known whether the extra final volatile evolution obtained was a desirable product or a byproduct from the mineral side reactions. Lastly, increasing the rotational velocity increased the rate of volatile evolution due to the faster mixing rates and also increased the final amount of volatile evolution.

CHAPTER 10

Conclusions

Section 1.3 outlined the research objectives of this thesis. In line with the research objectives, the conclusions of the current work are as follows:

1. The review of the rotating kiln literature showed that there is a lack of quantitative models to predict the mixing and segregation of solids in rotating drums. The models available only had limited applications and could not be used to predict the behaviour of the AOSTRA-Taciuk Processor, due to its unique nature. The need for new predictive models was apparent.

2. Suitable experimental methods were developed, involving image analysis, to measure the mixing and segregation behaviour in a laboratory sized rotating drum. Further experiments were carried out to determine the behaviour of the active layer since it was shown in the literature that the active layer was important in the mixing, segregation and heat transfer in a rotating kiln. The success of the mixing and segregation models was attributed to the use of the active layer parameters. Studying the active layer showed how the movement of material, which caused mixing and or segregation was related to the drum size and scaling parameters were developed with respect to the operational variables of rotating kilns.

3. A constant rate mixing mechanism was observed. However, on closer analysis it was shown that mixing occurs through a series of steps coinciding with the times when the materials entered the active layer. This was physical proof that mixing only occurred in the active layer of a rolling bed. The mixing of solids were modelled successfully with changes in the following parameters: rotational velocity, particle size, drum loading and material ratio. Complete mixing modelling required the determination of both the mixing rate and the final contact distance between the two materials being mixed. An active layer parameter was

developed and a linear relationship was found to exist between this active layer parameter and the mixing rate. Similarly a linear relationship was observed between the final contact parameter and the final contact. The mixing model was tested against independent experiments and accurately predicted the mixing behaviour of mixing in different sized rotating drums.

4. The segregation of solids in a rotating drum was successfully modelled with changes in the active layer velocity and the particle size ratio of the two materials. The segregation dynamics occurred too fast to be modelled and it was assumed the segregation dynamics in large industrial rotating kilns were negligible. The segregation model thus only considered the final segregated configuration of the bed. The segregation model was tested against independent experiments and accurately predicted the final segregated configuration.

5. A simulation computer code was developed to simulate mixing and segregation in a rotating drum. This simulation utilised the mixing and segregation models derived in Chapters 6 and 7, respectively. It was shown that the final amount of mixing was predicted accurately by the simulation. However, the mixing dynamics and the final segregated configuration were not predicted as accurately and this was due to the lower velocities experienced in the control volumes of the grid compared to the mean active layer velocity used in the modelling of the mixing dynamics and the final segregated state. However, it was shown, that by increasing the active layer velocity – due to increases in the drum diameter or the rotational velocity - that the deviation between the experimental results and those predicted by the simulation decreased. This would indicate that the simulation could be used to predict the mixing and segregation behaviour in industrial rotating kilns.

6. A heat transfer model was derived to determine the heat transfer between granular materials in a bed of solids. This model included convective and radiative heat transfer mechanisms and assumed that the heat transfer was pseudo steady in order to determine the heat transfer rate. Previous

work on the thermodynamic behaviour of oil shales was included in the heat transfer model to allow realistic volatile evolution rates to be predicted.

7. The simulation from Chapter 8 was extended to include the heat transfer model. This allowed the retort section of AOSTRA-Taciuk Processor to be simulated. The inclusion of typical thermal behaviour of oil shale allowed the rate of volatile evolution to be predicted within the industrial rotating kiln. Unfortunately this simulation could not be verified with industrial data, as that information was not available. However, a case study was carried out which tested operational variables available as part of the simulation. Higher rates of volatile evolution were possible by reducing the size of the material. Changing the material sizes did not effect the total amount of volatiles evolved unless different material sizes were used for the shale and ash. Increasing the initial material temperatures or reducing the shale to ash ratio increased the rate of volatile evolution and the final amount of volatiles. Lastly, increasing the rotational velocity increased both the volatile evolution rate and the final amount of volatiles.

8. The objectives of the research were achieved.

Nomenclature

Symbol	Units	Notes
$\ddot{A}$	-	Dynamic computer array to store the image information
A	m^2	Particle surface area
A_{AL}	m^2	Transverse area of the stagnant layer
A_{BED}	m^2	Transverse area of the bed
A_i	m^2	Convective heat transfer area for the i^{th} fraction
A_{Rad}	m^2	Radiative heat transfer area
$A_{SHALE,i}$	m^2	Surface area of the i^{th} shale fraction
A_{SL}	m^2	Transverse area of the active layer
a	-	Experimental constant
b	-	Experimental constant
$\boldsymbol{c}$	-	Column of the image
$C(x,t)$		Concentration at any position x and time t
D	m	Drum diameter
$\eth_{Diff}$	m^2/s	Diffusion coefficient
d_i	m	Mean particle size of the inner layer of the bed
d_o	m	Mean particle size of the outer layer of the bed
d_p	m	Particle diameter
Fr	-	Froude number (ratio of centrifugal to gravitational forces)
f	-	Mathematical function

g	m/s²	Acceleration due to gravity
H	-	Height of the image in pixels
$\overline{H}_i(t)$	J/g	Enthalpy per unit original mass of the material at time t
$\overline{h}$	W/m².K	Heat transfer coefficient
$\overline{h}_i$	W/m².K	Heat transfer coefficient for the i^{th} ash or shale fraction
i_j	-	Intercept for segregation model for layer j
$i_j(PSR)$	-	Intercept for the segregation model for layer j as a function of PSR
j	-	Layer index
k	W/m.K	Thermal conductivity of the material
k_e^0	W/m.K	Effective thermal conductivity of a stationary granular medium
k_e	W/m.K	Effective thermal conductivity of a moving granular medium
k_e^t	W/m.K	Effective thermal conductivity due to the flow of material
$\widetilde{L}$	m	Characteristic length, equals $\pi.d_p/2$ for spherical particles.
L	-	Loading of the drum expressed as a percentage of the drum volume
$l(t)$	mm, m	Contact at time t
l_0	mm, m	Initial contact
l_f	mm, m	Final contact
M	-	Degree of mixing, equals zero for a non mixed system, equals 1 for a fully mixed system, Rose (1959)
m	-	Index = 0.5

m_i	g	Original mass of the material
m_j	-	gradient of segregation model for layer *j*
$m_j(PSR)$	-	Gradient for the segregation model for layer *i* as a function of *PSR*
N	rpm	Rotational velocity of the drum
$\overline{Nu_L}$	-	Nusselt number
P_j	-	Proportion of segregated material in layer *j*
$P_o(t)$	-	Order parameter for segregation, Cantelaude et al (1997)
Pr	-	Prandtl number
PSR	-	Particle size ratio, large particle size divided by the smaller particle size
$Q_{c,i}$	W	Convective heat transfer rate to the i^{th} ash or shale fraction
$Q_{r\text{-}SHALE,i}$	W	Radiative heat transfer rate to the i^{th} shale fraction
$q_{c,i}$	J	Convective heat transfer to the i^{th} ash or shale fraction
q_i	J	Total heat transfer to the i^{th} ash or shale fraction
$q_{r,i}$	J	Radiative heat transfer to the i^{th} ash or shale fraction
R	m	Drum radius
Ra_L	-	Rayleigh number
R_A	m	Distance from Apex A to the centre of rotation, Figure 5.1
R_B	m	Distance from Apex B to the centre of rotation, Figure 5.1
$\boldsymbol{r}$	-	Row of the image
S_n	1/s	Segregation rate, Pollard & Henein (1989)

$\overline{T}_{ASH}$	K	Average temperature of the ash
T_i	K	Temperature of material *i*
T_{mean}	K	Temperature of the gas phase in a control volume
$T_{SHALE,i}$	K	Temperature of the i^{th} shale fraction
t	s	Time
t_1	s	Mixing time for material 1, Woodle & Munro (1993)
t_2	s	Mixing time for material 2, Woodle & Munro (1993)
t_m	s	Time required to fully mix the material in the bed.
U	W/m².K	Overall heat transfer coefficient to the particle
$\overline{V}_{AL}$	m/s	Mean active layer velocity
$\overline{V}_{SL}$	m/s	Mean stagnant layer velocity
W	-	Width of the image in pixels
x	m	Distance
X_0	-	X location of the centre of rotation
X_A	-	X location of Apex A
X_{AL}	-	Active layer proportion
Y_0	-	Y location of the centre of rotation
Y_A	-	Y location of Apex A
ΔQ	W	Heat transfer to the particle
ΔT	K	Temperature difference between the particle and its surroundings
Φ_{SL}	m².m/s	Stagnant layer flux
Γ	mm/s, m/s	Mixing rate
$\Gamma(t)$	mm/s,	Mixing rate at time *t*

	m/s	
ς	-	Segregation rate, Rose (1959)
α_A	-	Angle between Apex A and the centre of rotation
α_{AB}	-	Angle between Apex A and Apex B
β	-	Angle from the centre of rotation to the pixel
ε	-	Emmissivity of the solids, taken to be 0.90
ϕ	mm/s, m/s	Active layer flux parameter
γ	-	Angle of inclination of the drum
κ	-	Material ratio
λ	mm, m	Final contact parameter
μ_1	-	Ratio of frictional coefficient for material 1, Woodle & Munro (1993)
μ_2	-	Ratio of frictional coefficient for material 2, Woodle & Munro (1993)
σ	$W/m^2.K^4$	Stefan Boltzmann constant
τ	s	time constant characterising kinetics of segregation
τ_{min}	s	Minimum residence time
τ_{SAMP}	s	Sampling time, time step
$\tau_{SLCV,res}$	s	Residence time of the stagnant layer control volumes
ω	rad/s	Rotational velocity of the drum
ω_c	rad/s	Critical rotational velocity of the drum

References

Alonso, M., Satoh, M., Miyanami, K., "*Optimum combination of size ratio, density ratio and concentration to minimize free surface segregation*", Powder Technol., **68**, 145-152 (1991).

Arpaci, V., "*Conduction Heat Transfer*", Addison Wesley, London (1966).

Australian Institute of Petroleum, "*Queensland oil shale plans may bring Australian petroleum industry back to its roots*", Petroleum Gazette, **28**, 3-10 (1993).

Baker, C., G., "*Air-solids drag in cascading rotary dryers*", Drying Technol., **10**, 365-393 (1992).

Barker, J., J., "*Heat transfer in packed beds*", Ind. Eng. Chem., **57**, 43-51 (1965).

Barr, P., Brimacombe, J., Watkinson, A., "*A heat transfer model for the rotary kiln: Part 1. Pilot Kiln Trials*", Metall. Trans. B, **20B**, 391-402 (1989a).

Barr, P., Brimacombe, J., Watkinson, A., "*A heat transfer model for the rotary kiln: Part 2. Development of the Cross Section Model*", Metall. Trans. B, **20B**, 403-419 (1989b).

Berkovich, A., J., Young, B., R., Levy, J., H., Schmidt, J., S., "*Thermal characteristics of Australian oil shales*", J. Therm. Anal., **49**, 737-743 (1997).

Berkovich, A., J., "*The thermal characterisation of Australian tertiary oil shales*", Ph.D. Dissertation, University of Technology, Sydney, New South Wales, Australia (1999).

Boateng, A., A., "*Rotary kiln transport phenomena*", Ph.D. Dissertation, University of British Columbia, British Columbia, Canada (1993).

Boateng, A., Barr, P., "*A thermal model for the rotary kiln including heat transfer within the bed*", Int. J. Heat Mass Transfer, **39**, 2131-2147 (1996).

Boateng, A., Barr, P., "*Modelling of particle mixing and segregation in the transverse plane of the rotary kiln*", Chem. Eng. Sci., **51**, 4167-4181 (1996).

Boateng, A., Barr, P., "*Granular flow behaviour in the transverse plane of a partially filled rotating cylinder*", J. Fluid Mech., **330**, 233-249 (1997).

Bram, L., "*Whatever happened to the Rundle Twins?*", Aust. Mining, **87**, 52-58 (1995).

Bridgewater, J., "*Fundamental powder mixing mechanisms*", Powder Technol., **15**, 215-236 (1976).

Cahn, D., S., Fuerstenau, D., W., "*Simulation of diffusional mixing of particulate solids by Monte Carlo techniques*", Powder Technol., **1**, 174-182 (1967).

Cantelaube, F., Bideau, D., Roux, S., "*Kinetics of segregation of granular media in a two-dimensional rotating drum*", Powder Technol., **93**, 1-11 (1997).

Charlip, David, "*The BMP file format, Part 1*", Dr. Dobb's J., **20**, 44-49 (1995a).

Charlip, David, "*The BMP file format, Part 2*", Dr. Dobb's J., **20**, 34-42 (1995b).

Clément, E., Rajchenbach, J., Duran, J., "*Mixing of a granular material in a bidimensional rotating drum*", Europhys. Lett., **30**, 7-12 (1995).

Dixon, A., Cresswell, D., "*Theoretical prediction of effective heat transfer parameters in packed beds*", AIChE J., **25**, 663-676 (1979).

Donald, M., B., Roseman, B., "*Mechanisms in a horizontal drum mixer*", Br. Chem. Eng., **7**, 749-753 (1962).

Ferron, J., Singh, D., "*Rotary kiln transport processes*", AIChE J., **37**, 747-758 (1991).

Gurgel, J., M., Kluppel, R., "*Thermal conductivity of hydrated silica-gel*", The Chem. Eng. J., **61**, 133-138 (1996).

Henein, H., Brimacombe, J., K., Watkinson, A., P., "*The modelling of transverse solids motion in rotary kilns*", Metall. Trans. B, **14B**, 207-220 (1983a).

Henein, H., Brimacombe, J., K., Watkinson, A., P., "*Experimental study of transverse bed motion in rotary kilns*", Metall. Trans. B, **14B**, 191-205 (1983b).

Henein, H., Brimacombe, J., K., Watkinson, A., P., "*An experimental study of segregation in rotary kilns*", Metall. Trans. B, **16B**, 763-774 (1985).

Hogg, R., Cahn, D., S., Healy, T., W., Fuerstenau, D., W., "*Diffusional mixing in an ideal system*", Chem. Eng. Sci., **21**, 1025-1038 (1966).

Hogg, R., Fuerstenau, D., W., "*Transverse mixing in rotating cylinders*", Powder Technol., **6**, 139-148 (1972).

Hogg, R., Shoji, K., Austin, L., "*Axial transport of dry powders in horizontal rotating cylinders*", Powder Technol., **9**, 99-106 (1974).

Hunt, M., L., "*Discrete element simulations for granular material flows: effective thermal conductivity and self-diffusivity*", Int. J. Heat Mass Transfer, **40**, 3059-3068 (1997).

Kelbert, F., Royere, C., "*Lateral mixing and heat transfer in a rolling bed*", Int. Chem. Eng., **31**, 441-449 (1991).

Kohring, G., A., "*Studies of diffusional mixing in rotating drums via computer simulations*", J. Phys, **5**, 1551-1561 (1995).

Kramers, H., Croockewit, P., "*The passage of granular solids through inclined rotary kilns*", Chem. Eng. Sci., **1**, 259-265 (1952).

Kunii, D., Smith, J., M., "*Heat transfer characterictics of porous rocks*", AIChE J., **6**, 71-77 (1960).

Lebas, E., Hanrot, F., Ablitzer, D., Houzelot, J., L., "*Experimental study of residence time, particle movement and bed depth profile in rotary kilns*", Can. J. Chem. Eng., **73**, 173-180 (1995).

Leger, C., B., Cook, C., A., Cundy, V., A., Sterling, A., M., Deng, X., Lighty, J., S., "*Bed mixing and heat transfer in a batch loaded rotary kiln*", Environ. Prog., **12**, 101-109 (1993).

Lehmberg, J., Hehl, M., Schugerl, K., "*Transverse mixing and heat tarnsfer in horizontal rotary drum reactors*", Powder Technol., **18**, 149-163 (1977).

Levine, John, "*Programming for graphics files in C and C++*", John Wiley & Sons, Brisbane, Australia (1994).

Luse, Marv, "*The BMP file format*", Dr. Dobb's J., **19**, 18-22 & 82-85 (1994).

Molerus, O., "*Heat transfer in moving beds with a stagnant interstitial gas*", Int. J. Heat Mass Transfer, **40**, 4151-4159 (1997).

Mu, J., Perlmutter, D., D., "*The mixing of granular solids in a rotary cylinder*", AIChE J., **26**, 928-934 (1980).

Nakagawa, M., Caprihin, A., Fukushima, E., "*MRI of granular flows in a rotating cylinder*" in Cavitation and Multiphase Flow Forum, **135**, 23-27, ASME, Los Angeles, CA, USA (1992).

Nityanand, N., Manley, B., Henein, H., "*An analysis of radial segregation for different sized spherical solids in rotary cylinders*", Metall. Trans. B, **17B**, 247-257 (1986).

Papadakis, S., E., Langrish, T., A., Kemp, I., C., Bahu, R., E., "*Scale-up of cascading rotary dryers*", Drying Technol., **12**, 259-277 (1994).

Perron, J., Bui, R., "*Rotary cylinders: solid transport prediction by dimensional and rheological analysis*", Can. J. Chem. Eng., **68**, 61-68 (1990).

Pershin, V., F., "*Modelling of loose material mixing process in the cross section of a rotary drum*", Theor. Found. Chem. Eng., **20**, 324-328 (1987).

Pershin, V., F., Mineav, G., A., "*Energetic approach in determination of motion of a granular material in a rotating drum*", Theor. Found. Chem. Eng., **23**, 432-435 (1989a).

Pershin, V., F., Mineav, G., A., "*Modelling the mixing of a granular material in a cross section of a smooth rotating drum*", Theor. Found. Chem. Eng., **23**, 249-255 (1989b).

Pickering, R., W., Feakes, F., Fitzgerald, M., "*Time for passage of material through rotary kilns*", J. Appl. Chem., **1**, 13-19 (1951).

Pollard, B., L., Henein, H., "*Kinetics of radial segregation of different sized irregular particles in rotary cylinders*", Can. Metall. Quart., **28**, 29-40 (1989).

Raghavan, G., S., V. Harper, J., M., Haberstroh, R., D., "*Heat transfer using granular media*", Trans. ASAE, 589-592 (1974).

Rao, S., M., Toor, H., L., "*Heat transfer between particles in packed beds*", Ind. Eng. Chem. Fundam., **23**, 294-298 (1984).

Rao, S., M., Toor, H., L., "*Heat transfer from a particle to a surrounding bed of particles. Effect of size and conductivity ratios*", Ind. Eng. Chem. Res., **26**, 469-474 (1987).

Ray, A., K., Prasad, K., K., Ray, H., S., Sen, P., K., "*Residence time in a rotary kiln for sponge iron making- prediction from kinetic data*", Steel India, **17**, 16-20 (1994).

Ristow, G., H., "*Particle mass segregation in a two-dimensional rotating drum*", Europhys. Letters, **28**, 97-101 (1994).

Rose, H., E., "*A suggested equation relating to the mixing of powders and its application to the study of the performance of certain types of machine*", Trans. Inst. Chem. Eng., **37**, 47-64 (1959).

Roseman, B., Donald, M., B., "*Effects of varying the operating conditions of a horizontal drum mixer*", Br. Chem. Eng., **7**, 823-827 (1962).

Rutgers, R., "*Longitudinal mixing of granular material flowing through a rotating cylinder. Part I Descriptive and theory*", Chem. Eng. Sci., **20**, 1079-1087 (1965a).

Rutgers, R., "*Longitudinal mixing of granular material flowing through a rotating cylinder. Part II Experimental*", Chem. Eng. Sci., **20**, 1089-1100 (1965b).

Saatdjian, E., Large, J., F., "*Heat transfer in a countercurrent gas-solid, packed column*", J. Heat Transfer., **110**, 385-389 (1988).

Saeman, W., C., "*Passage of solids through rotary kilns*", Chem. Eng. Prog., **47**, 508-514 (1951).

Sai, P., S., T., Surender, G., D., Damodaran, A., D., Suresh, V., Philip, Z., G., Sankaran, K., "*Residence time distribution and material flow studies in a rotary kiln*", Metall. Trans. B, **21B**, 1005-1011 (1990).

Schotte, W., "*Thermal conductivity of packed beds*", AIChE J., **6**, 63-67 (1960).

Sherritt, R., G., Caple, R., Behie, L., Mehrotra, A., "*The movement of solids through flighted rotating drums. Part 1: Model Formulation*", Can. J. Chem. Eng., **71**, 337-346 (1993).

Sherritt, R., G., Caple, R., Behie, L., Mehrotra, A., "T*he movement of solids interaction through flighted rotating drums. Part 2: Solids-Gas Inetraction and Model Validation*", Can. J. Chem. Eng., **72**, 240-248 (1994).

Sotocinal, S., A., Alikhani, Z., Raghavan, G., S., V., "*Heating/ drying using particulate medium: a review. Part 1. General and heat transfer parameters*", Drying Technol., **15**, 441-459 (1997a).

Sotocinal, S., A., Alikhani, Z., Raghavan, G., S., V., "*Heating/ drying using particulate medium: a review. Part 2. Equipment*", Drying Technol., **15**, 461-475 (1997b).

Southern Pacific Petroleum Financial report, Southern Pacific Petroleum N.L., 1991.

Sullivan, W., N., Sabersky, R., H., "*Heat transfer to flowing granular media*", Int. J. Heat Mass Transfer, **18**, 97-107 (1975).

Sze, M., W., Ang, H., M., Tade, M., O., "*Particle dynamics in a cold model rotary kiln*" in Proc of the 23rd Aust. Chem. Eng. Conf., **4**, 27-32, IEAust, Adelaide, SA, Australia (1995).

Taciuk, W., Turner, R., "*Development status of Australian oil shale processing utilizing the Taciuk processor*", Fuel, **67**, 1405-1407 (1988).

Tackie, E., Watkinson, A., Brimacombe, J., "*Experimental study of the elutriation of particles from rotary kilns*", Can. J. Chem. Eng., **67**, 806-817 (1989).

Tackie, E., Watkinson, A., Brimacombe, J., "*Mathematical modelling of the elutriation of fine materials from rotary kilns*", Can. J. Chem. Eng., **68**, 51-60 (1990).

Thomas, L., C., "*Heat Transfer*", Prentice Hall, New Jersey (1992).

Wes, G., W. ,J., Drinkenburg, A., A., H., Stemerding, S., "*Solids mixing and residence time distribution in a horizontal rotary drum reactor*", Powder Technol., **13**, 177-184 (1976a).

Wes, G., W. ,J., Drinkenburg, A., A., H., Stemerding, S., "*Heat transfer in a horizontal rotary drum reactor*", Powder Technol., **13**, 185-192 (1976b).

Williams, J., Khan, M., "*The mixing and segregation of particulate solids of different particle size*", Chem. Eng., **269**, 19-25 (1973).

Woodle, G., Munro, J., "*Particle mixing and mixing in a rotary kiln*", Powder Technol., **76**, 241-245 (1993).

Yagi, S., Kunii, D., "*Studies on effective thermal conductivities in packed beds*", AIChE J., **3**, 373-381 (1957).

Yang, L., Farouk, B., "*Modelling of solid particle flow and heat transfer in rotary kiln calciners*", J. Air Waste Manage. Assoc., **47**, 1189 – 1196 (1997).

Zik, O., Stavans, J., "*Self-diffusion in granular flows*", Europhys. Letters, **16**, 255-258 (1991).

Zingarelli, J., Muradian, A., Stephenson, L., "*Upgrading of Stuart oil shale*", Fuel, **67**, 1408-1410 (1988).

APPENDICES

Appendix 1: The bitmap file format.

The Bitmap file format is a type of a computer graphics file. Bitmaps are the most commonly used graphics files since they represent a picture as a rectangular array of dots (Levine, 1994). Luse (1994) and Charlap (1995a, b) studied the bitmap file format and published papers on the structure of a bitmap file.

To the untrained eye, a Bitmap file just consists of a series of hexadecimal values. However, there is a structure to the Bitmap file format. In short a bitmap file consists of a File Header, a Bitmap Header, an optional Colour Palette and a Bitmap. Figure A1.1 shows a typical bitmap file viewed as text. Figure A1.2 shows the image represented by the bitmap file of Figure A1.1. The values of Figure A1.1 have been allocated different type faces to represent the different sections of the bitmap file. These will be discussed in more detail in this appendix.

Each entry, consisting of two values from 0 to F, of Figure A1.1 represent 8 bits or 1 byte of information. A *WORD* consists of 32 bits or 4 bytes of information.

A1.1 STRUCTURE OF THE BITMAP FILE

Bitmaps can exist with different numbers of colours, from a monochrome bitmap, where each pixel is represented by 1 bit, to a full colour bitmap, where each pixel is represented by 32 bits. In the current research, 256 colour bitmap files were used and the structure of this type of bitmap is the focus of this appendix.

42 4D AE 04 00 00 00 00 00 36 04 00 ~~00 28 00~~
~~00 00 0A 00 00 00 0A 00 00 00 01 00 08 00 00 00~~
~~00 00 78 00 00 00 00 00 00 00 00 00 00 00 00 00~~
~~00 00 00 00 00 00~~ *00 00 00 00 40 00 00 00 80 00*
00 00 FF 00 00 00 00 20 00 00 40 20 00 00 80 20
00 00 FF 20 00 00 00 40 00 00 40 40 00 00 80 40
00 00 FF 40 00 00 00 60 00 00 40 60 00 00 80 60
…… *……*
FF 00 FF 80 FF 00 00 A0 FF 00 40 A0 FF 00 80 A0
FF 00 FF A0 FF 00 00 C0 FF 00 40 C0 FF 00 80 C0
FF 00 FF C0 FF 00 00 FF FF 00 40 FF FF 00 80 FF
FF 00 FF FF FF 00 00 FF FF FF FF FF FF FF FF E0
00 00 FF 00 FF FF FF FF FF FF 00 FF 00 00 FF FF
….. ….
FF E0 FF FF 00 00 FF E0 FF FF FF FF FF FF E0 FF
00 00 00 FF FF FF FF FF FF FF FF E0 00 00

Figure A1.1: Text display of a 256 colour bitmap file.

A1.1.1 File Header

The File Header is shown as the **BOLD** font in Figure A1.1. The first two bytes of any image file indicates the image format. In the case of a bitmap file, the first two entries are 42 and 4D, respectively. This represents the characters B and M, short for BitMap. This is followed by a *WORD* to represent the size of the image, which by default should represent the size in bytes but was often set to zero or could contain the size of the file in words instead of bytes (Luse, 1994). The co-ordinates of the image hotspot is located in the next *WORD*. The hotspot is only used when the image in the file is used as a cursor. The final *WORD* of the File Header represents the offset from the beginning of the file to the beginning of the bitmap. This is important if different image formats are used since the size of the colour palette

depends on the number of colours in the palette. The File Header consists of 14 bytes of data.

A1.1.2 Bitmap Header

The Bitmap Header is shown as the ~~STRIKETHROUGH~~ font in Figure A1.1. The first *WORD* in the Bitmap Header is the size in bytes of the Bitmap Header. This value is also used to indicate what version of a bitmap file is being worked with. The second and third *WORD*s in the Bitmap Header contain the width and height of the image in pixels, respectively. The Bitmap Header also contains data to determine the number of bit planes used, the number of bits used per pixel, whether compression has been used and if so what type of compression and finally the size of the Bitmap in bytes. The Bitmap Header is 40 bytes in length.

A1.1.3 Colour Palette

The colour palette is shown as the *ITALIC* font in Figure A1.1. For a 256 colour bitmap, the Colour Palette consists of 256 combination of the Red, Green and Blue values to represent the colours in the image. Each colour is buffered to a *WORD* so the total size of the Colour Palette is 1024 bytes.

A custom colour palette was created for the analysis of the images obtained from the experiments. This palette consisted of a 100 colour specifications representing the black material, 100 colour specifications representing the orange material and 50 colour specifications representing the background colour (white) of the drum. Six other colours were required to complete the 256 colour palette. These 6 colours were different shades of red, green and blue and were used to represent important points in the images such as the apex positions, as shown in Figures 5.1 and 5.2.

The colour palette used in Figure A1.1 is the Windows default colour palette. The first colour specification equals 00 00 00 00. This represents values of 0 for the blue, green and red, respectively. The last 00 is used to buffer the colour to a *WORD*. This colour specification is referred to as colour 00 in the Bitmap.

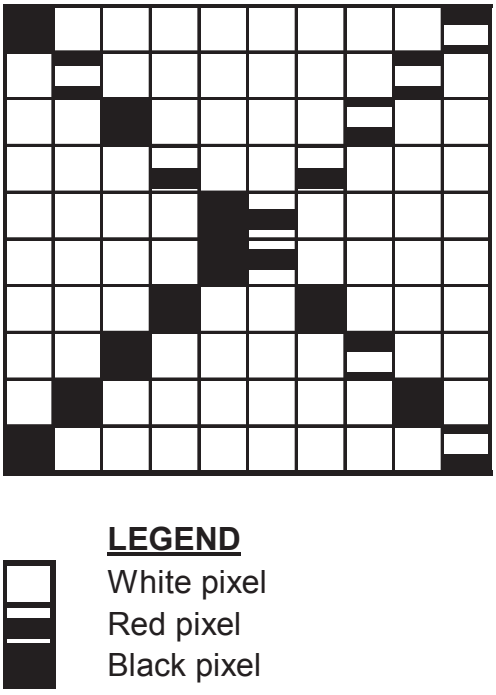

Figure A1.2: Image represented by data of Figure A1.1.

A1.1.4 Bitmap

The data representing the pixels is represented by the UNDERLINED values in Figure A1.1. This data follows immediately after the Colour Palette. The image is stored as a series of pixels from the bottom up. Each pixel in the line is represented by the index of the colour from the Colour Palette. Each line of data is buffered to the next full *WORD*. For example, if the current image has a width of 10 pixels, each pixel is represented by a value from 0 to 255 to represent the pixels colour from the Colour Palette. However, a WORD contains 4 bytes so 3 *WORD*s are required to represent the line in the image. The values of these last two bytes of the last *WORD* are set equal to 00.

A1.2 READING THE BITMAP FILE

In order to read the data in a bitmap, the format of the file as described above must be known. Since a bitmap file consists of hexadecimal values, some of which are unprintable, it is necessary to open the file as a binary file if it is desired to analyse them. This allowed all the data in the file to be analysed. Since all the experimental images were similar in format only the width and height of the images needed to be read from the file. These fields consisted of a *WORD*. Figure A1.2 represents a bitmap image of 10 pixels wide and 10 pixels high. This is expressed in the Bitmap Header by the values 0A 00 00 00. This hexadecimal value equals 10 in decimal. The images used in the experiments were all calibrated to the custom Colour Palette described above. The Colour Palette from the images was thus known and did not need to be read. The bytes of the Bitmap were read, the value indicating what colour the pixel represented from the colour table.

For example looking at the first entry of the Bitmap of Figure A1.1: this byte has the value of 00, which has a decimal value of 0. Thus the first pixel represents the zeroth colour in the colour table which was black. Thus the first pixel (from the bottom up) of the image is a black pixel. This is shown in Figure A1.2. Continuing along, there are 8 values of FF, representing the white colour followed by 1 value of E0, which represents the 225th colour in the Colour Palette and is the red colour. Figure A1.2 was drawn using the default Windows colour palette. In the experimental images the 1st to the 100th entries in the Colour Palette represented the black material, the second hundred represented the orange material and the next 50 colour specifications represented the white colour of the drum. This was followed by 2 green, 2 blue and 2 red colour specifications.

The psuedocodes for the programs that converts bitmap files into data that can be analysed are given in Appendix 2.

Appendix 2: Psuedo codes for the software written as part of the thesis.

A2.1 CONVERTING THE BITMAP IMAGES TO AN ARRAY

1. Obtain file name from user input.
2. Open the file in binary mode to allow non printable characters to be read as hexadecimal values.
3. Read bytes 19 to 22 to determine the width, W, of the image.
4. Read the next *WORD* (bytes 23 to 26) to obtain the height, H, of the image.
5. Skip the next 28 bytes. The 29th byte is the start of the Colour Palette.
   - 5.1. If details of the colour specifications are required, create an array so that the data can be read.
   - 5.2. If details of the colour specification are not required (as is the case in the current image analysis work – since the colour specifications are known), skip the 1024 bytes of the Colour Palette.
6. Create a dynamic array, Ä, of W+ 2 columns and H+ 2 rows.
7. Allocate the values in the 1st column, the (W+ 2)nd, the first row and the (H+ 2)nd row of Ä to the buffer value, which in this case was taken as 9.
8. Read the data from the Bitmap part of the image into the array:
   - 8.1. Loop through the rows, index ***r*** starting at 2 since first row is the buffer,
     - 8.1.1. Loop through the columns, index ***c*** starting at 2,
       - 8.1.1.1. Read the next byte (pixel), P, from the Bitmap.
       - 8.1.1.2. If the value of P is between 0 & 99, Ä[***r***, ***c***]= 0 (black).
       - 8.1.1.3. If the value of P is between 100 & 199, Ä[***r***, ***c***]= 1 (orange).
       - 8.1.1.4. If the value of P is between 200 & 249, Ä[***r***, ***c***]= 2 (white).
       - 8.1.1.5. If the value of P is either 250 or 251, Ä[***r***, ***c***]= 4 (green).
       - 8.1.1.6. If the value of P is either 252 or 253, Ä[***r***, ***c***]= 5 (blue).
       - 8.1.1.7. If the value of P is either 254 or 255, Ä[***r***, ***c***]= 6 (red).
       - 8.1.1.8. Increase ***c*** by one.

     if ***c*** *<= W+1*

     8.1.2. Increase ***r*** by one.

     if ***r*** *<= H+1*
9. Close the bitmap file.
10. Analyse Array using either the mixing or segregation routing.
11. If not destroyed, destroy dynamic array, Ä.

A2.2 PSUEDO CODE FOR THE MIXING ANALYSIS

1. Obtain experimental series name and numbers from user input.
2. Create the results file.
3. Loop through image series starting at the first image.

if image number <= total number of images

3.1. Set mixing contact equal to zero.

3.2. Read Bitmap into dynamically allocated array, as described above.

3.3. Loop through the rows, ***r***, of the array starting at 2.

if ***r*** *<= H+1*

3.3.1. Loop through the columns, ***c***, of the array starting at 2 & read pixel value, P.

if ***c*** *<= W+1*

3.3.1.1. If P equals 1, check surrounding pixels.

3.3.1.1.1. Check P[***r*** ± 1, ***c***] and P[***r***, ***c*** ± 1].

3.3.1.1.1.1. If surrounding pixel is of type 0 increase contact by 1.

3.3.1.2. Increase ***c*** by 1.

3.3.2. Increase ***r*** by 1.

3.4. Write total contact, in pixels length, between Orange and Black of current image to file.

3.5. Delete dynamically allocated array.

3.6. Increase image number.

4. Save results file.

A2.3 PSUEDO CODE FOR THE SEGREGATION ANALYSIS

1. Obtain experimental series name and numbers from user input.
2. Create the bed outline file.
3. Read bitmap of the outline described in Chapter 7 into a dynamically allocated array.

3.1. Loop through the outline image and find the location of the green pixels. This shows the position of Apex A and Apex B.

3.2. Calculate the position of the rotational centre of the bed from Apex A and Apex B as described in Chapter 5.

3.3. Loop through the pixels of the outline image,

3.3.1. If the current pixel, P, is white,

if $r <= H+1$

3.3.1.1. Check surrounding pixels for black pixels, if a black pixel is found calculate the distance and angle from the centre of rotation to P.

3.3.1.2. Save the distance and angle.

3.4. Sort and reduce array from approximately 9000 points to 360 points, one for each degree of the circumference at the centre of rotation.

3.5. Close bitmap.

3.6. Save the data in the bed outline file.

4. Create a segregation results file.

5. Loop through segregation images.

if image number <= total number of images

5.1. Read segregation image into a dynamically allocated array.

5.1.1. Loop through the segregation image and find the location of the green pixels. This shows the position of Apex A and Apex B.

5.1.2. Calculate the position of the rotational centre of the bed from Apex A and Apex B as described in Chapter 5.

until end of image

5.1.3. Loop through the pixels of the segregation image,

5.1.3.1. If the current pixel, P, is orange or black,

5.1.3.1.1. Determine the distance, $D_{P\text{-}O}$ from P to the centre of rotation.

5.1.3.1.2. Determine the angle, β, from centre of rotation to P.

5.1.3.1.3. Calculate the outline array distance, $D_{O,\beta}$ at the calculate angle.

5.1.3.1.4. Compare the distance of the outline at the calculated angle to the distance of the pixel to the centre of rotation.

5.1.3.1.4.1. If $D_{P\text{-}O} <= D_{O,\beta}$, P is within the outline.

5.1.3.1.4.2. Increment the colour count in the respective layer.

5.1.3.1.5. Read next pixel of array.

5.1.4. Delete dynamically allocated array.

5.1.5. Write the colour counts in each layer to the results file.

5.1.6. Increase image number by 1.

6. Save and close results file.

Appendix 3: Industrial rotating kiln simulation program.

Ideally a copy of the simulation developed during the course of the PhD would be included with the thesis. However due to licensing restrictions of educational software a standalone version of the program could not be created. In this section of the thesis, the graphical interface of the simulation is described.

A3.1 SIMULATION STRUCTURE

The simulation consisted of various forms. The main forms were the Start Form, shown in Figure A3.1, the Data Specification Form shown in Figure A3.2 and the Results Form shown in Figure A3.3.

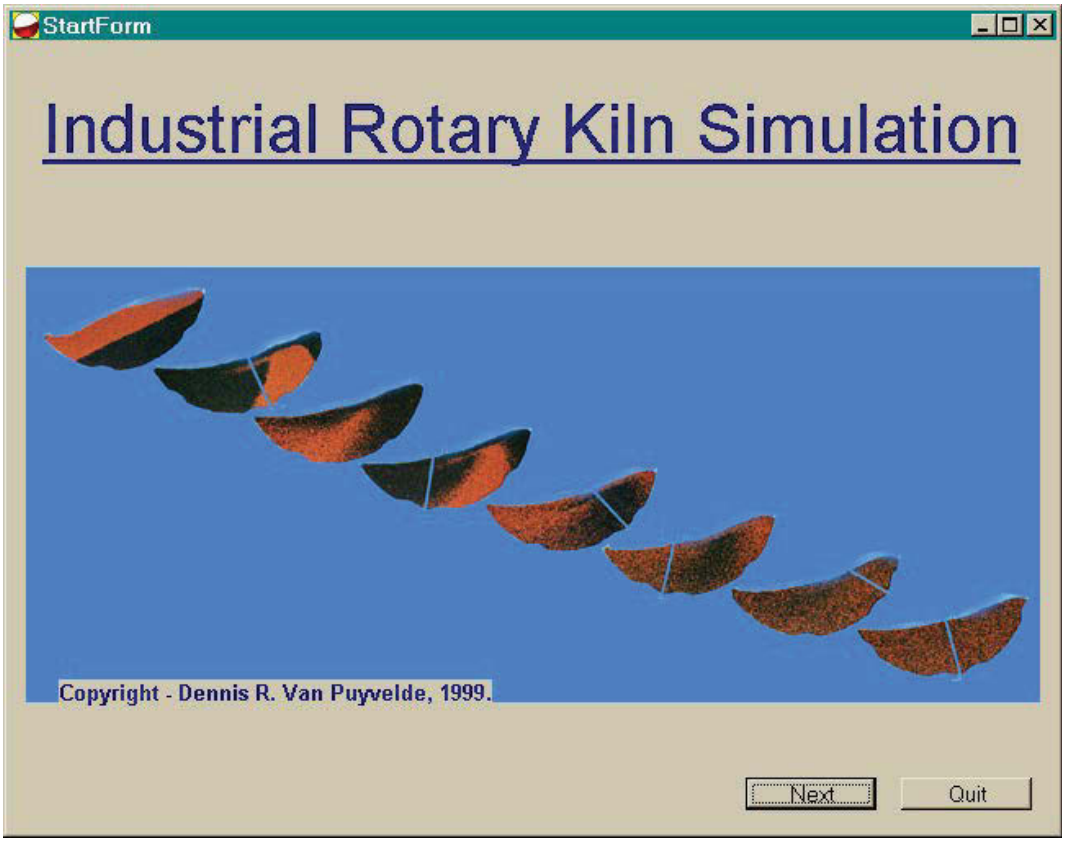

Figure A3.1: Start Form of the simulation.

A3.2 START FORM

The sole purpose of the Start Form was to start the program. The picture in the centre of the Start Form shows different mixing stages of the rolling bed. The Quit button was used to exit the program and the Next button was used to proceed to the next stage of the simulation, which was the Data Specification Form.

A3.3 DATA SPECIFICATION FORM

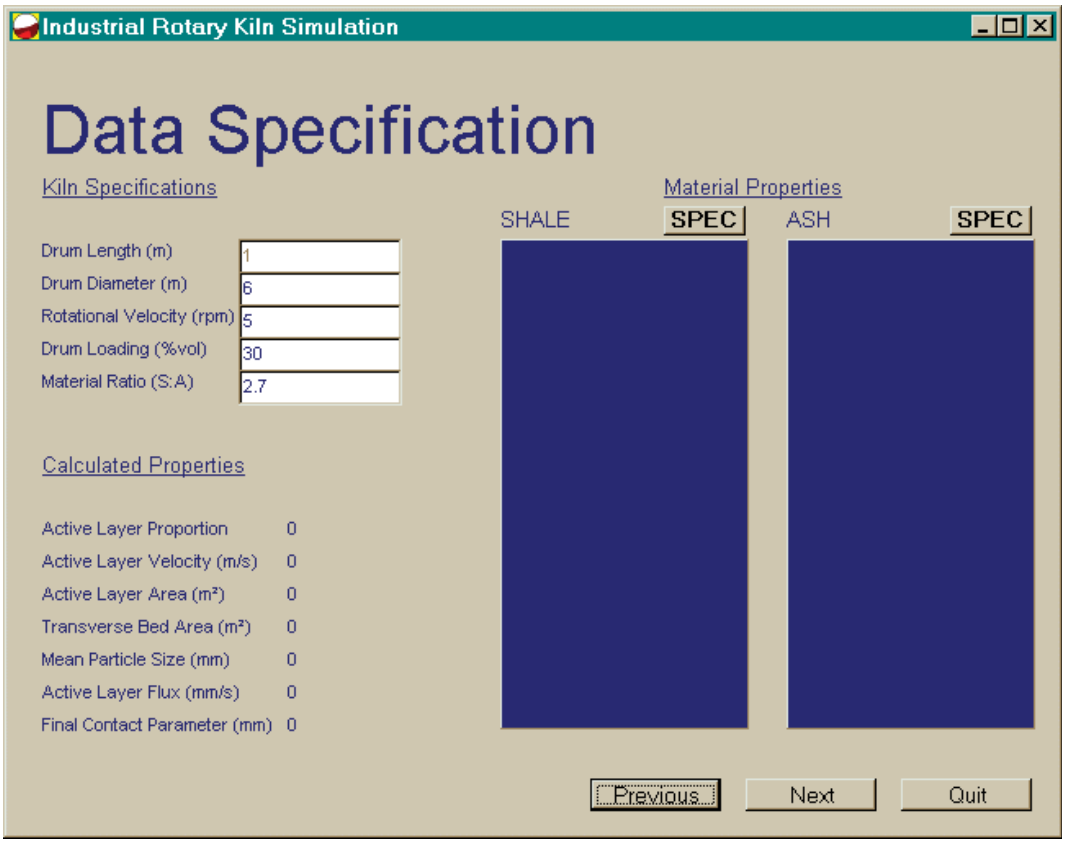

Figure A3.2: Data Specification Form.

The Data Specification Form was used to specify the rotating kiln operational parameters and the materials used in the simulation. This form consisted of two sections. The first section, shown by the white Edit boxes on the top left hand side,

was used to specify the characteristics of the kiln. Parameters such as the drum diameter, rotational velocity, drum loading and material ratio were specified. The length of the drum was fixed at 1 m. The two dark regions on the right hand side were used to specify the properties of the ash and the shale materials. These specifications included the initial temperature and the particle size distribution and were accessed using the SPEC button. The total flow of each material was calculated from the drum specifications. After the kiln and the material were specified, the calculated properties shown on the bottom left hand side of the Data Specification form were updated. Full material and drum specifications were required before the program would proceed to the next form of the simulation, which is the Results Form, using the Next button.

A3.3.1 Specify Feed Form

The Specify Feed Form was used to specify the size distribution and the materials of the Ash and Shale material used in the simulation. The Specify Feed Form is shown in Figure A3.3.

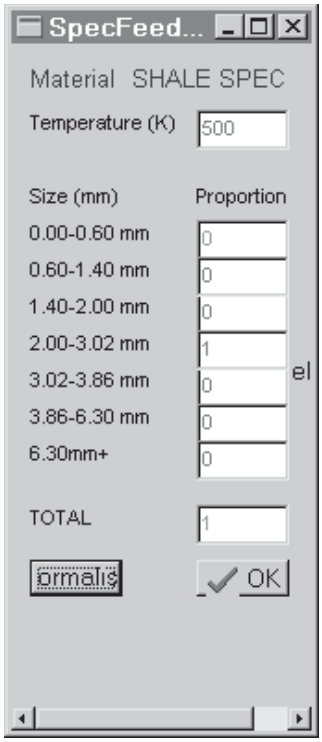

Figure A3.3: Specify Feed Form.

Initially the temperatures for all the material size ranges for either the Shale or the Ash were the same.

A3.4 RESULTS FORM

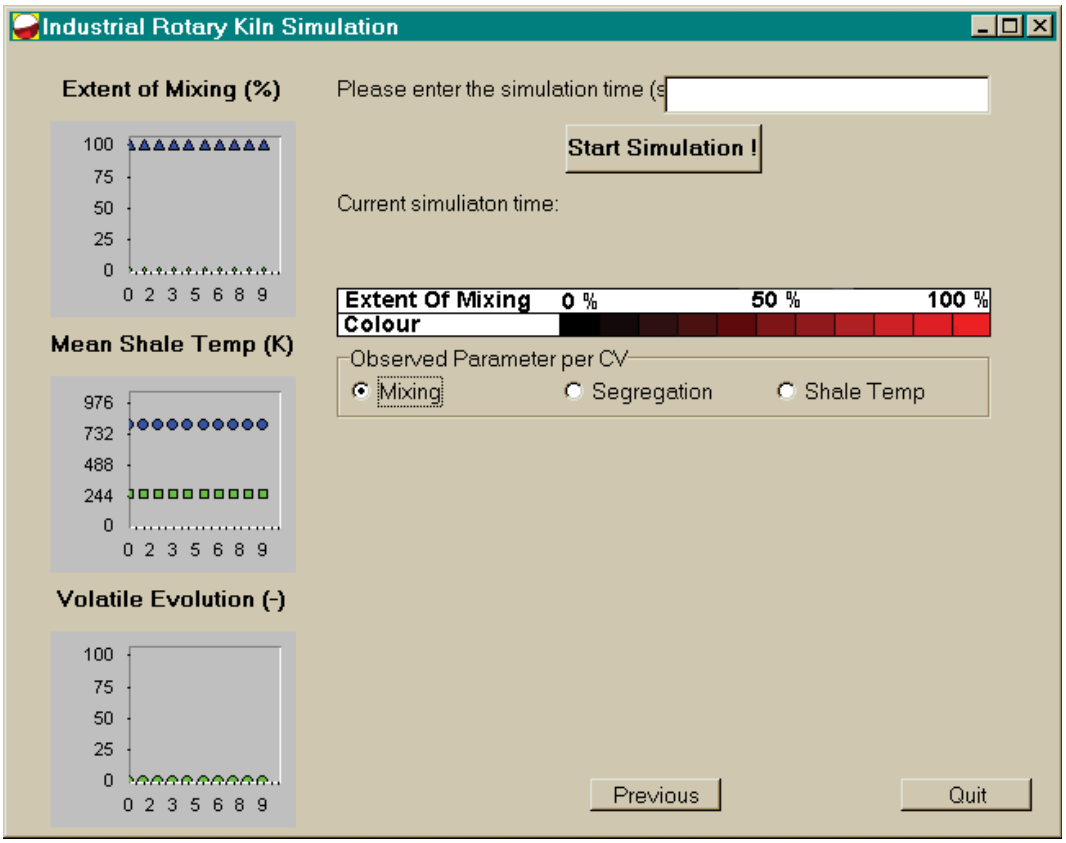

Figure A3.4: Results Form.

The Results Form shown in Figure A3.4 appears after pressing the Next button after complete data specification in the Data Specification Form.

The Results Form has a few regions. Firstly the three graphs on the left hand side allow the progress of the simulation to be tracked. These graphs have two series, the darker series represents a maximum and the lighter coloured series represents the time dependent value. These graphs illustrate the dynamic behaviour of the system

and included the Extent Of Mixing as a percentage of the maximum mixing in the kiln, the mean shale temperature in the kiln and the amount of volatile evolution as a percentage of the shale feed to the kiln. The total duration of the simulation time could be specified in the Edit box in the top right hand corner. The change in the control volumes of the grid as specified in Figure 8.2 could be tracked.

Three parameters could be tracked in the different control volumes. These were the extent of mixing or the mean particle size or the mean temperature in each control volume. The results of these in the grid were represented by different shades of blue, green or red respectively.

Images of the Results Form of the simulation are provided in the next section for different stages of the scenario of Case 2 as presented in Table 9.2.

A3.4.1 Segregation

The initial transverse size distribution for Case 2 is shown in Figure A3.5 and was represented by different shades of green with the black colour representing a particle size of 0 mm and a bright green colour representing a particle size of 6.30 mm as shown in the legend of Figure A3.5.

The shale and the ash particle sizes for Case 2 were different and this is reflected by the different shaded zones in Figure A3.5. For the initial configuration, the shale was added to the stagnant layer of the kiln.

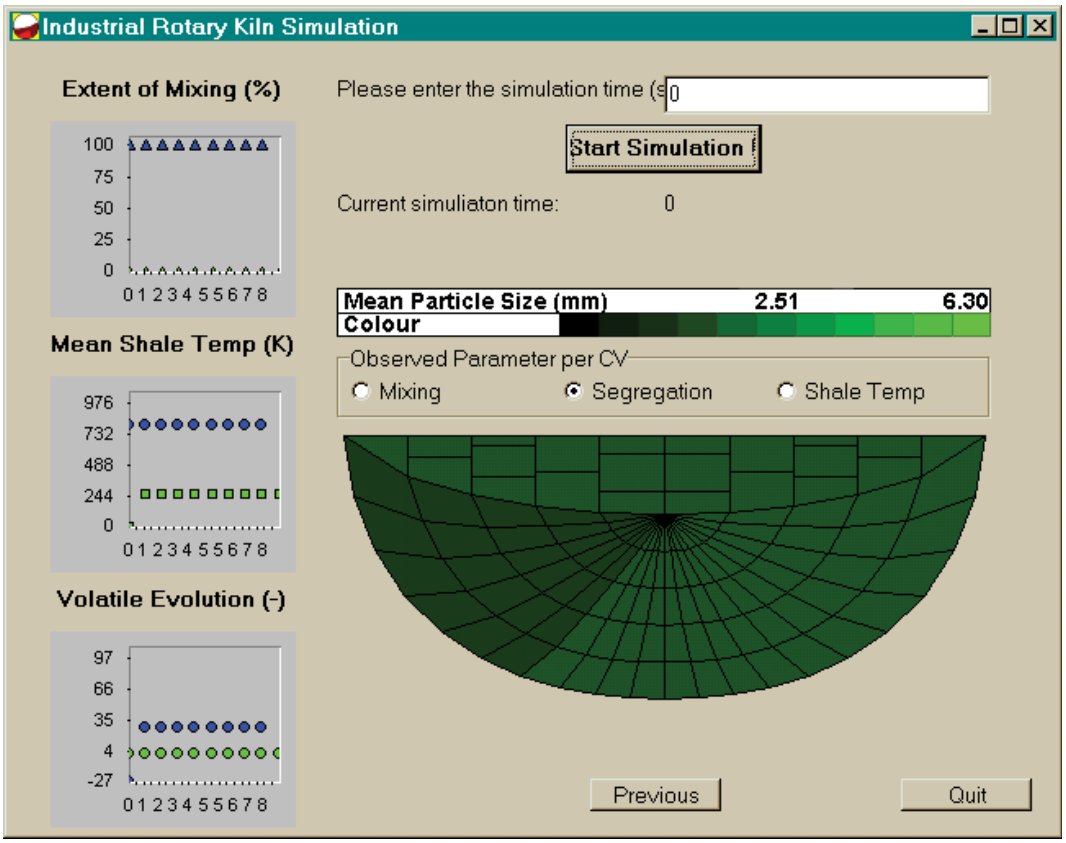

Figure A3.5: Initial segregation results form (Case 2)

The simulation was run for 60 seconds and at that time the bed was fully segregated. This is shown in Figure A3.6. As can be seen from the grid system, the mean particle size in the control volumes closer to the centre of rotation was less than the particle size of the other control volumes indicated by the darker coloured polygons on the grid. This showed that the finer material segregated.

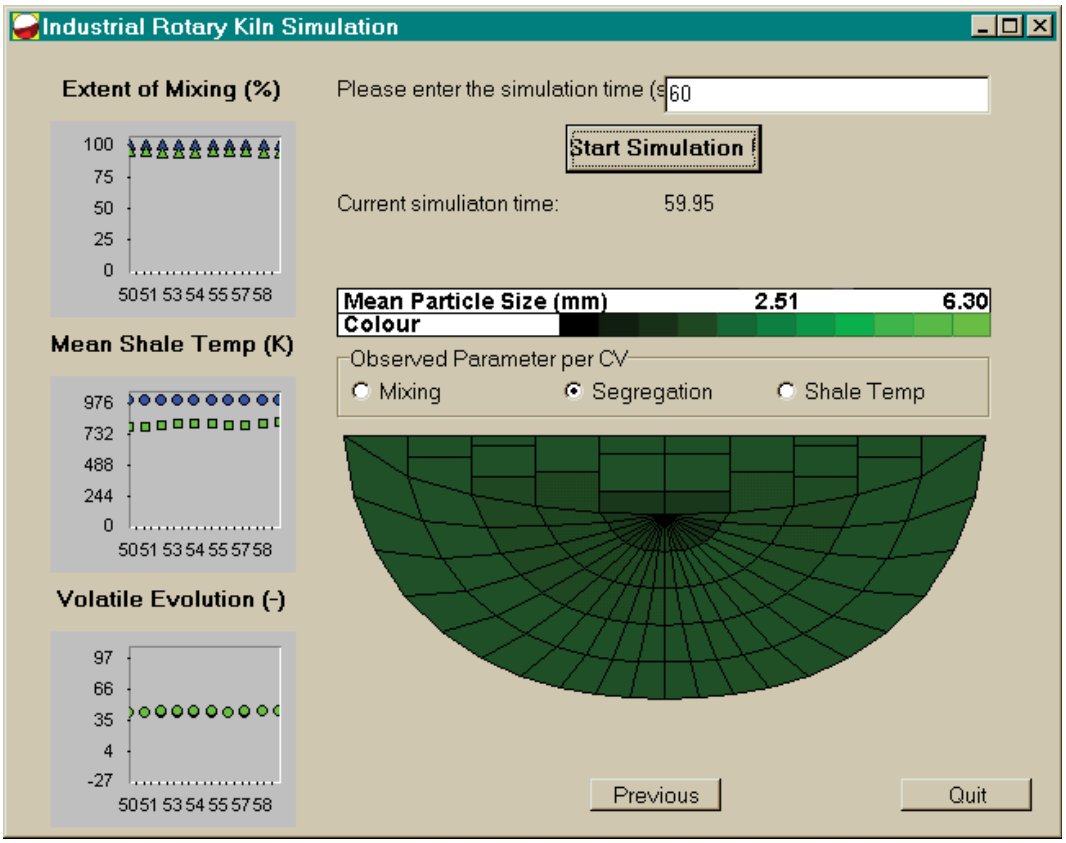

Figure A3.6: Segregated results form after 60 seconds (Case 2)

It should also be noted that the extent of mixing, the mean shale temp and the volatile evolution graphs all increased.

A3.4.2 Mixing

Different mixing levels are shown in Figure A3.7. Initially, the grid was coloured completely black, as the materials were completely unmixed. As time progressed, the mixing in the control volumes increased and this was shown by the lighter coloured control volumes in the grid. The mixing was completed after 60 seconds. The darker region in the centre of the bed was due to the segregated material.

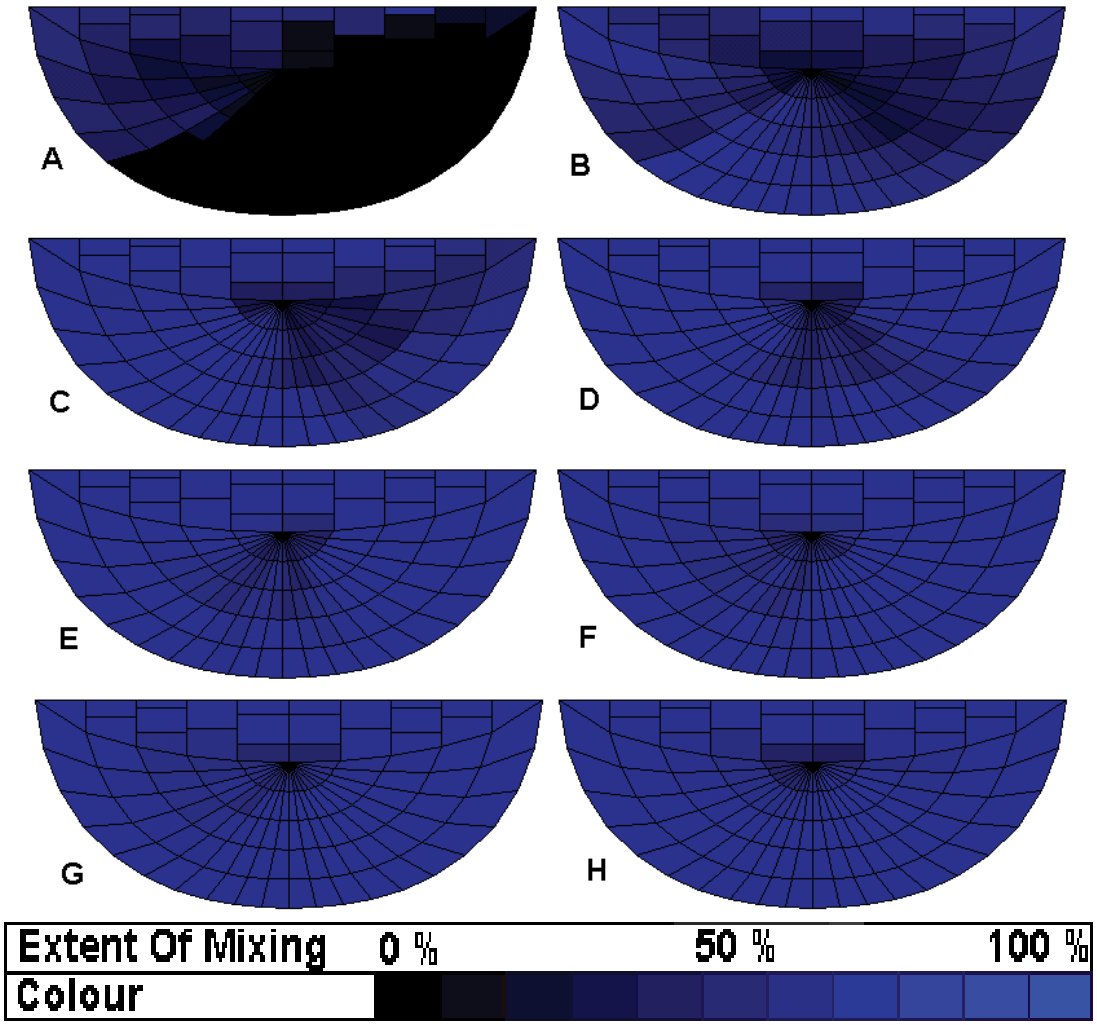

A) 5 sec, B) 10 sec, C) 15 sec, D) 20 sec, E) 25 sec, F) 30 sec, G) 40 sec and H) 60 sec

Figure A3.7: Mixing results.

Appendix 4: Papers submitted or published.

A4.1 UNREFEREED CONFERENCE PUBLICATIONS

D. Van Puyvelde, *"Simulation of oil evolution from oil shale in a rotary kiln"* in 3rd Australian Student Particle Technology Conference, Uni. of Newcastle, Newcastle, New South Wales, Australia (1998).

A4.2 REFEREED CONFERENCE PUBLICATIONS

D.R. Van Puyvelde, B.R. Young, M.A. Wilson, *"Simulation of the mixing and segregation in an industrial rotating drum"* in Proc. of the 28th Aust. & New Zealand Chem. Eng. Conf., IEAust, Perth, Western Australia, Australia (2000).

D. R. Van Puyvelde, B. R. Young, M. A. Wilson, S., J., Schmidt, *"Determination of transverse segregation in a rolling drum using image processing*" in Proc. of the 27th Aust. & New Zealand Chem. Eng. Conf., IEAust, Newcastle, New South Wales, Australia (1999).

D. Van Puyvelde, B. Young, M. Wilson, J. Schmidt, *"Experimental determination of mixing kinetics in a rolling drum"*, Proc. of the 26th Aust. & New Zealand Chem. Eng. Conf., IEAust, Port Douglas, Queensland, Australia (1998).

D. Van Puyvelde, B. Young, M. Wilson, J. Schmidt, *"Dynamic modelling of transverse mixing in a rotary kiln"* in Proc. of the 25th Aust. & New Zealand Chem. Eng. Conf., IEAust, Rotorua, New Zealand (1997).

A4.3 INTERNATIONAL REFEREED JOURNAL PUBLICATIONS

D.R. Van Puyvelde, B.R. Young, M.A. Wilson, *"Simulating the mixing and segregation behaviour of solids in a rotating kiln"*, Comp. Chem. Eng., **Submitted**, (Apr 2000).

D.R. Van Puyvelde, B.R. Young, M.A. Wilson, *"Comparison of transverse mixing kinetic data obtained from a rolling drum"*, Powder Technol., **Submitted**, (2000).

D.R. Van Puyvelde, B. R. Young, M. A. Wilson, S. J. Schmidt, *"Modelling transverse segregation in a rolling drum"*, Trans. I. Chem. E. Res. Dev., **78A**, 643-650 (2000).

D.R. Van Puyvelde, B., R., Young, M., A., Wilson, S., J., Schmidt, *"Modelling transverse mixing in a rotating drum"*, Can. J. Chem. Eng., **78**, 1-8 (2000).

D. R. Van Puyvelde, B., R., Young, M., A., Wilson, S., J., Schmidt, *"Experimental determination of transverse mixing in a rotating drum"*, Powder Tech., **106**, 183-191 (1999).